Title
Low dimensional magnetism

Author
Kjall, Jonas Alexander

Publication Date
2012

Peer reviewed|Thesis/dissertation

Low dimensional magnetism

by

Jonas Alexander Kjäll

A dissertation submitted in partial satisfaction of the
requirements for the degree of
Doctor of Philosophy

in

Physics

in the

Graduate Division
of the
University of California, Berkeley

Committee in charge:
Professor Joel E. Moore, Chair
Professor Ashvin Vishwanath
Professor Rachel A. Segalman

Fall 2012

Low dimensional magnetism

Abstract

Low dimensional magnetism

by

Jonas Alexander Kjäll
Doctor of Philosophy in Physics

University of California, Berkeley

Professor Joel E. Moore, Chair

Magnetism is a subject that has fascinated mankind for countless generations. With the development of quantum mechanics around a century ago a fundamental understanding of many of the underlying causes of magnetism were obtained. However, the long range interaction combined with the complex systems magnetism appears in makes it very hard to investigate it. In our days this research area is more active than ever, mainly due to future demand of the electronic industry for components engineered down to the atomic level. Quantum effects gets more important at short scales, especially in lower dimensional materials like sheets and wires. The rapidly increasing amount of computational power available makes the numerical techniques a more important part of the research effort. Many of these are especially well suited to analyze lower dimensional quantum problems. Three of the most important techniques, (classical) Monte Carlo, Exact Diagonalization (ED) and matrix product states (MPS) based techniques, like density renormalization group (DMRG) and time evolving block decimation (TEBD) will be described in some detail and put to use later in this dissertation.

With the rapid development of experimental techniques for ultracold gases in optical traps a new approach to investigate magnetic properties that are hard achieve or control in the solid state has emerged. We first study the ground-state phase diagram of a spin-1 condensate trapped in an optical trap when the magnetic dipole interaction between the atoms is taken into account along with confinement and spin precession. The boundaries between the regions of ferromagnetic and polar phases move as the dipole strength is varied and the ferromagnetic phases can be modulated. The magnetization of the ferromagnetic phase perpendicular to the field becomes modulated as a helix winding around the magnetic field direction, with a wavelength inversely proportional to the dipole strength. This modulation should be observable for current experimental parameters in ^{87}Rb. Hence the much-sought supersolid state, with broken continuous translation invariance in one direction and broken global $U(1)$ invariance, occurs generically as a metastable state in this system as a result of dipole interaction. The ferromagnetic state parallel to the applied magnetic field becomes striped in a finite system at strong dipolar coupling.

The development of artificial gauge fields, that can mimic magnetic fields, in ultracold gases suggests that atomic realization of fractional quantum Hall physics will become experimentally practical in the near future. While it is known that bosons on lattices can support quantum Hall states, the universal edge excitations that provide the most likely experimental probe of the topological order have not been obtained. We find that the edge excitations of an interacting boson lattice model are surprisingly sensitive to interedge hybridization and edge-bulk mixing for some confining potentials. With properly chosen potentials and fluxes, the edge spectrum is surprisingly clear even for small systems with strong lattice effects such as bandwidth. Various fractional quantum Hall phases for bosons can be obtained, and the phases $\nu = 1/2$ and $\nu = 2/3$ have the edge spectra predicted by the chiral Luttinger liquid theory.

Also, some of the traditional experimental techniques for detecting magnetic order and dynamics in solid state materials, like neutron scattering has had somewhat of a renaissance lately. In a recent experiment on $CoNb_2O_6$, Coldea *et al.* [1] found for the first time experimental evidence of the exceptional Lie algebra E_8. The emergence of this symmetry was theoretically predicted long ago for the transverse quantum Ising chain in the presence of a weak longitudinal field. We consider an accurate microscopic model of $CoNb_2O_6$ incorporating additional couplings and calculate numerically the dynamical structure function using a recently developed matrix-product-state method. The excitation spectra show bound states characteristic of the weakly broken E_8 symmetry. We compare the observed bound state signatures in this model to those found in the transverse Ising chain in a longitudinal field and to experimental data.

Finally, we investigate the ground state phase diagram of a related quantum spin chain, the $S = 2$ XXZ chain with single-ion anisotropy. The interest in this system comes mainly from connecting the highly quantum mechanical spin-1 phase diagram with the classical S=∞ phase diagram. While most of these questions where believed to have been satisfactorily answered mainly with DMRG, some recent studies have questioned some of the conclusions. We use several of the recent advances within DMRG and perform a detailed analysis of the whole phase diagram. We extend the phase diagram by considering different types of single ion anisotropies which help us to answer two important questions: First we show that one can adiabatically move from the isotropic Heisenberg point to the so-called large-D phase with a continuous change of the Hamiltonian. Second, we can tune the model into a predicted intermediate phase which is equivalent to the topologically non-trivial spin-1 Haldane phase. Furthermore, we study the spin-3 XXZ chain to help explaining the development of the classical phase diagram.

To my parents,

Contents

List of Figures **v**

Acknowledgments **x**

List of Acronyms **xii**

I Introduction 1

1 Brief introduction to magnetism **2**
1.1 Classic magnetism . . . 3
1.2 Atomic Magnetism . . . 4
1.3 Magnetism in condensed matter . . . 6
1.4 Quantum phases and phase transitions . . . 8
1.5 Spin chains . . . 10
1.6 Bose-Hubbard model . . . 12
1.6.1 Hofstadter's Butterfly . . . 13
1.7 Quantum Hall . . . 13
1.8 Experimental techniques . . . 16
1.8.1 Ultracold gases . . . 16
1.8.2 Neutron scattering . . . 17

2 Overview of dissertation **19**

II Numerical Techniques 21

3 Simulating quantum systems **22**
3.1 Monte Carlo . . . 22
3.2 Exact Diagonalization . . . 23
3.3 Matrix Product State based methods . . . 26
3.3.1 Entanglement . . . 27
3.3.2 Time Evolving Block Decimation . . . 28

3.3.3 Matrix product states 29

III Magnetism in Ultracold Gases 34

4 Magnetic phase diagram of a 2D S=1 condensate 35
4.1 Introduction 35
4.2 Review of spinor condensate without magnetic dipole interaction 36
4.2.1 Confinement 40
4.2.2 Precession 41
4.3 Magnetic dipole interaction 41
4.4 Analytical Results 43
4.4.1 Weak dipole interaction 43
4.4.2 Magnetic plaquettes 46
4.4.3 Magnetic helix 47
4.5 Numerical Results 48
4.5.1 Numerical treatment of the dipole term 50
4.5.2 Domain walls in $F_{\|}$ 50
4.5.3 Boundaries and trapping potential 51
4.6 Discussion 51

5 Detecting fractional quantum Hall phases in optical lattices 56
5.1 Introduction 56
5.2 The model 57
5.3 Circular trapping potential 59
5.4 Elliptical trapping potential 62
5.5 Discussion 64
5.6 Conclusions 65

IV Quantum Spin Chains 66

6 E_8 symmetry effects in perturbed quantum Ising chains 67
6.1 Perturbed quantum Ising chains 67
6.2 Theoretichal model of $CoNb_2O_6$ 68
6.3 Time evolution 69
6.4 Excitation spectra for a quantum Ising chain 72
6.5 Excitation spectra for $CoNb_2O_6$ 73
6.6 Conclusions 73

7 Quantum phases for anisotropic XXZ-chains 76
7.1 Introduction . . . 76
7.2 The model . . . 77
7.3 Quantum phase transitions . . . 78
7.3.1 Quantum phases . . . 78
7.3.2 First order transition . . . 79
7.3.3 Second order transition . . . 79
7.3.4 BKT transition . . . 79
7.3.5 Central charge . . . 81
7.4 Phase diagrams . . . 83
7.4.1 Phase Diagram (Δ,D_2) . . . 83
7.4.2 Phase digram (D_2,D_4) . . . 83
7.4.3 Odd Haldane phase . . . 86
7.4.4 Even Haldane phase . . . 88
7.5 $S = 3$ XXZ-chain . . . 89
7.6 Discussion . . . 91

Bibliography 93

List of Figures

1.1 An example of the continuous vanishing of an order parameter through a phase transition. The higher χ is, the more accurate is the numerical simulation. The exact meaning of χ will be explained in Ch. 3. 12
1.2 The fractal structure called Hofstadter's butterfly; the energy spectra as a function of magnetic field for a non-interacting (single) particle on a 2-D square lattice. 14

3.1 The entanglement spectra for a infinite spin-1 AFM Heisenberg chain. 28
3.2 Top; diagrammatic representation of an iMPS formed by the tensors Γ and Λ. The horizontal line represents the bond indexes $\alpha_{A,B} = 1, \ldots, \chi$ and the vertical lines the physical indexes $D_{A,B} = 1, \ldots, d$. Unitary operators acts on the physical indexes. Only operators that commutes with each other acts simultaneously as described in the previous section. Repeated use according to a Suzuki-Trotter decomposition leads to a real (or imaginary) time evolution for a time t (τ). . . 30
3.3 Update scheme for unitary two-site transformations of an MPS in the canonical form (see text for details). 31
3.4 (Figure layout to be updated) Entanglment (color coded) after a local perturbation on site $k = 64$ as a function of bond the cut is made at (x-axis) and time (y-axis) in Jt. 32
3.5 (Figure layout to be updated) Time evolution of the correlation function as a function of Jt for $\chi = 10$(green), $\chi = 15$(blue), $\chi = 20$(red) and $\chi = 25$(black) on the site the spin was flipped on at $t = 0$. 33

4.1 (Color online) Examples of possible spin configurations in the plane. The external fields are along the horizontal axis, $M_z(x, z)$ is plotted on the horizontal axis, $M_x(x, z)$ is on the vertical for every plaquette and $M_y(x, z)$ is not shown. (a) Uniform fully magnetized $F_\parallel$, (b) striped fully magnetized $F_\parallel$, (c) uniform partly magnetized $F_\perp/P_\parallel$ state, (d) helical fully magnetized $F_\perp$ 39
4.2 (Color online) Ground state phase diagram of a spin-1 condensate without dipolar interaction; from Mukerjee *et al.*. [49] 40

4.3 (Color online) Ground state phase diagram for a spin-1 condensate with dipole interaction and external fields, that introduces a quadratic Zeeman term and rapid spin precession. Both polar and ferromagnetic phases appear, perpendicular as well as parallel to the field. 45
4.4 (Color online) Transverse magnetization as a function of z, from numerical simulation. Orange: magnitude of total magnetization M_0, blue: transverse magnetization in plane M_x and black: transverse magnetization out of plane M_y. A helical modulation with wavelength $\lambda \approx 85$ μm is clearly visible. Simulation values: $|\tilde{c}_2|\bar{n}_{3D} = 320$ Hz, $c_d\bar{n}_{3D} = 0.8$ Hz and $q = 100$ Hz (edges removed). . . . 49
4.5 (Color online) Transition to $F_\perp/P_\parallel$ from $F_\parallel$. (a) For q slightly smaller than q_{c2}, large Mermin-Ho vortices appear between the stripes (plaquette size $a = 4$ μm). $M_z(x, z)$ is plotted on the horizontal axis, $M_x(x, z)$ on the vertical axis and $M_y(x, z) \approx 0$ for the whole region shown at this instant. (b) Consequently, the maximum value of the Fourier transform of the magnetization out of plane $M_x(k_z^{max})$, see Eq. (4.46), increase before the phase transition. Simulation variables: $|\tilde{c}_2|\bar{n}_{3D} = 450$ Hz, $c_d\bar{n}_{3D} = 7.2$ Hz and $q = 35$ Hz (a), $q = 30 - 39$ Hz (b). 52
4.6 (Color online) Transition to $P_\perp$ from $F_\parallel$. The parallel magnetization $M_z(z/a)$ is plotted for different values of $|\tilde{c}_2|\bar{n}_{3D} = 2.4 - 4.8$ Hz as a function of z/a. The magnetization is lowered at the boundaries around the transition point for a finite system. Simulation values: $N = 20 \times 20$, $c_d\bar{n}_{3D} = 5.7$ Hz and $q = -4$ Hz. 53
4.7 (Color online) Simulation of a helical modulated magnetized condensate in an elliptical trap. $\bar{n}_{3D}(x, z)M_z(x, z)$ is plotted on the horizontal axis, $\bar{n}_{3D}(x, z)M_x(x, z)$ on the vertical axis, and $M_y(x, z)$ is a quarter of a wavelength ahead of $M_x(x, z)$ as in Fig. 4.4, but is not shown. The wavelength $\lambda(z)$ of the helical modulation increases with decreasing density along the longitudinal axis. The distance between two neighbouring nodes is shown; the node to the left of them is outside the graph. Simulation parameters: $v_z = 1$, $v_x = 10$, $|c_2|\bar{n}_{3D} = 540$ Hz, $c_d\bar{n}_{3D} = 1.6$ Hz and $q = 120$ Hz. 53

5.1 (Color online) (a) Part of the square lattice in the symmetric gauge with the phases gained when hopping in the direction of the arrows. When hopping in the opposite direction, the phases are the complex conjugate of those shown. (b) The bulk gap in the $\nu = 1/2$ phase on a cylinder as a function of flux per plaquette, for $N = 4 - 6$ particles. The large red cross is from a clearly different spectrum, indicating that it might not be in a FQH phase. 58

5.2 (Color online) (a) Analytic edge spectrum at $\nu = 1/2$ in a trap as a function of angular momenta. Degenerate lines are drawn slightly apart for clarity. The solid lines corresponds to excitations consisting of four single particle modes or less. The dashed dotted lines are the additional excitations appearing for additional modes. (b)-(d) Edge excitations for $N = 4$ particles on a 11×11 square lattice in a circular harmonic trap, $\nu = 1/2$ black solid lines, $\nu = 2/3$ blue dashed lines and the possible Read-Rezayi (RR?) phase, red dashed dotted lines. (b) Edge spectrum at $n_\phi = 1/5$ as a function of angular momentum. (c) Energy gap to the $\nu = 1/2$ ground state for: ground states ($\circ$), 1 states ($\triangle$), 2 states ($\times$) and 3 states ($\bullet$), labeled as in Tab. 5.1, as a function of flux per plaquette. (d) Edge spectrum at $n_\phi = 1/8$ as a function of angular momentum. 61

5.3 (Color online) (a) Edge spectrum for $N = 4$ particles at $\nu = 1/2$ on a 9×15 site cylinder in a harmonic trap as a function of momenta. Apart from the expected edge spectrum (black solid lines), bulk excitations (red dash-dotted lines) and edge excitations from translated $\nu = 1/2$ phases (blue dashed and magenta dashed-dotted lines, where the former are aliased to a lower momenta) are mixed in. Two-fold degenerate states are marked with longer lines. (b) Analytic edge spectrum at $\nu = 1/2$ for a large system. Degenerate lines are drawn slightly apart for clarity. 63

6.1 (Color online) (A) Ising spins on the Co^{2+} ions are strongly coupled in 1D along zig-zag chains. The Co^{2+} ions are ordered in a weakly coupled triangular lattice in the plane perpendicular to the chain direction, with **a**, **b** and **c** orthogonal unit vectors. (B) Confinement of kinks: the potential energy between kinks increase linearly, along the z coordinate in the **c** direction, as more interchain bonds turn energetically unfavorable. The energy levels are given by the negative zeros of the Airy function. (C-D) The full Hamiltonian describing $CoNb_2O_6$ at no external magnetic field. (C) The dynamical structure function. (D) The cross section of (C) at zero momentum showing the masses of the first five bound states. A comparison of these masses from our MPS calculations (pluses) with the experimental results (circles) and the exact solution of the proposed first order phenomenological model (crosses). 70

6.2 (Color online) Ising chain in a transverse and a longitudinal field. (A) The dynamical structure function at $h^x = h_c^x$ and $h^z = 0.035$ meV. (B) The cross section of (A) at zero momentum. The five lowest bound states and two bound state pairs can be distunguished. (C) ($h^x = h_c^x$) The mass of the four lowest bound states and an asymptotic expansion for m_1 from $h^z \to 0$ as a function of the longitudinal field. (D) ($h^x = h_c^x$) Relative mass of the lowest bound states compared to the analytical predicted values at $h^z \to 0$. (E) ($h^z = 0.035$ meV) The bound state masses as a function of the transverse field (h^x). The energy gap is smallest around $h^x = 1.10$ meV, however the minimum in the higher bound states occurs for lower fields. (F) ($h^z = 0.035$ meV) The relative masses for the bound states increases roughly linear as a function of the field (h^x) and passes the analytical calculated values at h_c^x. 71

6.3 (Color online) The full Hamiltonian describing $CoNb_2O_6$. (A) Magnetization comparison between weakly coupled chains and chains in different constant longitudinal field. (B) The cross section of the dynamical structure function for h_c^x at zero momentum showing the masses of the first five bound states and two bound state pairs. (C) The bound state masses as a function of h^x. The minimum gap is above h_c^x and the bound state mass minimum decreases with increasing mass. (D) The ratio of the bound state masses varies linearly around h_c^x and goes through the analytically calculated values at h_c^x. 75

7.1 Examples of how to locate phase transitions with iDMRG data. (a) First order transition; Energy level crossing in the ground state. Red dashed line indicates the continuation of the energy level where it is not the ground state anymore. Note also that the energy is well converged in χ in iDMRG. (b)-(d) Second order transition. (b) Transition from a magnetized to a non-magnetized phase. (c)-(d) The entanglement entropy and correlation length go to infinity $S \to \infty$ and $\xi_0 \to \infty$ as $\chi \to \infty$ at the transition point. (c)-(d) BKT transition; Hard to locate in these diagrams. The critical phase is the region where the entanglement entropy and correlation length go to infinity $S \to \infty$ and $\xi_0 \to \infty$ as $\chi \to \infty$. . . 80

7.2 (a) S as a function of $log(\xi)$ for $\chi = 25, 35, 50, 70, 100, 140, 200, 280, 400, 560, 800, 1120$, black circles. Close to a QCP there is a linear relation between them, red dashed line. The system moves away from criticality with increasing χ. A linear fit to the data from the three largest χ gives a different slope, black line. (b) Linear fit of the data at three different χ to the Eq. 7.4. The red dashed line shows the transition to the critical phase with $c = 1$. 82

7.3 Phase diagram for $S = 2$ as a function of Δ and on-site anisotropy D_2. The phases detected with iDMRG are the large colored regions; AFM, XY and EH phases. Red dashed line show the previous calculated XY phase boundary with DMRG [106]. Solid red line, the calculated XY phase boundary with ED+LS [107]. Solid blue line, the calculated Oh phase boundary with ED+LS [107]. 84

7.4 Central charge calculations to find the critical phase as in Fig. 7.2, along different vertical lines in the phase diagram Fig. 7.3. The critical phase is where $c = 1$ extends over a finite range, like in (a) and likely (b), marked with vertical red dashed lines. 85
7.5 Phase diagram for $S = 2$ as a function of the on-site anisotropies D_2 and D_4 at $\Delta = 1$. The phases detected with iDMRG are the colored regions; AFM, XY, EH and OH phases. 86
7.6 String order calculations for different χ's and scaled to $\chi \to \infty$ (solid line) along the line (Eq. 7.5). Smaller χ gives a larger SO. The SO vanish at $D_4 \approx= 0.1$. At $D_4 = 0$ it has vanished for all χ's. 87
7.7 Phase transitions in the $S = 3$ XXZ-chain. (a) The vanishing of the magnetization order parameter $|\langle S_n^z \rangle|$ as a function of $1/\chi$, black circles and scaled to the limit $\chi \to \infty$, red dashed line. (b) The peak in the correlation length ξ_0 indicated the transition between the FM and the OH phase. (c) Central charge calculations gives the transition to the critical phase, red dashed line. (d) String order calculations at the AFM Heisenberg point. For small χ it is in the AFM phase, for $\chi \gtrsim 800$ it is in the OH phase and it scales linear with χ, red dashed line. 90

Acknowledgments

Looking back on my road into physics, there are many people without whom I would not be where I am today. My math and physics teacher Kenneth Karlsson at Peder Skrivares Gymnasium got me interested in physics through his encouragement and love of phyiscs and teaching. At Chalmers University of Technology my interest in physics deepened from the many knowledgeable professors whose classes I attended and the challenging problems they presented. I especially want to mention Stellan Östlund and Lars Brink who together with my fellow student Tomas Rube convinced me to apply for graduate school in the United States. I spent countless of hours with Tomas during my senior year studying theoretical physic and solving hard problems and I was very lucky having him move to Stanford at the same time as I moved here.

At UC Berkeley I have had many amazing physics teachers, I especially want to mention professors Joel Moore, Ashvin Vishwanath and Dan Stamper-Kurn, who I have enjoyed many interesting physics conversation with and who are a great inspiration to me. Joel and Ashvin are also on my thesis committee, together with Rachel Segalman. Their input to this thesis is greatly appreciated. Of course, Joel is also my advisor and his friendliness and constant belief in me has been a great support during my time here. His deep insight into physics, especially the research presented here has been invaluable.

I have been very fortunate to have many other great collaborators from whom I have learned a lot. My fellow students and office mates Andrew Essin, who thaught me much about how to do research, Michael Zaletel and Roger Mong. The researchers Frank Pollmann and Jens Bárðarson who always have had their door open and ready to discuss problems with me. I have also enjoyed many stimulating discussions with other physicists in my field here in Berkeley, including Vasudha Shivamoggi, Gil Young, Itamar Kimchi, Pavan Hosur, Yi Zhang, Marianne Rypestøl, Christoph Karrasch, Roni Ilan, Tarun Grover and Siddharth Parameswaran.

I also want to thank all my friends in Berkeley, both inside and outside the physics department, who are far to many to mention individually, but you know who you are anyway. Without you I would not have had the energy to pursue my research. You have made my years in Berkeley very memorable and among the best in my life so far!

Finally, I of course have to thank my family for their support and love. My parents who always have been there for me and at the same time encouraged me to go my own ways. As long as I can remember, they have challenged my curiosity and and most important, believed

in me. Frida, who has been a great sister, always ready to talk to me.

List of Acronyms

1D	one-dimensional
2D	two-dimensional
3D	three-dimensional
AFM	antiferromagnetic
BEC	Bose-Einstein condensate
DMRG	density matrix renormalization group
ED	exact diagonalization
EH	even Haldane
FM	ferromagnetic
FQH	fractional quantum Hall
iDMRG	infinite density matrix renormalization group
iTEBD	infinite time evolving block decimation
IQH	integer quantum Hall
LS	level spectroscopy
MI	Mott insulator
MPS	matrix product state
OH	odd Haldane
SF	superfluid
SO	string-order
TEBD	time evolving block decimation
QCP	quantum critical point

Part I

Introduction

Chapter 1

Brief introduction to magnetism

Magnetism is a property of a system, describing its response to external magnetic fields. It is one of the oldest mysteries of solids and remains a very active research area. Magnetic materials have been known to mankind for thousands of years around the world. The earliest known discussions about it can be traced back to the ancient Greeks and Chinese about 2500 years ago. Perhaps, its most famous use, as an instrument to determine the cardinal directions in navigation, or in short a compass, started to spread around China and Europe almost a thousand years ago. However, the underlying cause of the magnetic properties of these materials, remained a mystery up to about a hundred years ago with the formulation of quantum mechanics. Magnetic properties of solids are quantum mechanically in nature and classic physics can not fully explain them. Magnetic fields can arise from two different fundamental sources; moving electric charges and the intrinsic magnetic moment of particles. While Maxwell s classic electromagnetism describe the fields that arises from electrical currents, the currents producing the magnetic behavior of materials comes from the motion of the electrons. Both electrons orbiting the atomic nucleus and unbound electrons moving around in a system require a quantum mechanical description to explain the origin of magnetism. While the underlying mechanisms of magnetism by now is well studied and understood, many interesting questions remain. The magnetic interaction is long ranged and materials consists of a huge amount of particles $\sim 10^{23}$, making a complete treatment of those systems impossible. However, much progress has been made both in experimental and theoretical condensed matter physics where various successful approximations have been develop. Many important questions have been answered, but also many remain, including some of the simpler to state.

With the recent progress in engineering materials down to the atomic level, lower dimensional materials like sheets and wires are becoming increasingly more common and important. The push for smaller and smaller components in the electronic industry is the main driving force behind this. Quantum mechanical effects becomes more prominent as the dimension of the system is decreased. This introductory chapter will first summarize the basic known facts of magnetism and then briefly introduce some interesting research areas with magnetism in 1-D and 2-D systems. The main part of this dissertation will present some recent research

done within this field.

1.1 Classic magnetism

In Maxwell s classic theory of electromagnetism [2], no magnetic monopoles exist

$$\nabla \cdot \mathbf{B}(\mathbf{x}) = 0, \tag{1.1}$$

where $\mathbf{B}(\mathbf{x})$ is the magnetic field at position $\mathbf{x}$. Instead, the sources to steady magnetic fields are charge currents

$$\nabla \times \mathbf{B}(\mathbf{x}) = \frac{4\pi \mathbf{j}(\mathbf{x})}{c} + \frac{1}{c}\frac{\partial \mathbf{E}(\mathbf{x})}{\partial t}, \tag{1.2}$$

where $\mathbf{j}(\mathbf{x})$ is the current at $\mathbf{x}$ and c is the speed of light. The last term in Eq. 1.2 couples a rapidly varying electric field $\mathbf{E}(\mathbf{x})$ to a rapidly varying magnetic field, through a similar equation for the electric field leading to electromagnetic waves.

The macroscopic description of a material has a density of magnetic moments $\mathbf{M}(\mathbf{x})$, from current loops $\mathbf{j}_{mag} = \nabla \times \mathbf{M}(\mathbf{x})$ within it [3, 4]. The magnetic field within a sample created from external sources are hence

$$\mathbf{H}(\mathbf{x}) = \mathbf{B}(\mathbf{x}) - 4\pi \mathbf{M}(\mathbf{x}). \tag{1.3}$$

The response of a material in terms of its internal magnetic moments to an external magnetic field is

$$\chi_{ab} = \frac{\partial M_a}{\partial H_b}, \tag{1.4}$$

where χ_{ab} are the tensor components of the magnetic susceptibility. For a linear isotropic media χ is a scalar. A material with $\chi > 0$ is paramagnetic, it strengthens the magnetic field within the material with a general alignment of the magnetic moments with the external field. Materials with $\chi < 0$ are named diamagnetic. As the temperature is lowered, many materials develops a spontaneous magnetic order. Above the transition temperature they normally are paramagnets with

$$\chi = \frac{1}{T - \Theta}, \tag{1.5}$$

where T is the temperature and Θ the Curie-Weiss temperature, which normally do not coincide with the transition temperature T_c. Some material like iron have a surprisingly large transition temperature $T_c^{Fe} = 1042$ K.

An isolated current distribution has a magnetic dipole moment

$$\mathbf{m} = \int d^3x \frac{1}{2c} \mathbf{x} \times \mathbf{j}(\mathbf{x}) \tag{1.6}$$

The total Lorentz force on a current distribution is then

$$\mathbf{F} = \frac{1}{c} \int d^3x \mathbf{j}(\mathbf{x}) \times \mathbf{B}(\mathbf{x}) = ... = \nabla(\mathbf{m} \cdot \mathbf{B}), \tag{1.7}$$

where the current distribution is assumed to vanish outside some small area. The magnetic field is roughly constant within that area and can be Taylor expanded around its central value $\mathbf{B}(\mathbf{x}) = \mathbf{B}(0) + (\mathbf{x}\cdot\nabla)\mathbf{B}(0) + ...$ Hence, the potential energy of a dipole in a magnetic field is

$$U = -\mathbf{m}\cdot\mathbf{B}, \tag{1.8}$$

indicating that dipoles want to align with the magnetic field and are paramagnetic. However, this assumes that the current is constant while the dipole align itself with the field. A free charge q, experiencing the force $\mathbf{F} = q\mathbf{v}\times\mathbf{B}$, creates a magnetic moment in the opposite direction of the field and is hence diamagnetic. The actual motion of charged particles in material are governed by quantum mechanics and together with the pure quantum mechanical intrinsic magnetic moment of particles will be the focus when quantum magnetism are described in the next two sections.

1.2 Atomic Magnetism

Before one can start to understand the origin of magnetism in materials, it is important to understand it in an atom [3, 4]. The Hamiltonian governing an atoms interaction with an external magnetic field is

$$H = \frac{1}{2m}\sum_i \left(\mathbf{p}_i + e\mathbf{A}(\mathbf{r}_i)\right)^2 + \mu_B B(\mathbf{r}_i) S_i^z, \tag{1.9}$$

where the sum goes over all the electrons in the atom. The i^{th} electron has a momentum $\mathbf{p}_i$ at position $\mathbf{r}_i$. Electrons are elementary particles and are indistinguishable. They have exactly the same properties, mass m, charge $q = -e$, where e is the fundamental unit of charge, and spin (or intrinsic angular momentum) $s = 1/2$, which is related to its magnetic moment $\mathbf{m}_e \approx -2\mu_B\sqrt{s(s+1)}$. The first term in Eq. 1.9 describes the orbital motions interaction with the magnetic field and the second the spins interaction with the magnetic field. The electromagnetic vector potential $\mathbf{A}(\mathbf{r})$ is related to the magnetic field $\mathbf{B}(\mathbf{r}) = \nabla\times\mathbf{A}(\mathbf{r})$. The dominant magnetic energy contribution after performing perturbation theory wants to align the moments with the field, a paramagnetic contribution,

$$\Delta E_1 = \mu_B B(L^z + 2S^z) + ..., \tag{1.10}$$

unless the outer shell is filled or one electron short of half full in which case it vanishes. In second order of the magnetic field there is a diamagnetic contribution,

$$\Delta E_2^d = \frac{e^2B^2}{12m}r^2, \tag{1.11}$$

competing with another paramagnetic term. The diamagnetic contribution comes from the last part of the first term and is easiest derived in the symmetric gauge $\mathbf{A}(\mathbf{r}) = 1/2(-By, Bx, 0)$, using $x^2 + y^2 \approx 2/3(x^2 + y^2 + z^2) = r^2$.

Electrons are fermions, since they have half integer spin, and follow Fermi-Dirac statistics and obey the Pauli exclusion principle [5]. That is, only one particle can occupy a particular quantum state at a specific time. In a finite quantum system, the conserved quantities can only take on discrete values, called quantum numbers. For example, the electrons in an atoms electrostatic field can be well approximated by a central potential. In such a system the atomic orbitals can be described by the quantum numbers for the shell n, the angular momentum l and m_l and the spin $s = 1/2$ and m_s. The quantum numbers for the i^{th} electron are closely related to the corresponding physical observables, obtained in the bra-ket notation of quantum mechanics when the operators act on the eigenstates, labeled by the quantum numbers; the angular momentum

$$\mathbf{L}_i^2|l_i\rangle = l_i(l_i+1)\hbar^2/(4\pi)^2|l_i\rangle, \tag{1.12}$$

spin angular momentum

$$\mathbf{S}_i^2|s\rangle = s(s+1)\hbar^2|s\rangle, \tag{1.13}$$

and their projection along a specified axis in the atom

$$L_i^z|m_{l_i}\rangle = m_{l_i}\hbar|m_{l_i}\rangle \text{ and } S_i^z|m_{s_i}\rangle = m_{s_i}\hbar|m_{s_i}\rangle. \tag{1.14}$$

In the ground state, the electrons start to fill the innermost shells, which has $2n^2$ positions for $n = 1, 2, 3, .$, since $l = n-1, n-2, ..., 0$, $m_l = -l, -l+1, ..., l$ and $m_s = -1/2, 1/2$. The total angular momentum $\mathbf{J} = \mathbf{L} + \mathbf{S} = \sum_{i=1}^N \mathbf{L}_i + \sum_{i=1}^N \mathbf{S}_i$, where the sum is over all the electrons, is defined in the same way as for $\mathbf{L}$ and $\mathbf{S}$, with

$$\mathbf{J}^2|J\rangle = J(J+1)\hbar^2|J\rangle \text{ and } J_z|m_J\rangle = m_J\hbar|m_J\rangle. \tag{1.15}$$

All filled shells have zero total angular momentum $\mathbf{J} = 0$ (and also $\mathbf{S} = 0$ and $\mathbf{L} = 0$). The magnetic moment of an atom is related to its angular momentum through the relation $\mathbf{m}_{ATOM} = g_J\mu_B\mathbf{J}$. Hund's rules describe in which order the atomic orbitals inside each shell gets occupied.

1. The electrons occupy the orbitals with the largest total spin angular momentum S^z.
2. Given 1., the electrons occupation maximize L^z.
3. Given 1 and 2, for a less than a half full shell, the total angular momentum J^z is minimized. If more than half full, J^z is maximized.

Also, the j^{th}h nucleon has an intrinsic angular momentum or spin $\mathbf{I}_j$ and a corresponding magnetic moment. The magnetic moment of the electron is about 10^5 times larger than the nucleons and the latter can hence often be neglected. However, in atomic experiments, the precision of the electromagnetic fields are high enough to resolve the hyperfine splitting of the energy levels from the nucleons magnetic moment in an external magnetic field. In Ch. 4 that analyze an ultracold atomic experiment the nuclear magnetic moment also needs to be

taken into account. The total atomic angular momentum is $\mathbf{F} = \mathbf{I} + \mathbf{J}$, where $\mathbf{I}$ is the total intrinsic nuclear angular momentum of the atom. The orbitals of the nucleons do also form a shell like structure, with $\mathbf{I} = 0$ for a filled shell. Without going into details about how this is built up and the order the nucleons fill those orbitals, the quantum number of the total nuclear angular momentum I is a multiple of $1/2$ times a small integer.

1.3 Magnetism in condensed matter

Condensed matter physics deals with condensed phases of matters, primarily solids and liquids. It is many body systems, normally with huge number of particles. Often, the interactions between the particles are weak and all the interactions a particle experience can be approximated with an average interaction with its surrounding. The effective single particle problem that arises through this approximation is easier to analyze and normally gives good predictions. However, for certain systems it can not explain all observations and a multi-particle approach is necessary. These systems are called strongly correlated. In this dissertation we will primarily investigate these kind of systems, see Ch. 5, 6 and 7. However, we will also investigate one system where the interparticle interactions can be approximated with an effective interaction, see Ch. 4.

In the very simplest model of a metal, the electrons move around freely without interacting with the other electrons or the ions [3, 4]. Let us begin with briefly discuss how this system responds to an external magnetic field. First we consider the intrinsic magnetic moment of the electrons. Without a magnetic field there is an equal distribution of spin up and down electrons. With a magnetic field, the interaction with the spins $-2\mu_B B S^z$ raises the Fermi level for spins pointing in the opposite direction to the spins and lower it for the opposite spins, creating an unequal spin distribution. Electrons are negatively charged particles, so the magnetization points in the opposite directions to the spins, resulting in a magnetic susceptibility

$$\chi = \frac{4\pi\mu_B^2 k_F m}{\pi^2\hbar^2} \tag{1.16}$$

that is paramagnetic. However, as was noted in the previous section the motion of a free charge has a diamagnetic contribution. As an example, the orbiting motion of free electrons in a 2-D structure will be discussed in more detail in Sec. 1.7. Here we just state the result, that the diamagnetic contribution from the electrons motion is one third of the paramagnetic

$$\chi = -\frac{4\pi\mu_B^2 k_F m}{3\pi^2\hbar^2}. \tag{1.17}$$

However, for a more accurate treatment of magnetism in materials the interactions between the particles need to be considered. A magnetic dipole $\mathbf{m}_1$ creates a magnetic field

$$\mathbf{B} = \frac{3\hat{r}(\mathbf{m}_1 \cdot \hat{r}) - \mathbf{m}_1}{r^3}, \tag{1.18}$$

a distance $\mathbf{r}$ away from it. Another dipole $\mathbf{m}_2$ a distance $\mathbf{r}_{12}$ away from the first dipole will have a potential energy in its magnetic field

$$V_d = -\mathbf{m}_2 \cdot \mathbf{B} = \frac{\mathbf{m}_1 \cdot \mathbf{m}_2 - 3(\mathbf{m}_2 \cdot \hat{r}_{12})(\mathbf{m}_1 \cdot \hat{r})}{r_{12}^3} \tag{1.19}$$

The maximum energy decrease in a dipole field is obtained when the dipoles are aligned along the line separating them. This energy decrease is only $1 \cdot 10^{-3}$ eV for a typical inter atomic spacing ~ 1 Å in solids, which corresponds to a temperature of about 1 K. However, magnetism can be detected in many materials up to about 1000 K, well above where it would have been expected to vanish from the above calculation. Instead, the correct explanation for magnetism in material is, like in the atom, about finding certain quantum spin states that minimizes the coulomb interaction between the electrons, while obeying the Pauli exclusion statistics, similar to Hund's rules for atoms.

Let us consider the hydrogen molecule H_2 as an example for how an effective spin Hamiltonian can be derived from a Hamiltonian without any spin terms [6]. H_2 has two protons on sites $\mathbf{R}_{1,2}$ and two electrons at positions $\mathbf{r}_{1,2}$ occupying the atomic wave functions $\phi_{1,2}$. The Hamiltonian is

$$H = \sum_{i=1}^{2} H_i + \Delta H, \tag{1.20}$$

where

$$H_i = \frac{\hbar^2}{2m}\nabla_i^2 - \frac{e^2}{|\mathbf{r}_i - \mathbf{R}_i|} \tag{1.21}$$

is the isolated atomic Hamiltonian with ground state energy ϵ. The interaction between the two parts is

$$\Delta H = -\frac{e^2}{|\mathbf{r}_1 - \mathbf{R}_2|} - \frac{e^2}{|\mathbf{r}_2 - \mathbf{R}_1|} + \frac{e^2}{|\mathbf{r}_1 - \mathbf{r}_2|} + \frac{e^2}{|\mathbf{R}_1 - \mathbf{R}_2|} \tag{1.22}$$

Minimizing the energy $E = \langle\Psi|H|\Psi\rangle / \langle\Psi|\Psi\rangle$, with respect to the constants $c_{a,b}$ in the total wavefunction $\Psi = (c_a\phi_1(\mathbf{r}_1)\phi_2(\mathbf{r}_2) + c_b\phi_1(\mathbf{r}_2)\phi_2(\mathbf{r}_1))\chi$, where χ is the spin part, leads to the matrix equation

$$\left[\begin{pmatrix} V_d & V_o \\ V_o^* & V_d \end{pmatrix} - (E - 2\epsilon)\begin{pmatrix} 1 & \lambda^2 \\ \lambda^2 & 1 \end{pmatrix}\right]\begin{pmatrix} c_a \\ c_b \end{pmatrix} = 0, \tag{1.23}$$

with

$$\lambda = \int d^3r \phi_1^*(\mathbf{r})\phi_2(\mathbf{r}), \tag{1.24}$$

$$U_d = \int d^3r_1 d^3r_2 \Delta H |\phi_1(\mathbf{r}_1)\phi_2(\mathbf{r}_2)|^2 \tag{1.25}$$

and

$$U_o = \int d^3r_1 d^3r_2 \Delta H (\phi_1(\mathbf{r}_1)\phi_2(\mathbf{r}_2))^* \phi_1^(\mathbf{r}_2)\phi_2(\mathbf{r}_1). \tag{1.26}$$

The solution of Eq. 1.23 is

$$E^{\pm} = 2\epsilon + \frac{V_d \pm V_o}{1 \pm \lambda^2} \tag{1.27}$$

for the wavefunctions

$$\Psi^{\pm} = \frac{1}{2}[\phi_1(\mathbf{r}_1)\phi_2(\mathbf{r}_2) \mp \phi_1(\mathbf{r}_2)\phi_2(\mathbf{r}_1)][\chi^{\uparrow}(\mathbf{r}_1)\chi^{\downarrow}(\mathbf{r}_2) \pm \chi^{\uparrow}(\mathbf{r}_2)\chi^{\downarrow}(\mathbf{r}_1)], \tag{1.28}$$

which are antisymmetric as they have to be for fermions. For the hydrogen molecule

$$E^{+} - E^{-} = 2\frac{V_d\lambda^2 - U_o}{1 - \lambda^4} = J > 0, \tag{1.29}$$

the wavefunction with the antisymmetric spin part has the lower energy and an effective Hamiltonian can be constructed

$$H = J\mathbf{S}_1 \cdot \mathbf{S}_2 \tag{1.30}$$

where the $\mathbf{S}_{1,2}$ is the spin-1/2 operator acting on the atomic orbital on site $1, 2$. This Hamiltonian has an energy $-3/4J$ if acting on a spin singlet $S_{tot} = 0$ which is antisymmetric and $1/4J$ if acting on a spin triplet $S_{tot} = 1$ which is symmetric. Even if the original Hamiltonian has no spin-dependent terms through the Fermi statistics the energy difference arising from the Coulomb interaction and the kinetic energy can instead be attributed to the spin configuration.

Using other atomic orbitals than the Hydrogen s in the above calculation will give other values for J. Spatially separated orbitals, but not orthogonal, normally give rise to an antiferromagnetic interaction $J > 0$, while orthogonal orbitals that occupy the same region in space normally give a ferromagnetic interaction $J < 0$ in accordance with Hund's rules. For many electrons occupying many orbitals it can be even more complicated. In some systems an exact spin model can be derived, but many times a spin model that gives an approximate description of the system is used. Many spin models have also been studied that does not yet have a known realization in any material. Those models could be either for future use or for investigation of interesting properties where the solution can be beneficial in understanding other systems. In this dissertation we will investigate an Ising like spin chain in Ch. 6 that is a good model for $CoNb_2O_6$ and compare to some experimental results. We discuss briefly why the particular spin model we are using describe this material well. In Ch. 7 we study a spin-2 model, which has no known physical realization, but gives insight in how highly quantum mechanical systems with low spins are related to the classical limit $S \to \infty$.

1.4 Quantum phases and phase transitions

In the previous section we argued that the interactions between the electrons in a system could lead to an effective Heisenberg model, Eq. 1.30) with either FM ($J < 0$) or AFM ($J > 0$) interactions. A simple picture of a FM groundstate has all the spins pointing in the

same direction, and an AFM groundstate neighboring spins pointing in opposite directions. The question arises, is it possible to move smoothly without closing the gap between these two ground states by modifying the Hamiltonian. The answer is no, since the two states belong to different phases [4, 6–8]. Traditionally, Landau's symmetry breaking theory was believed to explain all different phases. A phase is simply defined as a region in phase space where the ground state wavefunctions have the same symmetries.

At sufficiently high temperature any system turns into a gaseous phase, which is completely disordered. Acting on a state in this phase with any symmetry operator will leave its expectation values unchanged. Upon lowering the temperature many systems condense into some kind of phase with more order, like a solid. The continuous translational and rotational symmetries are broken down to some discrete version. Apart from various lattice structures, also metallic, semiconducting, superconducting, superfluid, and magnetic phases among others can be explained with Landau's symmetry breaking theory.

Many phase transitions are driven by thermal fluctuations and more ordered phases with less symmetry appears as the temperature is lowered. However, even at zero temperature there are fluctuations, quantum fluctuations. By varying some physical parameter, like J in Eq. 1.30, a quantum phase transition can occur, driven by quantum fluctuations. For low temperatures, both thermal and quantum fluctuation are important and needs to be considered. In this dissertation we will mainly deal with systems at zero temperature, which are a good approximation to any system at very low temperature where the quantum fluctuations dominate.

To understand phase transition, an important concept is correlations. The correlation function measures how correlated one point is with another point a distance $\mathbf{x}$ away. It is defined as

$$\Gamma(\mathbf{x}) = \langle O(\mathbf{x})O(0)\rangle - \langle O(\mathbf{x})\rangle\langle O(0)\rangle, \tag{1.31}$$

where $O(\mathbf{x})$ is the order parameter or some other operator for a quantum system one is interested in the correlations of and $\langle\rangle$ is the thermal statistical average in a classical system or the expectation value in a quantum system. A rapid decay in $\Gamma(\mathbf{x})$ shows that fluctuations at one point does not affect the system far away. Instead it is the local interactions that dominate the physics of the system. A slow decay on the other hand means that fluctuations have a large effect on points far away and the system can get organized in larger structures not directly obvious from the local Hamiltonian. Close to a critical point the correlation function normally gets a form like

$$\Gamma(x) \to x^{-q}e^{-x/\xi}, \tag{1.32}$$

where ξ is the correlation length. It measure over what distance fluctuations are important or correlated. The correlation lengths diverge at many critical points. In fact, different types of critical points are divided into different classes;

- First order phase transition: Some properties, like the order parameter shift discontinuously, a (normally large) amount of latent heat is released or absorbed if it is a

temperature driven transition. No divergence in the correlation lengths

- Second order phase transition: The order parameter of one phase change continuously to zero at the transition to the other phase. Diverging correlation lengths and some other physical observables like susceptibility and entanglement entropy in quantum systems at the transition.

- Infinite order phase transitions: A phase transition between a gapped phase and a critical or gapless phase. The order parameter of the gapped phase also change continuously to zero at the transition to the gapless phase. The correlation length and other physical observable diverge at the transition to the gapped phase and remains infinite inside the gapless phase.

More detailed discussion of different types of phase transitions with several examples will be presented in Ch. 7. Ch. 4 and Ch. 5 also investigate different phases and some interesting observations are made about the transitions betweem them in those chapters as well.

With the discovery of the fractional quantum hall (FQH) phases in 1982, it was realized that there exist different quantum phases that have the same symmetry [8, 9]. This goes beyond Landau's symmetry breaking theory and a new theory had to be developed to explain these phases. These quantum phases are named topological phases if they are gapped. They can not be described by a local order parameter, long range correlations or as mentioned some broken symmetry. Instead, they can have different ground state degeneracy on different manifolds, in the thermodynamic limit, quasiparticle statistics and edge spectra. The first two of these do not uniquely define a topological phase, but the edge spectra is believed to do it. In Ch. 5 we will study the edge spectra of topological FQH phases in optical lattice and argue that it is the best way to experimentally detect these phases in ultracold gases.

The above definition of a topological phase is somewhat restrictive and does not incorporate some 1-D phases that can not be described by a local order parameter. An example is the Haldane phase around the Heisenberg point in a $S = 1$ chain, which will be discussed in detail in Ch. 7. This phase has no ground state degeneracy in a periodic system, but instead in an open system. The decomposed $S = 1/2$ edge spin is completly free. It has no exotic quasi-particle statistic, since it is a 1-D system. It also has long range correlations close to the phase transitions. This phase needs certain symmetries to remain stable and not turn into the trivial phase, and is normally called a symmetry-protected topological phase.

1.5 Spin chains

One of the easiest type of models to investigate quantum phase transitions in are quantum spin chains [6, 7]. From a theoretical point of view systems are generally easier to analyze as the interaction gets shorter and the dimension of the system lower.

Earlier we argued that the electron interaction could create an effective Heisenberg spin interaction, see Eq. 1.30. In many materials there are several different types of atoms that

can make the distance to the magnetic ions different in different directions. Since atomic interactions fall off very fast with distance, many material can hence to a good descripton be described by a 1-D or 2-D spin structure. Also, the spins in themselves can have a preferred component, so an anisotropy parameter Δ is introduced, that takes the system away from the Heisenberg point $\Delta = 1$. The Hamiltonian for the infinite quantum XXZ spin chain is

$$H_{\text{XXZ}} = \sum_n (S_n^x S_{n+1}^x + S_n^y S_{n+1}^y + \Delta S_n^z S_{n+1}^z), \tag{1.33}$$

where S_n^α ($\alpha = x, y, z$) is the α-component of the spin-S operator at the n^{th} site and Δ is the XXZ anisotropy parameter. For $S = 1/2$ there are three phases; FM, XY and AFM for increasing Δ. At the Heisenberg point, this Hamiltonian has a $SU(2)$ spin symmetry, which it is invariant under. Away from the Heisenberg point a $U(1)$ symmetry in the xy-spin plane remains and a $\mathbb{Z}_2$-symmetry in the z-component $S^z \to -S^z$. The magnetized phases breaks the $\mathbb{Z}_2$ symmetry. In the FM phase all spins can be either up or down and in the AFM the up spin can be on either the odd or even sites. The order parameter for the magnetized phases is $|\langle S_n^z \rangle|$. An example of the continuous decrease of this order parameter as Δ is varied can be seen in Fig. 1.33. This example is an infinite order phase transition, at $\Delta = 1$, between a gapped AFM phase and a critical gapless XY phase. Other types of phase transitions are normally easier to locate. More details about various phase transitions will be presented in Ch. 7.

Quantum mechanical effects are stronger the lower S. In the limit $S \to \infty$ the spins behave classically. But already for small S the interaction is predominantly classic and a classic analyze can often be done to obtain most of the information about a system. In Ch. 7, the focus is on integer spin XXZ-chains with onsite anisotropies, especially the $S = 2$ case and we also investigate how the classic limit develops as S increase.

As the spin anisotropy Δ gets stronger, another perhaps even more famous model appear. In the limit $\Delta \to \infty$, while $J \to 0$ so that $\Delta J = 1$ remains constant the Ising spin chain emerges

$$H_{\text{Ising}} = \sum_n S_n^z S_{n+1}^z. \tag{1.34}$$

This is deep inside the AFM phase (or the FM phase if the other limit is taken). Normally a transverse field h_x is added, so this model can be tuned through a phase transition to the trivial paramagnetic phase. This phase is also gapped, but has not broken any symmetry of the Hamiltonian, it is hence the same phase as would appear if the temperature was raised past a thermal phase transition. In Chap. 6 we will discuss a material that is close to the Ising limit, and with some other weak interactions present as well.

Spin models are many times good approximation to solid state systems, but it can be hard to exactly tune them in the desired way. In the last decade advances in ultracold gases has opened up for experimental investigation of spin models with a previously unprecedented control. Atoms with the desired spin are placed in optical lattices and their interaction can be easily tuned by external fields. Sec. 1.8 will give a brief introduction to ultracold gas experiments.

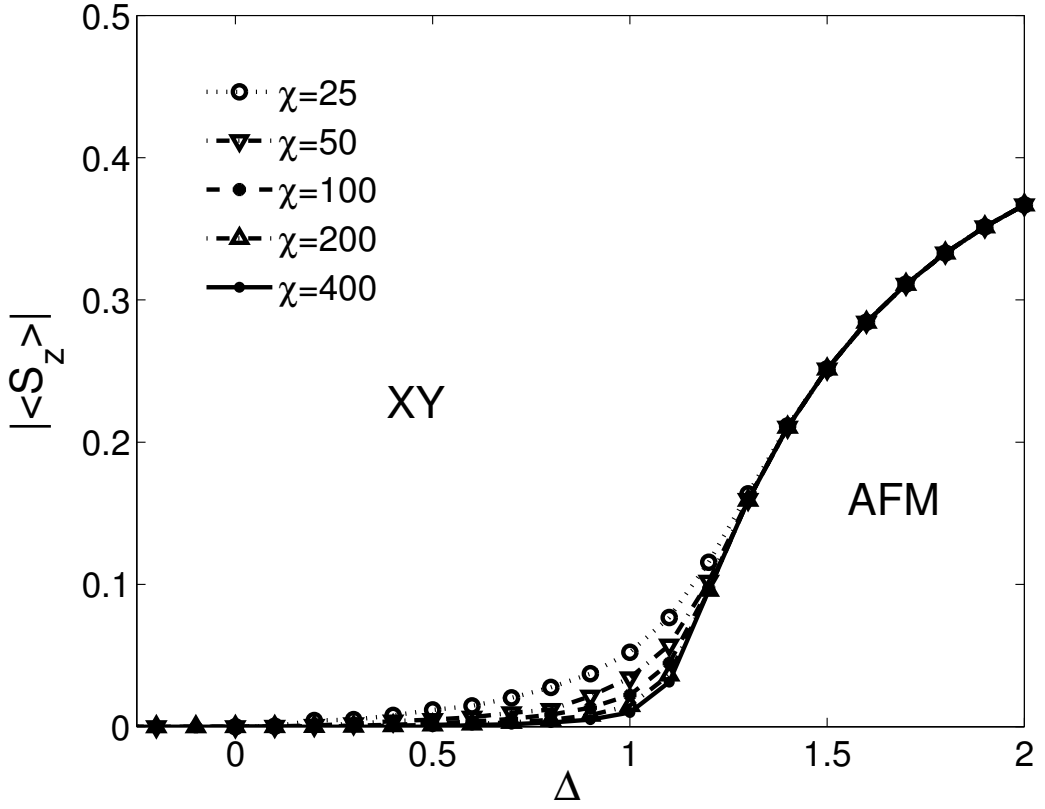

Figure 1.1: An example of the continuous vanishing of an order parameter through a phase transition. The higher χ is, the more accurate is the numerical simulation. The exact meaning of χ will be explained in Ch. 3.

1.6 Bose-Hubbard model

Another very important model within strongly correlated physics is the Hubbard model [7]. It was originally developed as a model describing the transition between an insulating phase and a conducting phase. It is an improved tight binding model where an electron can interact with another electron at the same site in a different atomic orbital in addition to their hopping between different atomic orbitals located on different lattice sites. In its original form, two s-orbitals are located on every lattice site, one for $m_s = 1/2$ and one for $m_s = -1/2$.

A similar model can also be constructed for bosons, it is then called the Bose-Hubbard model. It has been realized with ultracold gases and has been a great system to study quantum phases and phase transitions in. Since several bosons can occupy the same orbital,

only one orbital per lattice site is normally used leading to the Hamiltonian

$$H = -J \sum_{\langle i,j \rangle} \hat{a}_i^\dagger \hat{a}_j + \hat{a}_j^\dagger \hat{a}_i + \frac{U}{2} \sum_i \hat{n}_i(\hat{n}_i - 1), \tag{1.35}$$

where $\langle i, j \rangle$ is the sum over nearest neighbor sites, J is the hopping amplitude, U the onsite repulsion, $\hat{a}_i^\dagger$ and $\hat{a}_i$ are the boson creation and annihilation operator and $\hat{n}_i$ counts the number of bosons on site i. In the Hubbard model, the boson operators in the hopping term in the Bose-Hubbard model are replaced by the fermion creation and annihilation operators $\hat{c}_i^\dagger$ and $\hat{c}_i$ and the interaction term reads $U \sum_i \hat{n}_{i,\uparrow} \hat{n}_{i,\downarrow}$, only a contribution when both orbitals on site i are occupied. The Bose-Hubbard model is superfluid (SF) for large J and turns into a Mott insulating (MI) phase at some lower J depending on the filling fraction. Similar to filled atomic shells, each filled layer of bosons, where the number of bosons is a multiplet of the number of sites have little effect on the systems, leading to the so called Mott lobes.

1.6.1 Hofstadter's Butterfly

Non-interacting bosons $U = 0$ is a simple model to solve, since it is a single particle model. However, adding a magnetic field on a square lattice creates a very interesting structure, called the Hofstadter's Butterfly after its discoverer [10]. The magnetic field is easiest added as a phase change in the hopping amplitude, that corresponds to the phase $\alpha = 2\pi n_\phi$ a particle gains when it moves around the flux n_ϕ. Using the Landau gauge, the Hamiltonian reads

$$H = -J \sum_{\vec{r}} \hat{a}_{\vec{r}+\hat{x}}^\dagger \hat{a}_{\vec{r}} e^{-i\alpha y} + \hat{a}_{\vec{r}+\hat{y}}^\dagger \hat{a}_{\vec{r}} + h.c., \tag{1.36}$$

where the sites are at $\vec{r} = (x, y)$. Simulating for $\alpha = (0.0 : 0.001 : 1.0)$ on up to a 2×1000 site lattice leads to a fractal image, when the energy spectrum is plotted as function of α, see Fig. 1.2.

In Ch. 5 we combine these two models Eq. 1.35 and Eq 1.36, interacting Bosons in a magnetic field. We focus on the limit $U \to \infty$, since it is slightly easier to analyze with the decrease in Hilbert space from $D = \binom{M+N-1}{N}$ to $D = \binom{M}{N}$, where M is the number of sites and N the number of bosons. Also, as we will show in Ch. 5, as long as no phase transition occurs out of the phase, a change in U has a marginal impact on the result.

1.7 Quantum Hall

An unexpected response to an external magnetic field was observed in an experiment by von Klitzing, Dorda and Pepper in 1980 [11]. In a Hall measurement, a steady current j_x, is flowing in the $\hat{x}$ direction in perpendicular magnetic B_z and electric E_y fields, whose forces

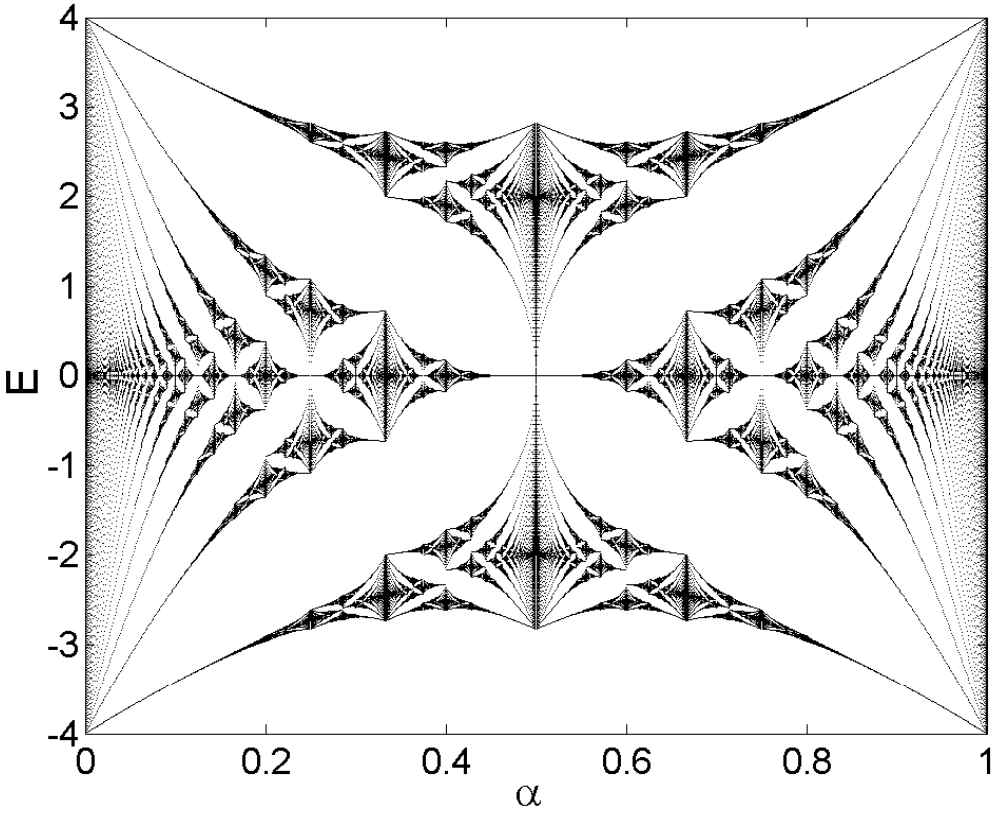

Figure 1.2: The fractal structure called Hofstadter's butterfly; the energy spectra as a function of magnetic field for a non-interacting (single) particle on a 2-D square lattice.

on the moving charges cancel $qE_y = qv_xB_z$. The measured conductivity tensor σ is defined as $\mathbf{j} = \sigma\mathbf{E}$. Its transverse conductivity element

$$\sigma_{xy}^{\text{classic}} = \frac{j_x}{E_y} = \frac{n_c e}{B_z} \tag{1.37}$$

is expected to be proportionell to $1/B_z$. This has been a very reliable method to measure the charge density n_c in a sample. However, they observed an exact quantization of σ_{xy} at low temperature in a 2-D electron gas in a strong magnetic field

$$\sigma_{xy}^{\text{quantum}} = \frac{\nu}{h/e^2}, \tag{1.38}$$

where ν are integers. That is, σ_{xy} is constant for some range of B_z , before rapidly decreasing to the next quantized value for another range of B_z. A quantization of a macroscopic observable, the conductivity, in a macroscopic sample was very unexpected. A lot of experimental and theoretical work followed on this discovery and it was soon realized that the

quantization was very accurate, to about 1 part in a billion [12]. Nowadays the standard for resistance is defined from the basic quantum of resistance $R_K = h/e^2$. Measurements of the longitudinal conductivity σ_{xx} is zero where σ_{xy} is constant.

Treating the conduction electrons as free particles moving in the xy-plane in an external perpendicular magnetic field B_z, it is straightforward to see that they are quantized in certain energy levels, called Landau levels [4, 9]. The Hamiltonian for such a particle is

$$H = \frac{1}{2m}\left(\mathbf{p} + \frac{e}{c}\mathbf{A}(\mathbf{r})\right)^2. \tag{1.39}$$

Choosing Landau gauge $\mathbf{A} = (0, Bx, 0)$, we see that the operator $\hat{p}_y$ commutes with the Hamiltonian and can be replaced with its eigenvalue $\hbar k_y$. The resulting Hamiltonian is a 1-D Harmonic oscillator

$$H = \frac{\hat{p}_x^2}{2m} + \frac{1}{2}m\omega_c^2\left(\hat{x} + \frac{\hbar k_y}{m\omega_c}\right)^2 \tag{1.40}$$

shifted in coordinate space and with energy eigenvalues $E_n = \hbar\omega_c(n + 1/2)$, where $\omega_c = eB/mc$ is the cyclotron frequency and n an integer quantum number. The Landau levels E_n are degenerate since the quantum number in the y-direction k_y does not affect the energy. In a periodic sample with length L_y it can take on the values $k_y = 2\pi N/L_y$, where N is a positive integer such that the center of the Harmonic oscillator stays within the sample $\frac{\hbar k_y}{m\omega_c} < L_y$, or $N < \frac{m\omega_c L_x L_y}{2\pi\hbar}$. The number of electronic orbitals in the lowest Landau level is hence

$$N_e = \frac{BL_xL_y}{hc/e} = \frac{\Phi}{\Phi_0} = N_\phi, \tag{1.41}$$

which is the same as the number of flux quanta $\Phi_0 = hc/e$ trough the system. For none polarized electrons (both spin up and down) there are twice as many electronic orbitals. Each flux penetrate an area $2\pi l_B$, where $l_B = \sqrt{h/eB}$ is called the magnetic length.

In a perfect sample, in an increasing external magnetic field, the next Landau level would start to fill immediately after the previous is completly filled, so why can a quantized conductivity be measured? The answer is maybe a bit surprisingly due to impurities. Impurities create localized states around them and some of those will be in the energy gap between the extended states of adjacent Landau levels. It is very hard to make a "perfekt" material without any impurities and often they can partly obscure the effect that one wants to measure, but for the IQH they do not, in fact they are essential for the quantization.

In 1992, only two years after the discovery of the IQH effect, quantized conductivity was measured at fractional fillings $\nu = p/q$, with p and q integers, by Tsui *et. al.* [13]. To have incompressible phases at partly filled Landau levels require interactions between the electrons, since otherwise there would be a huge ground state degeneracy $\sim \frac{N_\phi!}{N!(N_\phi - N)!}$, where N is the number of electrons. Consequently a completely different theory needed to be developed. The wavefunction for a single particle in a magnetic field, the solution to Eq. 1.40 is $\Psi_0 = f(z)e^{-|z|^2/4/l_B^2}$, where $f(z)$ is an analytic function. Laughlin constructed

the following wavefunction to explain the fillings at $\nu = 1/m$ with m an integer

$$\Psi_{1/m}(z_i) = \prod_{i<j}(z_i - z_j)^m e^{-\sum_i |z_i|^2/4l_B^2}, \tag{1.42}$$

where $z = x + iy$ is a function of the 2-D coordinates (x, y). This wavefunction describes fermions for odd m, for which it is totally antisymmetric. The wavefunction has an m-order zero, which describe the strong electron repulsion well. It is an incompressible state with uniform density within a disc.

The model we presented in the previous section, interacting bosons on a lattice in a magnetic field can be in FQH phases [14]. In Ch. 5 we will investigate how these phases can be detected and also see the transitions between some of them.

1.8 Experimental techniques

Most of the research presented in this dissertation has a close connection to experiments. In this section we give a quick introduction to two selected experimental techniques that are relevant to the research presented in this dissertation; ultracold gases that can be used to investigate magnetism in a very controlled setting and neutron scattering that is used to map out the magnetic structure and excitations in the solid state.

1.8.1 Ultracold gases

A Bose-Einstein condensate (BEC) in a dilute quantum gas was obtained for the first time in 1995 by Wiemann and Cornell's group at Jila and Ketterle's group at MIT [15, 16]. They managed to trap a gas of alkali atoms ^{87}Rb and ^{23}Na respectively and cool it to a sufficiently low temperature for the gas to Bose-Einstein condense. Since this original achievement, the field has experienced a rapid development. Notable achievements include, the tuning of the interactions through a Feshbach resonance, trapping in an optical trap where the spin degrees are free, different trapping potentials including lattices and lower dimensional condensates as well as a multitude of detection techniques.

Each research group has their own slightly different way of creating a BEC, although most of the general features remain the same. Here I will give a very brief summary of the experiment I am most familiar with, the "Spinor Rubidium BEC" in Stamper-Kurns group at UC Berkeley. For more information about the experiment, see one of the excellent Ph. D.-dissertations written by the former graduate students in that group [17–19].

Liquid Rb in equilibrium with its vapor is kept in an oven with a small opening through which the Rb-gas can move towards the experimental chamber. The flux of Rb out from the oven is determined by the gas pressure through the temperature. At a typical temperature of 100°C about 10^{16} atoms/s leave the oven. However of these atoms in thermal equilibrium

only about 1/60000 leaves the oven in the right direction and continue into the Zeeman slower.

Inside the Zeeman slower is a counter propagating laser beam that slows down the atoms through scattering. The Zeeman slower creates a magnetic field that keep the majority of the atoms in resonance with the laser beam as their velocity is decreasing. Exiting the Zeeman slower, the majority of the atoms have a velocity 20 m/s, down from the thermal average velocity of 300 m/s they had when they entered.

This is low enough to be efficiently trapped in the magneto-optical trap. About $5 \cdot 10^9$ atoms are trapped during the 10 second and then compressed and cooled in several steps to $60 - 70$ μK. The atoms are then transferred to a magnetic trap where they are evaporated cooled through a radio-frequency laser that changes the magnetic quantum number. They can be expelled from the trap by the magnetic field, leading to a lower average temperature, around the transition temperature to a Bose-Einstein condensate. Finally, the condensate is loaded into the optical dipole trap. Without a magnetic trapping field the spins of the atoms can move freely. A spatially varying Stark shift creates an attractive force directed towards the center of the trap. Using different frequencies in the different directions leads to a condensate with different extensions in those directions.

Two of the main detection techniques used to probe ultracold gases are time of flight and *in-situ*. In time of flight, the condensate is released from the trap and allowed to expand. No further interactions between the atoms are assumed to take place. The atoms position after a long enough time, will be related to the momentum distribution that was present in the trap just before they were released. An experiment normally takes a couple of seconds and many are performed under the same conditions to create good statistics. In an *in-situ* measurement the condensate interact directly with an electromagnetic wave, that is assumed to give continuous information about the condensate without affecting it. Due to the smallness of the condensate a high resolution imaging technique is essential, on the order of μm or better.

Today there are ultracold gas experiments operating all over the world and new ones are cosntructed continiously. This subsection is way to short to give it any kind of justification to all the experiments and what they have measured and plan to measure. For the interested readers one of the reviews of the field is a good start. A fairly general one is Ref. [20] by Bloch, Dalibard and Zwerger. More specific ones, one related to the work presented in Ch. 4 is Ref. [21] by Stamper-Kurn and Ueda, and another related to the work in Ch. 5 is Ref. [22] by Cooper. These review articles should be a good starting point to other review articles as well as original work in the field.

1.8.2 Neutron scattering

Neutrons are a very important probe in the investigation of the structure and dynamics of materials [23]. They are charge less and can hence penetrate deeper into solids than what charged particles can. Their magnetic moment makes them well suited to investigate magnetic properties. Their wavelength at room temperature $\lambda \approx 1.8$ Å is one the same

order as the typical interatomic distance in solids, so interference effects can be used to get information about the structure. Cold neutrons $\sim 0.1-100$ meV, can be used to investigate elementary excitations. One of the biggest challenges with neutron scattering is two have a reliable neutron source with large enough flux of neutrons. There are two main types of neutron sources, reactor and spallation. The emerging neutrons are very energetic and needs to be slowed down in a moderator to be useful. Their magnetic moment are unpolarized and for magnetic measurements it can be useful to polarize them. The differential scattering cross section for a neutron $\mathbf{k}_i$ scattering into $\mathbf{k}_f$, where $\mathbf{k}$ is the momentum, is

$$(\frac{d\sigma}{d\Omega})_{\mathbf{k}_i\to\mathbf{k}_f} = \frac{1}{N}\frac{k_1}{k_0}(\frac{m}{2\pi\hbar^2})^2 \sum_{\lambda_0\sigma_i} p_{\lambda_0}p_{\sigma_i} \sum_{\lambda_1\sigma_f} |\langle \mathbf{k}_f\sigma_f\lambda_1|V|\mathbf{k}_i\sigma_i\lambda_0\rangle|^2\delta(E+E_{\lambda_0}-E_{\lambda_1}), \quad (1.43)$$

where we average over all initial states λ_0 of the sample occuring with probability p_{λ_0} and the initial polarization of the neutrons σ_i with probability p_{σ_i}. We sum over all the final state of the sample λ_1 and of the outgoing polarization of the neutron σ_f.

To investigate magnetic excitations in a solid, the lattice structure and the dynamics of the spins needs to be taken into account

$$\begin{aligned}\frac{d^2\sigma}{d\Omega dE} =& \frac{1}{N_m}\frac{k_1}{k_0}\frac{(\gamma r_0)^2}{2\pi\hbar}\sum_{\alpha\beta}(\delta_{\alpha\beta}-\hat{\mathbf{q}}_\alpha\hat{\mathbf{q}}_\beta)\sum_{ii'} f_i^*(\mathbf{q})f_{i'}(\mathbf{q}) \\ &\times \int \langle \mu_{i\alpha}(0)\mu_{i'\beta}(t)\rangle\langle e^{-\mathbf{q}\mathbf{R}_i(0)}e^{-\mathbf{q}\mathbf{R}_{i'}(t)}\rangle e^{-iEt/\hbar}dt,\end{aligned} \quad (1.44)$$

where N_m is the number of magnetic ions, $r_0 = e^2/m_ec^2$ the classical radius of the electron, $\mathbf{q} = \mathbf{k}_i - \mathbf{k}_0$ and $f_i(\mathbf{q})$ is the atomic form factor for an atom localized on lattice site $\mathbf{R}_i$. The magnetic moment of the neutron is $\mu_n = -\gamma\mu_N\sigma$.

Chapter 2

Overview of dissertation

The dissertation is divided into three parts. In Part II we give an overview of the main numerical techniques used in the dissertation; classical Monte Carlo, exact diagonalization and matrix product state based techniques. In Part III we analyze two different experiments with ultracold gases that investigate phases for trapped bosons in an external magnetic field. In Part IV we investigate some quantum spin chains. One of them was initiated by results from a remarkable neutron scattering experiment.

Part II has only one chapter.

- Ch. 3, "Simulating quantum systems," gives a quick introduction to some different techniques used to simulate quantum systems. We start with a quick overview of the classical Monte Carlo algorithm, using a spin-1 model on a square lattice as an example. Next, we discuss exact diagonalization, using a hard-core Bose-Hubbard model on a square lattice as an example. We show how to use the translational symmetry to speed up the calculations and get the energy as a function of momentum. Finally, we discuss the matrix product state based techniques; density matrix renormalization group and time evolving block decimation. We consider both ground state calculations and dynamics after a quench.

Part III consists of two chapters.

- Ch. 4, "Magnetic phase diagram of a 2D S=1 condensate," examines the phase diagram of a 2D spin-1 condensate trapped in an elliptical potential when the dipole-dipole interaction is taken into account. Non-trivial order develops in both ferromagnetic phases, with magnetic domains respectively a helical structure. The transition between the two phases with vortex development is also studied. The work was completed in collaboration with Andrew M. Essin and Joel E. Moore, published at Ref. [24].

- Ch. 5, "Detecting fractional quantum Hall phases in optical lattices," investigates the edge spectra for bosonic fractional quantum Hall phases in an optical lattice. Different phases are found and their stability and the phase transition between them are

investigated, We show that the edge spectra is a good way to experimentally detect the different phases. The work was completed in collaboration with Joel E. Moore, published at Ref. [25].

Part IV consists of two chapters.

- Ch. 6, "E_8 symmetry effects in perturbed quantum Ising chains ," was motivated by an experiment on $CoNb_2O_6$, a material that closely resembles a quantum Ising chain, when it was tuned close to the QCP. Signature of the expected Lie algebra E_8 was seen in the excitation spectra. We investigate an accurate model of $CoNb_2O_6$ close to the QCP, taking into account interactions not previously investigated. The signatures of the weakly broken E_8 symmetry remains and are clearer than expected. The work was completed in collaboration with Frank Pollmann and Joel E. Moore, published at Ref. [26].

- Ch. 7, "Quantum phases for anisotropic XXZ-chains," investigates the development of the classical limit from a quantum XXZ spin-chain with onsite anisotropies, focusing on the $S = 2$ phase diagram. An almost classical phase diagram is found in the basic plane, but it is proven that a narrow region still connects the Heisenberg point with the trivial phase. The symmetry protected topological phase in the $S = 1$ phase diagram around the Heisenberg point can be reached for a wide range of certain onsite anisotropies. The work was done in collaboration with Michael Zaletel, Roger Mong, Jens H. Bárðarson and Frank Pollmann, to be published.

Part II

Numerical Techniques

Chapter 3

Simulating quantum systems

In this chapter we will briefly discuss the numerical techniques used later in this dissertation. The first section is about the Monte Carlo technique that is used in Ch. 4. The second section introduce exact diagonalization used in Ch. 5. The last section presents the matrix product state based techniques, with focus on time evolving block decimation used in Ch. 6 and density matrix renormalization group used in Ch. 7.

3.1 Monte Carlo

The Monte Carlo algorithms are a family of computational algorithms relying on repeated random numbers. Probably the most commonly used in condensed matter physics is the quantum Monte Carlo algorithm. The one we will discuss in this section is a classical Monte Carlo algorithm [27], that will be used later, see Ch. 4. The first step is to generate a starting configuration. It can be a random configuration or an ordered one. Each step of the main algorithm follow the same procedure. First, the old state is saved. A new state is randomly chosen from some distribution that contains all realizable numbers. In our case we have a spin-1 condensate, discretized on a 2-D $M_x \times M_y$ lattice. At each lattice point a 3-component complex vector

$$\sqrt{n_{2D}(r,s)}\psi(r,s) = \begin{pmatrix} a(r,s)+ib(r,s) \\ c(r,s)+id(r,s) \\ e(r,s)+if(r,s) \end{pmatrix} \tag{3.1}$$

is defined, where r and s are integers between $1 \leq r,s \leq M_x, M_y$. To create a new state we first pick a random lattice site (r,s) followed by picking a random component a, b, c, d, e, or f of the vector at that site (r,s). A new value for that component is then randomly obtained from a Gaussian distribution. Note, that the vector $\sqrt{n_{2D}(r,s)}\psi(r,s)$ is not normalized and each component can in principle take on any value independent of the others. To keep the total particle number around the desired value, a chemical potential $\mu \sum_{r,s=1}^{M_x,M_y} n_{2D}(r,s)$ is added to the Hamiltonian in the code. The mean of the Gaussian distribution is chosen so that the correct particle number from the chemical potential is a likely outcome and its

deviation is chosen as a compromise between easy exploration of the whole phase space and good convergence.

Lastly the energy of the new configuration is calculated. If it is lower than the previous, the new state is kept. If it is higher, the new state is kept if

$$e^{-\delta E/k_B T_{MC}} \leq \zeta, \tag{3.2}$$

where ζ is a randomly picked number $\zeta \in [0, 1)$, otherwise not. This process is repeated many times, normally $\gtrsim 10^6$, until the total energy reaches a minimum. Depending on the symmetry of the phase one might need to be aware of local minima. Some local minima can be possible to get out from by modifying T_{MC}. Others could require different starting conditions. Multiple simulations are then performed and the one with the lowest final energy is the ground state.

The parameter T_{MC} is called the Monte Carlo temperature and it controls the dynamics of the simulation. It is not directly related to the physical temperature of the system and the dynamics is not necessarily the physical dynamics either, although it can normally give good insight into it. The best use of the algorithm is that it normally can find the ground state of the system in an efficient way. The Monte Carlo temperature T_{MC} used is like the Gaussian deviation also decided from simulation optimization. In the end it is confirmed that the final result is independent of these parameters for a wide range of values.

3.2 Exact Diagonalization

Exact diagonalization (ED) is in principle a very simple and powerful technique. Diagonalizing matrices, that is finding its eigenvalues and its eigenvectors, is a common mathematical problem that appears in many fields. Consequently, there are efficient codes available for all major coding languages. In quantum mechanics the Hamiltonian is defined in matrix form and the exact energy eigenvalues E_n and energy eigenkets $|n\rangle$ are obtained

$$H|n\rangle = E_n|n\rangle. \tag{3.3}$$

Knowing the full energy eigenspectra with all associated eigenstates of a system, it is straight forward to calculate the interesting properties of the system including dynamical ones.

However, for quantum problems there is a major limitation associated with this approach, the rapid growth of the Hilbert space. As an example, consider the $S = 1/2$ chain. It is a discrete quantum system with a local Hilbert space dimension $d = 2S + 1 = 2$. However the global Hilbert space $dim(\mathcal{H}) = d^n$ grows exponentially with the number of sites n. For example, a system with only $n = 10$ sites has a Hilbert space with dimension $2^{10} = 1024$ and requires the diagonalization of a 1024×1024 matrix. Luckily, many of the physical Hamiltonians are sparse, that is most entries are zero, and a lot of memory can often be saved if only the value and the position in the matrix of the non-zero elements are stored. Many times one is not interested in the full eigenvalue spectra of a huge matrix, but only a

handful of the lowest energy eigenvalues. For sparse matrices there are codes that do this very efficiently. Depending on the particular matrix, today a regular laptop can normally calculate eigenvalues of Hilbert space on the order of millions of states.

What has been described so far is simple and straight forward to implement. However, it is possible to exactly solve somewhat larger systems by taking advantage of the symmetries present in the Hamiltonian. Doing this, the matrix will be put into block diagonal form, where all the nonzero matrix elements are collected into blocks along the diagonal. The blocks corresponds to a conserved quantity, conjugate to the symmetry variable. For example in a Hamiltonian with translational symmetry, blocks corresponding to a certain linear momentum can be created. Implementing the symmetries of the Hamiltonian normally requires a fair amount of work.

In the rest of this section I will explain the ED code I wrote for bosons in optical lattices, see Ch. 5. It is a problem closely related to the Bose-Hubbard model on a square lattice introduced in Ch. 1. We write down the Hamiltonian, Eq. 1.35, again for convenience

$$H = -J \sum_{\mathbf{r}} \hat{a}^\dagger_{\mathbf{r}+\hat{x}} \hat{a}_{\mathbf{r}} + \hat{a}^\dagger_{\mathbf{r}+\hat{y}} \hat{a}_{\mathbf{r}} + h.c. + \frac{U}{2} \sum_i \hat{n}_i(\hat{n}_i - 1), \tag{3.4}$$

where J is the hopping amplitude, $\hat{a}^\dagger_{\mathbf{r}}$ creates a boson on site $\mathbf{r} = (x, y)$ and $\hat{n}_{\mathbf{r}} = \hat{a}^\dagger_{\mathbf{r}} \hat{a}_{\mathbf{r}}$ gives the number of particles on site $\mathbf{r}$.

We start with writing an algorithm that defines all the quantum states of the problem. Since the Hamiltonian acts on the real space, we define them in terms of site occupation. When the onsite interaction goes to infinity $U \to \infty$, see Ch. 1, only one particle can occupy every site and the last term in Eq. 3.4 can be ignored. The dimension of the Hilbert space reduces to $D = \binom{M}{N}$, where N is the number of particles and M the number of sites. The states are saved in a $D \times N$ matrix V, where the i^{th} row correspond to the i^{th} state. The first multiparticle state we define is one particle on each of the sites $V(1,:) = (1, 2, .., N)$, where the lattice sites can be numbered in some convenient way. The next state is created by moving the last particle one site $V(2,:) = (1, 2, .., N-1, N+1)$. This is repeated until the last particle is at the last site $V(M-N+1,:) = (1, 2, .., M)$. Then, the second to the last particle is moved one site and the last particle is placed just after it $V(M-N+2,:) = (1, 2, .., N-2, N, N+1)$. Then the last particle is moved one site at a time until it reaches site M. Whenever the last particle can not be moved anymore, one checks if the second to last particle can move one site, if it can not, then the third to the last is checked, then the next and so on until a particle is found that can move. Once that particle is found, all particles at higher site numbers are moved as close to it as is possible on the higher side. This is done until no more particles can move $V(D,:) = (M - N + 1, ..., M)$. All possible D states are now defined.

To be able to find the states quickly if we are given a random state it is important to have an easily calculated label for each. This can be done by defining the labels

$$v(i) = \sum_{j=1}^{N} V(i, j) \cdot M^{(j-1)}. \tag{3.5}$$

To quicker find the state in V corresponding to $v(i)$, we sort v from the lowest to the highest value. The same reshuffling is done for the rows in V.

After these preliminary steps, it is time to calculate the values of the matrix elements. This is done by looping through all the D quantum states in V. For each quantum state $V(i,:)$, we act with the Hamiltonian on it. If it only contains nearest neighbor interactions on a square lattice, the J-terms in Eq. 3.4, it will give us four other quantum states in V

$$H|i\rangle = -J|i^{(1)}\rangle - J|i^{(2)}\rangle - J|i^{(3)}\rangle - J|i^{(4)}\rangle. \tag{3.6}$$

Depending on the boundary conditions used, some of these might not be allowed and needs to be discarded. Having obtained these new quantum states, we calculate their labels $\{v(i^{(a)})\}$, as in Eq. 3.5, to find out which quantum states $\{V(i^{(a)},:)\}$ they correspond to. In the Hamiltonian we save the matrix elements $-J$ on sites $\{(i,i^{(a)})\}$. Since we know the Hamiltonian is Hermitian, only the quantum states $i^{(a)} \leq i$ needs to be calculated by this procedure. When the full Hamiltonian is obtained it is diagonalized with a sparse eigensolver to obtain the n lowest energy eigenvaules and eigenstates.

Adding a magnetic field will change some of the matrix elements to $-Je^{-i\phi}$ for some value ϕ. More importantly, it will destroy some translational symmetry depending on the gauge and the boundary conditions. We implemented two different conserved quantities in two separate pieces of code for the simulations presented in Ch. 5, from the translational symmetry that remains around a cylinder (and a torus) in Landau gauge and from the rotational symmetry that remains on a square in symmetric gauge.

Here we briefly describe how the translational symmetry was implemented. Consider a cylinder with M_x sites around it. We start out obtaining all quantum states as above, however we also need to know which states are related by translational symmetry. For every state we translate the whole state $m = 1, 2, ...$ and $M_x - 1$ sites, for example

$$(1, 2, .., N) \rightarrow \text{ sort}((1+m, 2+m, .., N+m) \text{ mod } M), \tag{3.7}$$

to create M_x states $\{V(i^{(b)},:)\}$ related by the symmetry. Before proceeding, we check if all the states related by the translational symmetry are different or if they have a higher translational symmetry M_x/I, where I is an integer. For example the two particle state $(1, M_x/2+1)$ has a $M_x/2$-site translation symmetry and only the first $M_x/2$ states are kept. For each set of states related by symmetry, one state $V(i^{(b')},:)$ is picked as the basic state, the one with lowest value on its label $v(i^{(b')})$. For each state in this set we save the translational symmetry of the set $M_x/I(i)$ and the label $v(i^{(b')})$ of the basic state. The basic quantum states are also saved separately in a matrix $\tilde{V}(i^{(b')},:)$.

To create the nonzero entries of the matrix we loop through the basic quantum states $\tilde{V}(:,:)$ and act with the Hamiltonian on them as in Eq. 3.6. For the states $\{V(i^{(a)},:)\}$ obtained in this way we check which is theirs basic quantum states $\{\tilde{V}(i^{(a')},:)\}$. A matrix $A_{i^{(b')},i^{(a')}}$ with dimension $M_x/I(i^{(b')}) \times M_x/I(i^{(a')})$ from the two basic quantum states is constructed with elements corresponding to all the translated states from these two basic quantum states.

Due to the translational symmetry of the Hamiltonian, the non-zero matrix elements should be the same on all diagonals wrapping around the matrix;

$$A_{i^{(b')},i^{(a')}} = \begin{bmatrix} a & b & 0 & 0 \\ 0 & a & b & 0 \\ 0 & 0 & a & b \\ b & 0 & 0 & a \end{bmatrix}. \tag{3.8}$$

Note, if acting with the Hamiltonian creates two different quantum states that belongs to the same basic quantum states they need to be treated together. This matrix is then Fourier transformed with a discrete Fourier transform

$$\tilde{A}_{i^{(b')},i^{(a')}}(k_x, k_{x'}) = \sum_{x=0}^{M_x/I(i^{(b')})} \sum_{x'=0}^{M_x/I(i^{(a')})} A_{i^{(b')},i^{(a')}}(x, x') e^{-2\pi i (k_x \cdot x/(M_x/I(i^{(b')}) + k_{x'} \cdot x'/(M_x/I(i^{(a')})))}, \tag{3.9}$$

both along the rows and the columns. If necessary additional rows and or columns with zeros are inserted to make the final matrix a $M_x \times M_x$ matrix. For example if $I(i^{(a')}) = 2$, the additional columns $2, 4, ..., M_x$ needs to be inserted. From the resulting diagonal matrix, the non-zero diagonal elements are stored at site $(i^{(b')}, i^{(a')})$ in M_x matrices corresponding to each of the conserved quantities $k_x = 0, 2\pi/M_x, .., 2\pi(M_x - 1)/M_x$. These M_x matrices are then diagonalized as above with a sparse matrix eigenvalue solver to find the n lowest eigenvalues and eigenstates for each momentum $k_x = 0, 2\pi/M_x, .., 2\pi(M_x - 1)/M_x$.

3.3 Matrix Product State based methods

Density matrix renormalization group (DMRG) was invented by Steve White in 1992 [28**?**]. Initially it was a method to mainly calculate the ground state of finite discrete 1-D quantum many-body systems. In 2003 Guifré Vidal invented another method, time evolving block decimation (TEBD), that in addition also could simulate real time evolution for the same type of systems [29]. A few years later this method was extended to infinite systems infinite TEBD (iTEBD) [30]. Altough DMRG was formulated with matrix product states (MPS) fairly early [31, 32], it took several years, until TEBD was developed, for the wider community to recognize its usefulness. Soon it was realized that DMRG and TEBD are very similar and could calculate the same things. Today they are the most powerful methods for simulating 1-D strongly correlated quantum systems and are used by many research groups. The development of the algorithms continue and an exiting direction is to adapt them to quasi 2-D and 2-D systems.

In the first section we will discuss the physical foundation of these methods, the concept of entanglement. Then we discuss the main idea behind the ground state and time evolution calculations, focusing on the TEBD method. Finally we write the wave functions with MPS and explain why this is an efficient formulation for these methods.

3.3.1 Entanglement

To understand how much information is needed to describe a multi-particle quantum states, it is important to understand the concept of entanglement. Consider a quantum system with Hilbert space $\mathcal{H}$. Divide the system into two parts A and B, with Hilbert spaces whose product is the full Hilbert space

$$\mathcal{H} = \mathcal{H}_A \otimes \mathcal{H}_B. \tag{3.10}$$

The simplest non-trivial case is a system where both subsystems consists of 2 quantum states, for example $|\uparrow\rangle$ and $|\downarrow\rangle$. The wavefunction for the whole system H can be either a product state $|\psi\rangle = |\psi\rangle_A|\psi\rangle_B$ like,

$$\frac{|\uparrow\rangle_A + |\downarrow\rangle_A}{\sqrt{2}} \otimes |\uparrow\rangle_B, \tag{3.11}$$

or an entangled states $|\psi\rangle \neq |\psi\rangle_A|\psi\rangle_B$ like,

$$\frac{|\uparrow\rangle_A|\downarrow\rangle_B + |\downarrow\rangle_A|\uparrow\rangle_B}{\sqrt{2}}. \tag{3.12}$$

A product state is easy to describe since the state of one subsystem is independent of the other. However, for an the entangled state, a measurement on one subsystem will affect the other as well. For larger systems with N_A quantum states in the $\mathcal{H}_A$ subspace and N_B quantum states in the $\mathcal{H}_B$ subspace, it is important to be able to quantify the entanglement between them. The total wave function can be written in a more compact form if states $|\phi_\alpha\rangle_A$ and $|\phi_\alpha\rangle_B$ are used instead of the obvious ones $|i\rangle_A$ and $|i\rangle_B$ as

$$|\psi\rangle = \sum_{i=1}^{N_A}\sum_{j=1}^{N_B} C_{ij}|i\rangle_A|j\rangle_B = \sum_{\alpha=1}^{N=min(N_A,N_B)} \lambda_\alpha|\phi_\alpha\rangle_A|\phi_\alpha\rangle_B, \tag{3.13}$$

where C_{ij} and λ_α are constants. The states in the smallest subspace can be taken as the same $|\phi_\alpha\rangle_A \equiv |i\rangle_A$ and as an example for the larger subspace, consider our previous discussed system with 2 states $|\phi_\alpha\rangle_B = (C_{\alpha 1}|1\rangle_B + C_{\alpha 2}|2\rangle_B)/\lambda_\alpha$. For a normalized wave function $|\psi|^2 = 1$, the λ's satisfy $\lambda_\alpha \geq 0$ and $\sum_\alpha \lambda_\alpha^2 = 1$. The entanglement entropy S between the two subsystems (or the entanglement between subsystem A or B and the rest of the system, S_A or S_B) is

$$S = S_A = S_B = -\sum_\alpha \lambda_\alpha^2 log(\lambda_\alpha^2). \tag{3.14}$$

The quantum states $|\phi_\alpha\rangle_{(A,B)}$ are ordered in decreasing λ_α order such that $\lambda_1 \geq \lambda_2 \geq ... \geq \lambda_N$. The entanglement entropy for a product state is zero and small for a weakly entangled states $\lambda_1 \approx 1$. The maximal entanglement entropy $S_{max} = \log(N)$ is obtained for a maximal entangled state $\lambda_1 = \lambda_2 = ... = \lambda_N = 1/\sqrt{N}$. Most multi-particle quantum state are only slightly entangled and can be well described by a small subset of the basis states $|\phi_\alpha\rangle_{A,B}$

$$|\psi\rangle = \sum_{\alpha=1}^{N} \lambda_\alpha|\phi_\alpha\rangle_A|\phi_\alpha\rangle_B \approx \sum_{\alpha=1}^{\chi} \lambda_\alpha|\phi_\alpha\rangle_A|\phi_\alpha\rangle_B, \tag{3.15}$$

where $\chi \ll N$. As an example consider the entanglement spectra λ_α^2 at a split at a random bond for the ground state of the infinite spin-1 AFM Heisenberg chain, see Fig. 3.1. The two-fold symmetry in the spectra is due to symmetries present in this phase, see Ch. 7 for more information, and not something that always occurs. The rapid decrease in λ_α^2 is common for quantum states away from criticality. At or close to criticality a more involved approach is necessary, again see Ch. 7 for more details. As can be seen, the value falls off much faster than α, so almost all the information of this multi-particle quantum state with an infinite Hilbert space is contained in the first ~ 30 quantum states on each side.

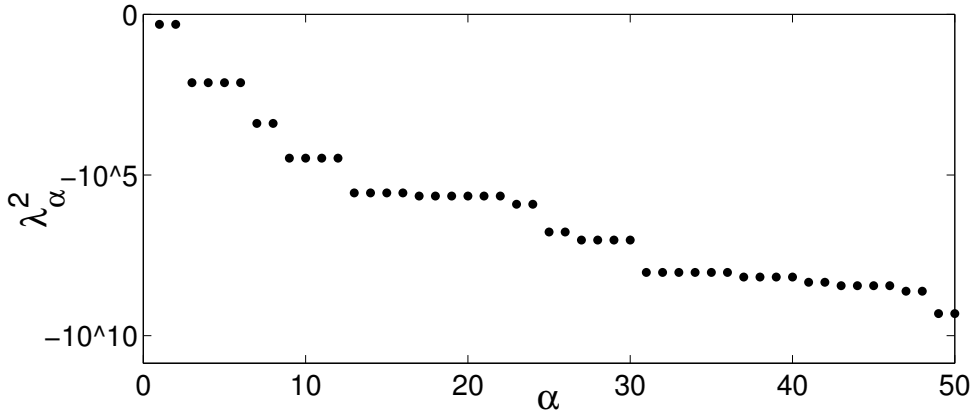

Figure 3.1: The entanglement spectra for a infinite spin-1 AFM Heisenberg chain.

To summarize, away from criticality a huge reduction in the amount of information needed to describe a multi-particle quantum state is possible, with $\chi \ll min(N_A, N_B)$. However, in this section we have only shown that this is possible when the full wave function $|\psi\rangle$ is known. In the following sections we discuss how to approximate $|\psi\rangle$ with a wavefunction $|\tilde{\psi}\rangle$ that never has more than χ basis states. We drop the tilde immediately and all wave functions below are built up from χ basis states.

3.3.2 Time Evolving Block Decimation

Before describing in details how a MPS description of a wave function can be obtained, let us go through the main idea about the operations we perform on these wave function to get the desired results. DMRG is normally slightly more efficient when calculating ground states while TEBD is more efficient at dynamics. Several great reviews has been written about the methods, see for example Ref. [33]. Instead of repeating everything here for both methods, we will briefly sketch one of the methods, TEBD where both ground state calculations and dynamics can be described at the same time. Given an initial quantum state $|\psi(0)\rangle$ it evolves into a state

$$|\psi(t)\rangle = e^{-iHt}|\psi(0)\rangle \tag{3.16}$$

after a time t, if the Hamiltonian is independent of time. The ground state of a Hamiltonian $|\psi_0\rangle$ can be obtained starting from a random initial state $|\psi_i\rangle$, with nonzero overlap with the ground state $\langle\psi_0|\psi_i\rangle \neq 0$, by time evolution in imaginary time

$$|\psi_0\rangle = \lim_{\tau\to\infty} \frac{e^{-H\tau}|\psi_i\rangle}{||e^{-H\tau}|\psi_i\rangle||}. \tag{3.17}$$

A Hamiltonian with only local interactions, for example only nearest neighbor interactions $H = \sum_r h^{[r,r+1]}$, is decomposed into parts that commutes with themselves

$$H = F + G = \sum_{even\ r} h^{[r,r+1]} + \sum_{odd\ r} h^{[r,r+1]}, \tag{3.18}$$

where $[h^{[r,r+1]}, h^{[r',r'+1]}] = 0$ if $|r - r'| \neq 1$. The real or imaginary time evolution operator can then be approximated with a Suzuki-Trotter decomposition of order p

$$e^{-i(F+G)\delta t} \approx f_p(e^{-iF\delta t}, e^{-iG\delta t}), \tag{3.19}$$

with $f_1(x, y) = xy$, $f_2(x, y) = x^{1/2}yx^{1/2}$, etc. This approximation gets better the larger p is and the smaller the time interval δt is. For the real dynamics we present in Ch. 6, we found it more advantageous from a computational point of view to decrease δt while keeping p low (we used $p = 2$). Every time we act with the time evolution operator on our state, the state grows and we need to truncate it. To be able to explain this, we need to describe in detail how quantum states are stored.

3.3.3 Matrix product states

Let us go back and discuss in more detail how the MPS description of a quantum state can be obtained [33, 34]. The wave function of a discrete chain with d quantum states on each of the L sites can be written as

$$|\psi\rangle = \sum_{j_1,\ldots,j_L}^{d} C_{j_1,\ldots,j_L}|j_1\rangle\ldots|j_L\rangle \approx \sum_{j_1,\ldots,j_L}^{d} B^T A_{j_1}\ldots A_{j_L}B|j_1,\ldots,j_L\rangle, \tag{3.20}$$

where A_{j_n} are $\chi \times \chi$ matrices (for $j_n = 1, ..., d$), and $|j_n\rangle$ represents the local state at site n. The $\chi \times 1$ vector B determines the boundary conditions. In this dissertation we will consider the case of infinite chains and the boundary matrices can be ignored. For translational invariant infinite chains with nearest neighbor interaction only matrices at two neighboring sites need to be stored $A_{j_{n+1}}$ and $A_{j_{n+2}}$. Note, that one site is not enough, since the operators F and G, from the previous subsection, act on two sites simultaneously. These $2d$ A-matrices are written as a product of $2d$ $\chi \times \chi$ complex matrices $\Gamma^{A,B}_{j,\alpha\beta}$ and 2 positive, real, diagonal matrices $\Lambda^{A,B}_{\beta}$, see Fig. 3.2 for a diagrammatic representation. In the figure is also shown how repeated use of a unitary operator like time-evolution can act on the state in a computational efficient way.

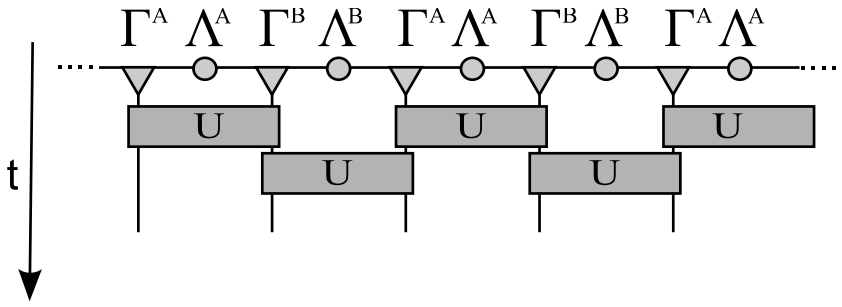

Figure 3.2: Top; diagrammatic representation of an iMPS formed by the tensors Γ and Λ. The horizontal line represents the bond indexes $\alpha_{A,B} = 1, \ldots, \chi$ and the vertical lines the physical indexes $D_{A,B} = 1, \ldots, d$. Unitary operators acts on the physical indexes. Only operators that commutes with each other acts simultaneously as described in the previous section. Repeated use according to a Suzuki-Trotter decomposition leads to a real (or imaginary) time evolution for a time t (τ).

We are now ready to explain how the time evolution operator acts on the wave function and what is done to prevent the amount of information from growing. The main idea is presented schematically in Fig. 3.3. In the first step $(i) \rightarrow (ii)$, F (or G) acts on $\Lambda^B_\alpha \Gamma^A_{j,\alpha\beta} \Lambda^A_\beta \Gamma^B_{j,\beta\alpha'} \Lambda^B_{\alpha'}$ (or $\Lambda^A_\alpha \Gamma^B_{j,\alpha\beta} \Lambda^B_\beta \Gamma^A_{j,\beta\alpha'} \Lambda^A_{\alpha'}$) to form the tensor $\Theta_{\alpha\alpha' jj'}$ with dimensions (χ, χ, d, d). This is rewritten as a $(\chi d, \chi d)$-matrix $\tilde{\Theta}_{(\alpha j),(\alpha' j')}$. Singular value decomposition (SVD) is performed on this matrix ($(ii) \rightarrow (iii)$). The middle diagonal matrix becomes the new Λ^A_β-matrix (or Λ^B_β). Its elements are ordered in descending order and only the χ largest of its χd elements are kept. The corresponding columns of X and rows of Y are also removed. The new Γ-matrices are obtained through division by the old Λ^B (or Λ^A), which is saved since this matrix is not updated in this sequence and the remaining χd index is split up in its χ and d part. This process is repeated with F and G the number of times the Suzuki-Trotter decomposition prescribes, see Eq. 3.19 for every time step δt.

In ground state simulations with imaginary time evolution, various conditions can be used to check when a good enough approximation to the ground state is obtained. One of the simplest, yet an efficient check is when the energy difference $\delta E(\tau) = E(\tau + \delta\tau) - E(\tau)$ between two time steps is smaller than some predetermined value $\delta E(\tau) \leq N_\tau$, which normally is $N_\tau \approx 10^{-8} - 10^{-12}$. A similar check could also be applied to the entanglement entropy $\delta S(\tau) = S(\tau + \delta\tau) - S(\tau) \leq N_S$. This normally converges a lot slower with common values $N_S \approx 10^{-4} - 10^{-6}$. To assure convergence in both quantities, multiple convergence criteria can be required for the simulation.

In real time evolution from a state that is not the ground state (the ground state is invariant under time evolution), the entanglement entropy normally increases rapidly with t, making it increasingly hard to store all the information needed to accurately describe the quantum state. The time evolution we perform in Ch. 6 starts out from a local quench on

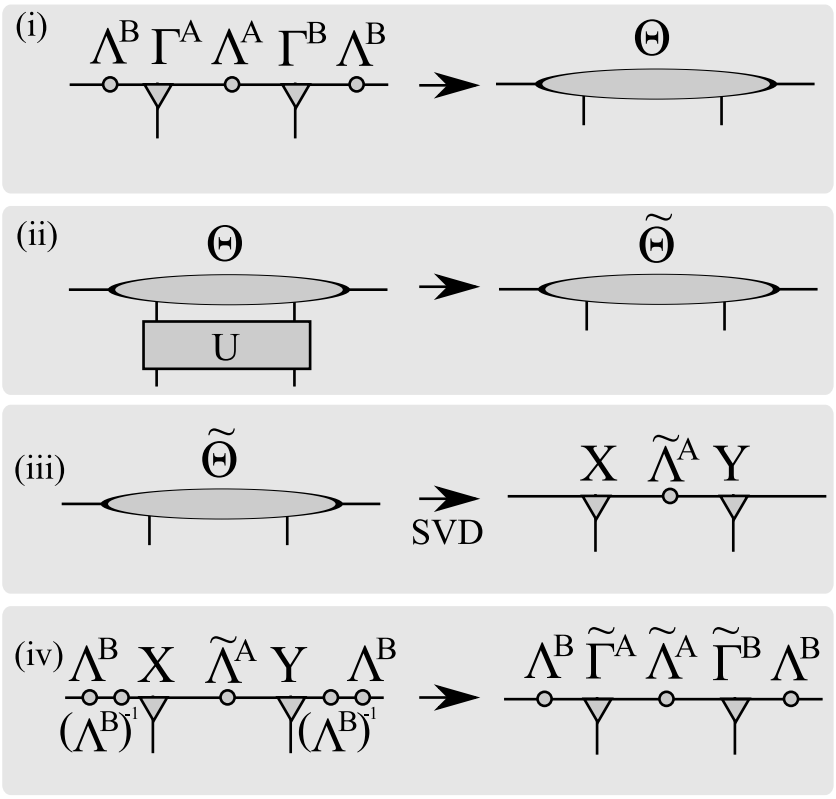

Figure 3.3: Update scheme for unitary two-site transformations of an MPS in the canonical form (see text for details).

the ground state $S_n^y|\psi_o\rangle$. The entanglement increase from this spreads out with constant velocity as can be seen in Fig.3.4. After the initial increase at a given site, the entanglement remains fairly constant.

Bonds with larger entanglement entropy, needs a larger χ on it to describe it accurately. However, the main increase in information that needs to be stored comes from all the additional Λ's (and Δ's), since the quench brakes the translational symmetry previously present in $|\psi_0\rangle$. More sites need to be added the longer one wants to time evolve the system. A slightly more advanced algorithm will add sites as the entanglement starts to increase on nearby sites.

The velocity with which the entanglement increase moves out from the local quench increases the closer to a critical point the initial ground state is. Since ground states already are more entangled close to criticality, it is very hard to do dynamics close to critical points.

To be able to evolve all these matrices long enough, a lot of computations need to be done. To make it manageable, we do not require the same precision as we normally do for ground state calculations and χ is decreased as much as possible. However, to avoid any artifacts to appear in our wave functions we need to be very careful. A good approach is

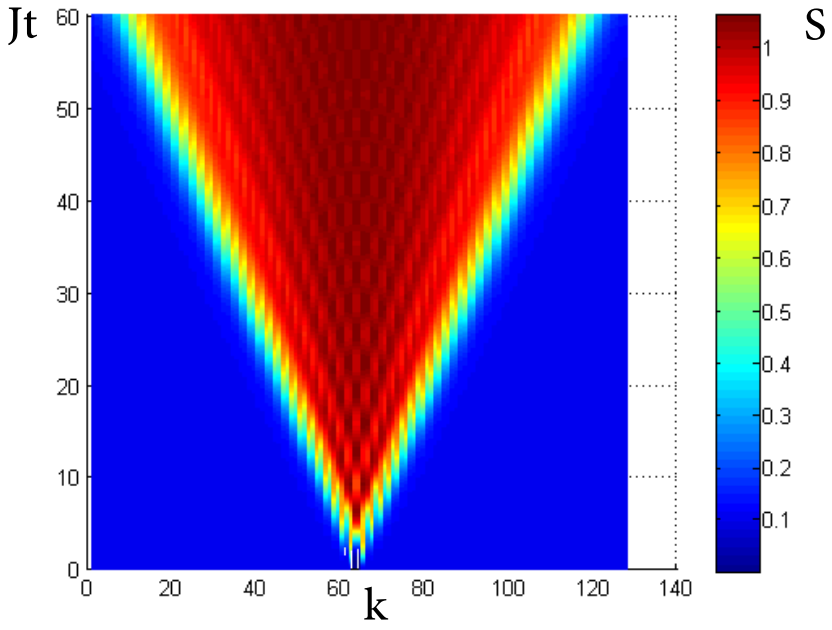

Figure 3.4: (Figure layout to be updated) Entanglment (color coded) after a local perturbation on site $k = 64$ as a function of bond the cut is made at (x-axis) and time (y-axis) in Jt.

to do simulations with various values for the parameters χ, δt and t_{final} and see when they start to differ more than desired. As an example, see Fig. 3.5, that shows the correlation function simulated for different χ

$$C(0,t) = \langle \psi_0 | S_n^-(t) S_n^+(0) | \psi_0 \rangle \tag{3.21}$$

simulated for different χ as a function of time t on the site where the local quench were performed at $t = 0$.

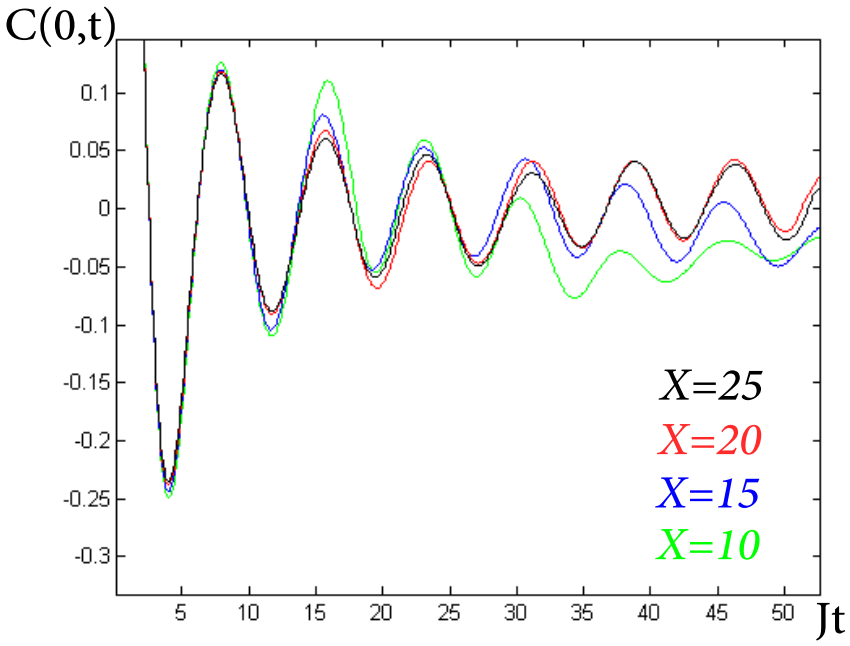

Figure 3.5: (Figure layout to be updated) Time evolution of the correlation function as a function of Jt for $\chi = 10$(green), $\chi = 15$(blue), $\chi = 20$(red) and $\chi = 25$(black) on the site the spin was flipped on at $t = 0$.

Part III

Magnetism in Ultracold Gases

Chapter 4

Magnetic phase diagram of a 2D S=1 condensate

4.1 Introduction

Bose condensates of atoms with nonzero total spin $F \geq 1$ show various phases combining magnetic and superfluid order. When the magnetic symmetry is broken spontaneously, as can occur when the atoms are confined in a spin-independent optical trap, condensates are classified as "polar" (for antiferromagnetic interactions) or "ferromagnetic". Most theoretical studies of these spinor Bose condensates neglect the long-range interaction between atomic magnetic moments, and this neglect is justified for many experimental conditions. However, recent experiments [35–37] investigating ordering in a nearly two-dimensional condensate have shown complex magnetic behavior in the ferromagnetically interacting $F = 1$ spinor Bose gas of ^{87}Rb.

The most surprising feature of these experiments, which image the spin distribution in real space, is a long-lived phase that appears to have the broken global $U(1)$ invariance of a superfluid along with possible breaking of the continuous translational symmetry in one or two directions, i.e., with stripe-like or checkerboard-like order. A possible supersolid phase has recently also been suggested in the superfluid of ^{4}He. [38] Many theoretical papers have been written about the properties of ^{4}He and whether a supersolid phase can exist in the absence of disorder. Only recently have theoretical studies been done to explain the observed supersolid-like behavior in a ^{87}Rb spinor condensate. [39] The earlier studies of ^{87}Rb concentrated on magnetic properties arising from the weak spin-dependent local interaction and the quadratic Zeeman shift. More recent experiments [36, 37] indicates that the long range dipole interaction also plays an important role in the formation of the magnetic phases in spatially large systems and with this addition a supersolid state might be possible.

Most previous studies of this system concern dynamical properties: the leading instability when the Hamiltonian is changed to favor ferromagnetic order can be stripe-like or

checkerboard-like depending on parameters. [39–41] In this chapter, our goal is to determine the static ground-state phase diagram. We start from the phases that are well established at low temperatures [42–45] for a spin-1 gas with no dipole interaction and quadratic Zeeman effect. (Low temperatures mean below the superfluid and magnetic transitions, where all the studies in this chapter will take place.) We then add the dipole interaction to see how it changes the phases as well as the location of the boundary between them. We do this in a quasi-two-dimensional geometry as in the experiments. [35–37] We investigate both an infinite and a finite square planar geometry. After observing the formation of two kinds of stripe order in a Monte Carlo simulation, we developed an analytical approach to explain the results, based upon smallness of the dipolar coupling at short distances. That analytical approach is presented first in order to prepare the groundwork for the simulation results.

We show that all boundaries in the phase diagram, except between the two polar phases, are moved when the dipole interaction is added, some in a non-intuitive way. The magnetic dipole interaction prefers a ferromagnetic state, but the confinement makes a ferromagnetic state out of the plane energetically unfavorable. Moreover, the spin precession make the in-plane perpendicular ferromagnetic state unfavorable, since the spin rotates out of the plane. Both ferromagnetic phases can get modulated in one direction. The phase parallel to the external fields needs a strong dipole interaction or a system much wider than its length to become modulated. This modulation appears as fully magnetized stripes with sharp domain walls between them. The phase perpendicular to the external fields gets modulated, from the very lowest dipole strengths, into a helical configuration around the field. The wavelength of the helix is inversely proportional to the dipole strength. For ^{87}Rb the wavelength is $\sim 80\mu$m and should be observable in experiments.

The outline of this chapter is as follows. In the following section, we review the basic physics of spinor condensates without the dipole interaction. In Sec. 4.3 we introduce the dipole interaction and put it into a form that is convenient for numerical simulations. Sec. 4.4 presents analytical results in the limit of weak dipole interaction, and Sec. 4.5 contains the results of our Monte Carlo simulations of the problem. The final section summarizes the relationship between our results and those of other theoretical papers and suggests how future experiments could be designed to observe clearly the metastable supersolid phase found in our simulations.

4.2 Review of spinor condensate without magnetic dipole interaction

Well below the Bose-Einstein condensation (BEC) temperature most bosons occupy the same quantum state. We write the total wavefunction as a product of single particle wavefunctions

$$\Psi_N(\mathbf{x}_1, \mathbf{x}_2, ..., \mathbf{x}_N) = \Psi(\mathbf{x}_1)\Psi(\mathbf{x}_2)...\Psi(\mathbf{x}_N), \tag{4.1}$$

where $\vec{r}_n$ is the coordinate of the n^{th} boson. A good approximation for the interactions between the bosons in a dilute gas is a spherical scattering potential. The Hamiltonian for a BEC with only this type of interaction between the bosons without and external field is

$$H = \sum_{i=1}^{N} \left(-\frac{\hbar^2}{2m}\nabla_i^2 + V(\mathbf{x}_i) + \sum_{i<j}\sum_{F=0}^{2f} g_F \mathcal{P}_F \delta(\mathbf{x}_i - \mathbf{x}_j) \right), \tag{4.2}$$

where f is the spin of the bosons (integer), g_f is a constant, and $\mathcal{P}_F$ a projector that projects the total spin onto a state with spin-F. The total wavefunction in two particle scattering must have an even integer combined spin $F = 0, 2, ...$, which gives a symmetric spin wavefunction, since the total wavefunction for bosons has to be symmetric and the spatial part is symmetric. Isolating the single-particle part of the Hamiltonian and integrating out $\int dV|\Psi| = N$ leads to the Gross-Pitaevski equation

$$\left(-\frac{\hbar^2}{2m}\nabla^2 + V(\mathbf{x}) + \sum_{F=0}^{2f} g_F \mathcal{P}_F)|\Psi(\mathbf{x})|^2 \right) \Psi(\mathbf{x}) = \mu\Psi(\mathbf{x}). \tag{4.3}$$

This is a single particle description of the condensate normalized to give the correct particle number, so we can use a simpler single particle Hamiltonian. A single particle Hamiltonian is also much easier to analyze numerical and we will use the classical Monte Carlo technique described in Ch. **??**. Before writing down the Hamiltonian we will work with, let us determine the precise form of the interaction. Alkali atoms that have a $I = 3/2$ nuclear spin, like ^{87}Rb, have a total spin $f = 1$ in the ground state per atom, since $\vec{F} = \vec{I} + \vec{S}$ with one electron in the outer shell $s = 1/2$. For $f = 1$ the projectos are $g_0\mathcal{P}_0 + g_2\mathcal{P}_2 = c_0 + c_2\vec{F}_1 \cdot \vec{F}_2$ [42]. A Bose-Einstein condensate of spin $f = 1$ atoms is described by a three-component complex order parameter

$$\Psi(\mathbf{x}) = \sqrt{n_{3D}(\mathbf{x})}\psi(\mathbf{x}) = \sqrt{n_{3D}(\mathbf{x})} \begin{pmatrix} \psi_{+1}(\mathbf{x}) \\ \psi_0(\mathbf{x}) \\ \psi_{-1}(\mathbf{x}) \end{pmatrix}, \tag{4.4}$$

where the spinor $\psi(\mathbf{x})$ is normalized as $\psi^\dagger\psi = 1$ and the subscripts label the spin eigenvalue with respect to an arbitrarily chosen quantization direction. In the absence of external fields and neglecting the dipole interaction, the Hamiltonian governing the condensate is[42, 43]

$$H_0 = \int d^3x \left[\frac{\hbar^2}{2m} |\nabla\Psi|^2 + \frac{c_0}{2} n_{3D}^2 + \frac{c_2}{2} n_{3D}^2 M^2 \right], \tag{4.5}$$

where m is the atomic mass, $\mathbf{M}(\mathbf{x}) = \psi^\dagger(\mathbf{x})\mathbf{F}\psi(\mathbf{x})$ is the dimensionless magnetization ($|\mathbf{M}| \leq 1$), and $\{F^i\}$ are the three generators of $SU(2)$ in the spin-1 representation

$$F^x = \frac{1}{\sqrt{2}}\begin{pmatrix} 0 & 1 & 0 \\ 1 & 0 & 1 \\ 0 & 1 & 0 \end{pmatrix}, \quad F^y = \frac{1}{\sqrt{2}}\begin{pmatrix} 0 & -i & 0 \\ i & 0 & -i \\ 0 & i & 0 \end{pmatrix},$$
$$F^z = \begin{pmatrix} 1 & 0 & 0 \\ 0 & 0 & 0 \\ 0 & 0 & -1 \end{pmatrix}. \tag{4.6}$$

The first term in the Hamiltonian is the kinetic energy for bosons with mass m. The next two terms are the spin-independent and spin-dependent contact interactions, respectively. The coefficients are given by $c_0 = (4\pi\hbar^2/3m)(2a_2 + a_0)$ and $c_2 = (4\pi\hbar^2/3m)(a_2 - a_0)$, with $\{a_0, a_2\}$ the s-wave scattering lengths in the channel with total angular momentum $\{0, 2\}$.

When $c_2 < 0$ ("ferromagnetic") it is energetically favorable for this system to magnetize, $M \neq 0$, while $c_2 > 0$ favors a "polar" state with $M = 0$. The scattering lengths for ^{87}Rb are $a_0 = 101.8a_B$ and $a_2 = 100.4a_B$, [46] where a_B is the Bohr radius, so c_2 is negative and its condensate will be ferromagnetic in the absence of external fields (still neglecting the dipole interaction). However, the condensate of ^{23}Na will be in a polar state. [42]

The external fields normally applied to a spinor condensate consist of an optical trap and a uniform magnetic field described by the following addition to the Hamiltonian

$$H_{ef} = \int d^3x \left[U + q\psi^\dagger(\hat{\mathbf{B}} \cdot \mathbf{F})^2\psi\right] n_{3D}, \tag{4.7}$$

The trapping potential $U(\mathbf{x})$ confines the condensate spatially; for our purposes, its main effect will be to produce a quasi-two-dimensional geometry. The quadratic Zeeman shift q can be tuned independently of $\mathbf{B}$ with microwave radiation, $q = q^B + q^{EM}$. [47] We take the two sources as coaxial along $\hat{\mathbf{z}}$, so we can use Eq. (4.7). This is also the axis we quantize the spinor along. The magnetic field also creates a linear Zeeman term $\mathbf{B}\cdot\int d^3x\, n_{3D}\boldsymbol{\mu}$, that favors an uniformly magnetized condensate. However, experiments on ^{87}Rb have not observed any tendency toward such relaxation over the accessible time scales of several seconds, [47] making the longitudinal component of magnetization conserved. (This assumption does not apply in condensates of higher spin, such as chromium. [48]) Normally, this component is chosen to vanish initially and can hence be ignored for the purpose of energetics. However, the magnetic field also causes Larmor precession of the magnetization perpendicular to it. This is an important effect that needs to be taken into account as it modifies the nature of the magnetic interaction on time scales longer than the precession time.

The spin state of the condensate is governed by the parameters c_2 and q, as in Fig. 4.2. [49] There are two different kinds of polar states ($c_2 > 0$), one that minimizes $\langle(F^z)^2\rangle = 0$ and one that maximizes $\langle(F^z)^2\rangle = 1$ the impact of the quadratic Zeeman term. Respectively,

$$\psi_\parallel^P(\phi) = e^{i\phi}\begin{pmatrix} 0 \\ 1 \\ 0 \end{pmatrix}, \quad \psi_\perp^P(\phi,\theta) = \frac{e^{i\phi}}{\sqrt{2}}\begin{pmatrix} -e^{-i\theta} \\ 0 \\ e^{i\theta} \end{pmatrix}. \tag{4.8}$$

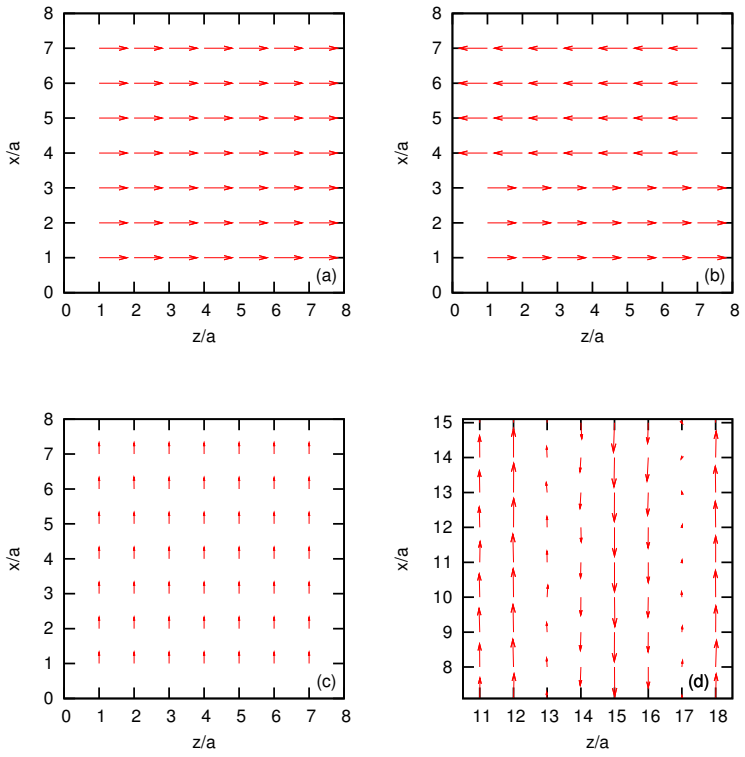

Figure 4.1: (Color online) Examples of possible spin configurations in the plane. The external fields are along the horizontal axis, $M_z(x,z)$ is plotted on the horizontal axis, $M_x(x,z)$ is on the vertical for every plaquette and $M_y(x,z)$ is not shown. (a) Uniform fully magnetized $F_\parallel$, (b) striped fully magnetized $F_\parallel$, (c) uniform partly magnetized $F_\perp/P_\parallel$ state, (d) helical fully magnetized $F_\perp$.

Consequently, does the phase $P_\parallel$, with order-parameter manifold $U(1)$, appears at $q > 0$, while the phase $P_\perp$ appears when $q < 0$. Note that the range of θ is only $[0,\pi)$, or alternatively that the order-parameter manifold for this phase is $U(1)\times U(1)/Z_2$. [50] When $c_2 < 0$ and $q < 0$, both energies are minimized by ferromagnetic states

$$\psi^F_{\parallel,\uparrow}(\phi) = e^{i\phi}\begin{pmatrix}1\\0\\0\end{pmatrix}, \quad \psi^F_{\parallel,\downarrow}(\phi) = e^{i\phi}\begin{pmatrix}0\\0\\1\end{pmatrix}, \tag{4.9}$$

giving a manifold $U(1)\times Z_2$ (recall that we exclude the linear Zeeman energy from energetic considerations), see Fig. 4.1. In the final quadrant of the phase diagram, however, no ferromagnetic state minimizes the quadratic Zeeman energy. The smallest impact of a

ferromagnetic state on the quadratic Zeeman term is $\langle (F^z)^2 \rangle = 1/2$ for

$$\psi_\perp^F(\phi, \xi) = \frac{e^{i\phi}}{2} \begin{pmatrix} e^{-i\xi} \\ \sqrt{2} \\ e^{i\xi} \end{pmatrix}, \tag{4.10}$$

Consequently, for $q < q_c = 2|c_2|n_{3D}$ the state will be a linear combination of $\psi_\parallel^P$ and $\psi_\perp^F$ with magnetization $M_x + iM_y = \sqrt{1-(q/q_c)^2}\, e^{i\xi}$ and manifold $U(1) \times U(1)$, see Fig. 4.1. Above q_c, the state will be the pure polar state $P_\parallel$.

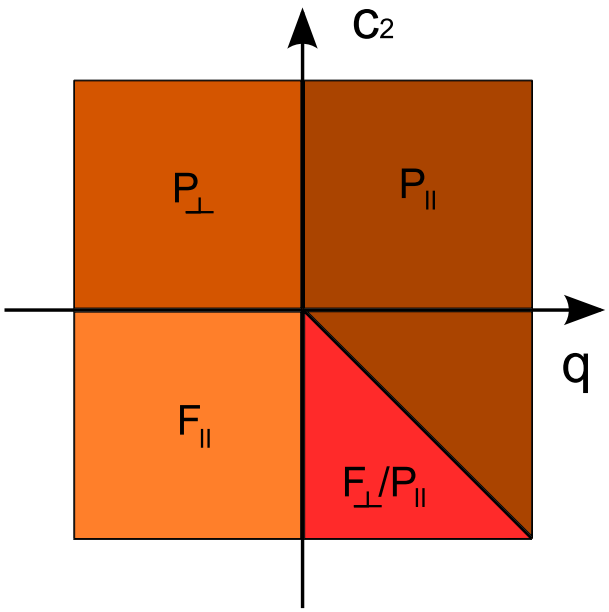

Figure 4.2: (Color online) Ground state phase diagram of a spin-1 condensate without dipolar interaction; from Mukerjee *et al.*. [49]

Typical experimental values for ^{87}Rb [35–37] include a peak density of $n_0 = 2.5 \times 10^{14}\,\mathrm{cm}^{-3}$, giving the interaction strengths $c_0 n_0 = 1.9\,\mathrm{kHz}$ and $c_2 n_0 = -9\,\mathrm{Hz}$, while $q^B \approx 1.6\mathrm{Hz}$ and q^{EM} can be tuned from roughly $-50\,\mathrm{Hz}$ to $50\,\mathrm{Hz}$ and is normally taken coaxial to q^B. [47]

4.2.1 Confinement

The optical trap in the experiment makes the gas effectively two dimensional, with a Thomas-Fermi radius $r_{TF} \approx 1.5\mu m$ along the direction of tightest confinement. [35–37] Since this is smaller than the spin healing length $\xi = \sqrt{\hbar^2/(2m|c_2|n_{3D})} \approx 2.5\mu m$, we take the confinement to be along the $\hat{y}$ direction and treat the gas as frozen along this direction;

that is, we take

$$\Psi(\mathbf{x}) = \sqrt{n_{2D}(x,z)\rho(y)}\,\psi(x,z), \tag{4.11}$$

where we assume $\int dy\,\rho(y) = 1$. In the following we will consider one of two profiles $\rho(y)$ as convenient, a boxcar profile and a Gaussian,

$$\rho_1(y) = \frac{1}{K}\Theta(K/2-y)\Theta(K/2+y),\ \rho_2(y) = \frac{1}{\sigma_y}\sqrt{\frac{2}{\pi}}e^{-\frac{2y^2}{\sigma_y^2}}, \tag{4.12}$$

where $\Theta(x)$ is the Heaviside step function. We introduce a common notation for the condensate thickness T and a 3-dimensional density $\bar{n}_{3D}(x,z)$ without y-dependence

$$\frac{1}{T} = \langle\rho\rangle = \int dy\,\rho(y)^2, \quad \bar{n}_{3D}(x,z) = \frac{n_{2D}(x,z)}{T} \tag{4.13}$$

for the boxcar profile and for the gaussian profile, to be able to treat both profiles simultaneously in section 4.4. In most of our analysis these densities are also independent of (x,z), except where we use a nonzero trapping potential $U(x,z)$ in the plane.

4.2.2 Precession

Atoms with magnetic moment $\boldsymbol{\mu}_\perp = g_F\mu_B\mathbf{M}_\perp$ perpendicular to the field precess at frequency $|\gamma|B_0 = |g_F|\mu_B B_0$ around the fields. As usual, μ_B is the Bohr magneton and g_F is Lande's g-factor. For ^{87}Rb, $g_F = -1/2$ and a field of $B_0 = 150\,\mathrm{mG}$ produces a Larmor precession at 110 kHz, a scale orders of magnitude larger than the contact interactions or the quadratic Zeeman energy.

The Hamiltonian considered so far is invariant under the spin rotation

$$\psi_k(x,z) \to U_{kl}(t)\psi_l(x,z), \quad U(t) = e^{-i\gamma B_0\hat{\mathbf{B}}\cdot\mathbf{F}t} \tag{4.14}$$

and is hence unaffected by the rapid Larmor precession. Therefore, adding precession does not affect the phase diagram in the problem with only local interactions. [42, 43] However when we include the dipole interaction in the next section, both confinement and spin precession become important.

4.3 Magnetic dipole interaction

The interactions considered thus far for a spin-1 condensate are all local. However, the moments $\boldsymbol{\mu}$ will interact through the long-ranged dipole interaction. The dipolar energy of a magnetized fluid with magnetization $\boldsymbol{\mathcal{M}}(\mathbf{x})$ is

$$E_{dip} = \frac{\mu_0}{8\pi}\int d\mathbf{x}d\mathbf{x}'\left[\frac{\boldsymbol{\mathcal{M}}\cdot\boldsymbol{\mathcal{M}}' - 3(\boldsymbol{\mathcal{M}}\cdot\hat{\mathbf{r}})(\boldsymbol{\mathcal{M}}'\cdot\hat{\mathbf{r}})}{r^3} - \frac{8\pi}{3}\mathcal{M}^2\delta^{(3)}(\mathbf{r})\right], \tag{4.15}$$

where $\mathbf{r} = \mathbf{x} - \mathbf{x}'$ and $\boldsymbol{\mathcal{M}}' = \boldsymbol{\mathcal{M}}(\mathbf{x}')$. The last term, or "s-wave" part, contributes to the contact interaction c_2 in the BEC Hamiltonian, and so should not be treated independently. In this chapter we take the first, "d-wave" part to be the full dipolar interaction. This is weak for ^{87}Rb relative to most other energies in the system, but since it is long ranged it will have an important impact on the magnetic phases. The initial studies of the spin-1 condensate ignored this term, [42, 49] but some recent works have included it along with the effects of quasi-two-dimensional confinement and rapid Larmor precession. [39, 40] Among other results, it was shown that dipolar interaction renders the Larmor precession unstable, [40] and we return to this point in the concluding section. Until then we follow previous authors and assume that this instability has significant effects only at late times, and so neglect it. Cherng and Demler examined the instability spectrum of a uniform ferromagnetic state within a mean field and collective mode analysis. We will use the same physical model but instead look at the ground state phase diagram and consider a wider range of parameters c_2, q, and c_d (see Eq. (4.16) below) with analytical and Monte Carlo calculations.

The total Hamiltonian we work with is

$$H = H_0 + H_{ef} + H_{dip} \tag{4.16}$$

where

$$H_{dip} = \frac{c_d}{2}\int d^3x d^3x' n_{3D}(\mathbf{x}) M_i(\mathbf{x}) n_{3D}(\mathbf{x}') M_j(\mathbf{x}') \left[\nabla_i \nabla'_j \frac{1}{|\mathbf{x}-\mathbf{x}'|} - \frac{4\pi}{3}\delta_{ij}\delta^{(3)}(\mathbf{x}-\mathbf{x}')\right]. \tag{4.17}$$

This is the same as the more usual expression with $(\delta_{ij} - 3\hat{r}_i\hat{r}_j)/r^3$, but split it into a part that is positive-(semi-)definite and a part that simply shifts the parameter $c_2 \to c_2 - 4\pi c_d/3$. This decomposition is convenient for numerical work that searches for energy minima. With two integrations by parts the first term becomes the Coulomb interaction for a charge density $\boldsymbol{\nabla}\cdot(n_{3D}\mathbf{M})$. We will typically mean just this term when referring to "the dipole interaction," since it is the difficult part.

For both analytical and numerical work we need the dimensionally reduced form of the Coulomb part expressed in a rotating frame. Ignoring the contact term in H_{dip} and performing two partial integrations we find

$$E^C_{dip} = \frac{c_d}{2}\int d^3x d^3x' \frac{\boldsymbol{\nabla}\cdot(n_{3D}\boldsymbol{M}(\mathbf{x}))\boldsymbol{\nabla}'\cdot(n_{3D}\boldsymbol{M}(\mathbf{x}'))}{|\mathbf{x}-\mathbf{x}'|} = \frac{c_d}{2}\int d^2x d^2x' \sigma(x,z)\sigma'(x',z')\cdot$$
$$\int dy dy' \frac{\rho(y)\rho(y')}{|\mathbf{x}-\mathbf{x}'|} + \frac{c_d}{2}\int d^2x d^2x' n_{2D} M_y(x,z) n_{2D} M_y(x',z') \int dy dy' \frac{[\partial_y \rho(y)][\partial_{y'}\rho(y')]}{|\mathbf{x}-\mathbf{x}'|} \tag{4.18}$$

where $\sigma(x,z) \equiv \partial_x(n_{2D}M_x(x,z)) + \partial_z(n_{2D}M_z(x,z))$ is an effective surface charge density. The density n_{2D} has only a (x,z) dependence for a nonzero trapping potential $U(x,z)$. The integrals over y can be performed explicitly for either Gaussian or boxcar profiles ρ; we

choose the Gaussian form for the purposes of numerics. Then

$$\rho(y)\rho(y') = \frac{2}{\pi\sigma_y^2} e^{-(y_+^2+y_-^2)/\sigma_y^2}$$
$$[\partial_y\rho(y)][\partial_{y'}\rho(y')] = \frac{8(y_+^2-y_-^2)}{\pi\sigma_y^6} e^{-(y_+^2+y_-^2)/\sigma_y^2} \tag{4.19}$$

with $y_\pm = y \pm y'$. The integrals over y_+ are simple, and the integrals over y_- can be put in terms of special functions with help of the identities $\int dx \frac{e^{-x^2}}{\sqrt{c^2+x^2}} = e^{\frac{c^2}{2}} K_0(\frac{c^2}{2})$ and $\int dx \frac{x^2 e^{-x^2}}{\sqrt{c^2+x^2}} = \frac{\sqrt{\pi}}{2} U(\frac{1}{2}, 0, c^2)$. Here K_0 is a modified Bessel function and U is a confluent hypergeometric function.

The strength of the dipole term is given by $c_d = \mu_0 g_F^2 \mu_B^2/4\pi$, where μ_0 is the vacuum permeability, giving a value of $c_d n_0 = 0.8\,\mathrm{Hz}$ for ^{87}Rb. The effect of confinement is less trivial for this term then for the others, and transforming to a rotating frame is also nontrivial since the interaction couples spin directions to spatial directions. See Appendix **??** for a full treatment of these effects. In the following section, we discuss how the dipole interaction is expected to modify the phase diagram when it is sufficiently weak that the $H_{dip} = 0$ ground states can be used as a starting point.

4.4 Analytical Results

Adding the dipole interaction Eq. (4.17) will change the phase diagram Fig. 4.2. The term that looks like the spin dependent interaction will just move the whole phasediagram up along c_2 with $\frac{4\pi c_d}{3}$. The energy from the Coulomb part of the dipole interaction is always positive, hence this parts prefers a polar state with zero magnetization $M = 0$. Consequently, regions of Fig. 4.2 with polar states above $c_2 = \frac{4\pi c_d}{3}$ will not change if we add the dipole-dipole coupling. However, the rest of the phase diagram may be affected and the phase boundaries will depend on c_d, as we now discuss in some detail.

4.4.1 Weak dipole interaction

Adding a weak dipole term (weak compared to the kinetic energy term) will only change the phase diagram slightly. We start out by ignoring any new phases and investigate how a weak dipole interaction will move the boundaries between the existing phases. The three magnetic terms in the Hamiltonian are the spin-dependent contact interaction, the quadratic Zeeman and the dipole term. By comparing the energy contributions from these three for simple *Ansätze* we can locate the boundaries between different minima, in a system with L the extent along z and W the extent along x.

The polar phases are, of course, the simplest (see Eq. (4.8))

$$E^{P_\parallel} = 0, \quad E^{P_\perp} = q\bar{n}_{3D} LWT. \tag{4.20}$$

Consider next the phase $F_\parallel$, which appeared at $q, c_2 < 0$ in the system without dipolar energy. The two terms previously treated are easily kept exact, while the dipole term requires more treatment.

For a uniform condensate with maximal magnetization, aligned parallel to the magnetic field, the only contribution to the dipole energy comes from the quasi 1-dimensional lines of charge of length W located at the edges at $z = \pm L/2$. The second term in Eq. (4.18) does not contribute and only the edges of the first

$$E^C_{dip} = \frac{c_d n_{2D}^2}{2} \int_{-W/2}^{W/2} dx dx' \int_{-\infty}^{\infty} dy dy' \rho(y)\rho(y') \times 2 \left[\frac{1}{\sqrt{x_-^2 + y_-^2}} - \frac{1}{\sqrt{x_-^2 + y_-^2 + L^2}} \right] \quad (4.21)$$

In the limit $L \gg W \gg T$, the leading contribution to the energy comes solely from the first term, which describes the self energy of two quasi-one-dimensional lines of charge. Indeed, it becomes just

$$\begin{aligned} E^C_{dip} &= 2c_d n_{2D}^2 \int^W dx_- (W - x_-)/x_- \\ &= 2c_d n_{2D}^2 W \ln W/T + O(W) \end{aligned} \quad (4.22)$$

asymptotically, where the lower cutoff T has been chosen for convenience.

The energy for the uniform out-of-plane configuration is

$$E^C_{dip} = \frac{c_d}{2} n_{2D}^2 \int d^3x d^3x' \frac{[\partial_y \rho(y)][\partial_{y'} \rho(y')]}{|\mathbf{x} - \mathbf{x}'|}. \quad (4.23)$$

Since there will be a term extensive in the planar size, it is simplest to ignore the effects of boundaries and work with a surface energy density

$$\begin{aligned} \eta &= \frac{c_d}{2} n_{2D}^2 2\pi \int dy dy' \int_0^R dr \, \frac{r \, [\partial_y \rho(y)][\partial_{y'} \rho(y')]}{\sqrt{r^2 + y_-^2}} \\ &= 2\pi c_d n_{2D}^2 \int dy dy' \rho(y)\rho(y')\delta(y - y') + O(1/R) \\ &= 2\pi c_d n_{2D}^2 \frac{1}{T} \end{aligned} \quad (4.24)$$

after integrating over the radial coordinate r followed by partial integration in y and y'.

Keeping terms of order A^2 and $A \ln A$ where $A = L, W$, (see Eq. (4.9))

$$E^{F_\parallel} = \frac{\tilde{c}_2}{2} \bar{n}_{3D}^2 LWT + q\bar{n}_{3D} LWT, + 2c_d \bar{n}_{3D}^2 WT^2 \ln W/T \quad (4.25)$$

with $\tilde{c}_2 = c_2 - 4\pi c_d/3$.

The transition in the left half-plane betwen the states $F_\parallel$ and $P_\perp$, see Fig. 4.3, will hence be moved up from $c_2 = 0$ for a system without dipole interaction to

$$c_{2c} \equiv 4c_d \left(\frac{\pi}{3} - \epsilon_L \right), \quad (4.26)$$

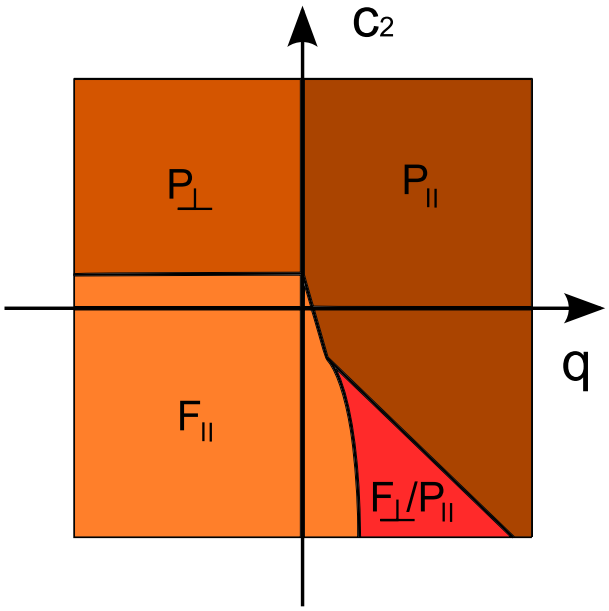

Figure 4.3: (Color online) Ground state phase diagram for a spin-1 condensate with dipole interaction and external fields, that introduces a quadratic Zeeman term and rapid spin precession. Both polar and ferromagnetic phases appear, perpendicular as well as parallel to the field.

where $\epsilon_L = \frac{\ln W/T}{L/T}$ will vanish in the large-system limit.

The region of the phase diagram with $q > 0$ and $c_2 < 0$, is the most interesting, due to the rapid precession of the perpendicular magnetization about the magnetic field, and the high dipolar energy cost of spins pointing out of the plane. Consequently, the region of $F_\perp/P_\parallel$ in the phase diagram will shrink and the regions of $P_\parallel$ and $F_\parallel$ grow, with the latter extending to positive values of q. For a uniform condensate with spins out of the plane, the Coulomb energy is equivalent to that of a parallel-plate capacitor, giving an energy $2\pi c_d(\bar{n}_3 M)^2 T^2 LW/T$ to leading order, *i.e.*, neglecting fringing fields, see Appendix **??**.

Because of the precession, the spins will effectively average the out-of-plane and in-plane interaction energies with equal weights. Consequently, the dipole energy for magnetization perpendicular to the external fields is $c_d(\bar{n}_3 M)^2(\pi W + T \ln L/T)LT$. To find the energy for the $F_\perp/P_\parallel$ state, we first have to find M, since this state is not completly magnetized. Consider a spinor $\psi^T = (a, b, a)$ with $a = \sqrt{(1-b^2)/2}$ $(1/\sqrt{2} < b < 1)$, which represents a superposition of $\psi_\parallel^P$ and $\psi_\perp^F$ (see Eqs. (4.8) and (4.10)). Its magnetization is $M_x = 2b\sqrt{1-b^2}$. Putting it all together,

$$E^{F_\perp/P_\parallel} = 4b^2(1-b^2)(\frac{\tilde{c}_2}{2}W + c_d(\pi W + T \ln W/T))\bar{n}_{3D}LT + q\bar{n}_{3D}(1-b^2)LWT. \quad (4.27)$$

The energy for this state is minimized at

$$b^2 = \frac{1}{2}\left(1 + \frac{q}{q_c}\right). \tag{4.28}$$

As the notation suggests, the transition between the phases $P_\parallel$ and $F_\perp/P_\parallel$ occurs at $q = q_c$, where $E^{F_\perp/P_\parallel} = E^{P_\parallel} = 0$ and $M = 0$

$$q_c \equiv 2|c_2|\bar{n}_{3D} - 4c_d\bar{n}_{3D}\left(\frac{\pi}{3} + \epsilon_W\right), \tag{4.29}$$

where $\epsilon_W = \frac{\ln L/T}{W/T}$ will vanish in the large system limit. As can be seen in Eqs. (4.28), (4.29) and (4.30), the value of the magnetization and hence the order parameter for the $F_\perp/P_\parallel$ state decreases continuously and is zero at the phase transition to the $P_\parallel$ state.

$$M_0 = |\langle F_\perp/P_\parallel\rangle| = \sqrt{1 - (q/q_c)^2} \tag{4.30}$$

This is exactly the same equation as for a system without dipole interaction, except that q_c now is given by Eq. (4.29).

Plugging the form for b, Eq. (4.28) and (4.29), back in also allow us to locate the transition between $F_\perp/P_\parallel$ and $F_\parallel$, where $E^{F_\perp/P_\parallel} = E^{F_\parallel}$, which will occur at

$$q_{c2} \equiv \sqrt{q_c\left(2|c_2|\bar{n}_{3D} + 8c_d\bar{n}_{3D}\left(\frac{\pi}{3} - 2\epsilon_L\right)\right)} - q_c. \tag{4.31}$$

Finally, the transition between $F_\parallel$ and $P_\parallel$ will take place when $E^{F_\parallel} = E^{P_\parallel} = 0$, at

$$q_{c3} \equiv \frac{|c_2|\bar{n}_{3D}}{2} + 2c_d\bar{n}_{3D}\left(\frac{\pi}{3} - \epsilon_L\right). \tag{4.32}$$

The three transition lines (q_c, q_{c2} and q_{c3}) separating the three phases in the lower right quadrant meet at the point

$$(q, c_2) = 4c_d\left(\bar{n}_{3D}\left(\frac{\pi}{3} + \epsilon_W - 2\epsilon_L\right), \left(\frac{\pi}{3} + 2\epsilon_W - \epsilon_L\right)\right). \tag{4.33}$$

To finish the phase diagram, we see that the transition line in Eq. (4.32), that separates $F_\parallel$ and $P_\parallel$, can be extended to the region $q, c_2 > 0$, with the substitution $|c_2| \to -c_2$ and that it will intersect with the transition line in Eq. (4.26) at the point $(q, c_2) = (0, c_{2c})$.

4.4.2 Magnetic plaquettes

The dipolar energy favors spatially modulated ferromagnetic states, which screen the long-ranged interaction, over uniform states. Consider the state $F_\parallel$. We can adapt a classic argument of Kittel concerning the formation of magnetic domains to the present quasi-two-dimensional geometry. [3] The boundary energy $2c_d\bar{n}_{3D}^2 WT^2 \ln W/T$ from before will

become $2c_d\bar{n}_{3D}^2 WT^2 \ln d/T$ if the uniform state breaks up into Ising-like domains of width d and length L that alternate between $M_z = 1$ and $M_z = -1$, keeping the total magnetization $M_0 = 1$ everywhere, see Fig. 4.1. There will be a cost in kinetic energy at the domain walls, and the competition between these two effects sets the domain size.

We can estimate an upper bound for the domain wall energy by assuming its width is the spin-healing length ξ_S. The energy will scale with the area of the wall $\sim LT$, and the surface density will be $\sigma_W \sim \hbar^2\bar{n}_{3D}/2m\xi_S$. With the number of domains given by W/d, the energy is

$$E = \sigma_W \frac{LWT}{d} + 2c_d\bar{n}_{3D}^2 WT^2 \ln d/T, \tag{4.34}$$

which gives

$$d^{\parallel} = \frac{\sigma_W}{c_d\bar{n}_{3D}^2 T} L. \tag{4.35}$$

The resulting domains have a width proportional to the length of the system, and are very large when the dipolar coupling is weak. In ^{87}Rb with the experimental parameters given in section 4.2.1, $\sigma_W \sim 10^4\,\mathrm{Hz}\,\mu\mathrm{m}^{-1}$ and $d^{\parallel} \sim 20L$, which could be difficult to achieve experimentally.

For a rectangular sample ($L > W$) in the $F_{\parallel}$ state, with a constraint of zero total longitudinal magnetization ($\int d\mathbf{x} n_{3D}(\mathbf{x}) M^z(\mathbf{x})) = 0$), it can be more energetically favorable to split up into two domains perpendicular to the field. The energy for this configuration is $E = 2\sigma_W WT + 3c_d\bar{n}_{3D}^2 WT^2 \ln W/T$ to leading order and if this is lower than the energy in Eq. (4.31) it will occur. However, this is only due to the constraint; a domain-free configuration has lower energy and a configuration with several domain walls perpendicular to the field will not be favorable for any values in the phase diagram.

4.4.3 Magnetic helix

For the $F_{\perp}$ state, a different modulation will appear. In particular, since the state is XY-like (the rapid Larmor precession gives the same energy for all perpendicular spin directions), it can adopt a smoothly varying magnetization texture. The smoothest form will be a helix, with wave vector along the magnetic field, see Fig. 4.1.

We can obtain a simple estimate of the wavelength of the transverse helical state to leading order in the strength of the dipole coupling by assuming a fully polarized time evolving state $\psi_{\perp}^F(0, k_z z - \gamma B_0 t)$, Eq. (4.10), with magnetization

$$M_x + iM_y = n_{2D}\rho(y)e^{i(k_z z - \gamma B_0 t)}. \tag{4.36}$$

Fourier transforming the kinetic and the dipole energy term, keeping only contributions that scale with the area of the two-dimensional system, the (areal) energy density of this state is

$$\frac{\text{energy}}{\text{area}} = n_{2D}\frac{\hbar^2}{2m}\frac{k_z^2}{2} + \frac{c_d}{2}\frac{n_{2D}^2}{2}\int \frac{dk_y}{2\pi}\frac{4\pi}{k_y^2 + k_z^2} k_y^2 |\tilde{\rho}(k_y)|^2 \tag{4.37}$$

plus k_z-independent terms. In the kinetic term, there is a factor of $1/2$ because only half the atoms are in the $m_z = \pm 1$ states that carry kinetic energy. In the dipole term, the only extensive contribution to the energy comes from the out-of-plane component M_y, which gives a factor $1/2$ there as well. Notice also that the time dependence is gone. With $k_y^2/(k_y^2+k_z^2) = 1 - k_z^2/(k_y^2+k_z^2)$, the relevant terms are

$$n_{2D}\frac{\hbar^2}{2m}\frac{k_z^2}{2} - \frac{c_d}{2}\frac{n_{2D}^2}{2}|k_z|\int\frac{du}{2\pi}\frac{4\pi}{1+u^2}|\tilde{\rho}(|k_z|u)|^2, \tag{4.38}$$

and to lowest order in k_z we just need $\tilde{\rho}(0) = \int dy\,\rho(y) = 1$ to arrive at

$$n_{2D}\frac{\hbar^2}{2m}\frac{k_z^2}{2} - \pi\frac{c_d}{2}n_{2D}^2|k_z|, \tag{4.39}$$

which takes its minimum at

$$k_z = \pm\frac{\pi}{2}\frac{n_{2D}c_d}{\hbar^2/2m}. \tag{4.40}$$

At leading order in the dipole strength, then,

$$\lambda_z^\perp \sim \frac{\hbar^2/2m}{c_d\bar{n}_{3D}T} \tag{4.41}$$

with $\lambda_z^\perp$ the wavelength of the helical modulation.

In other words, as shown in Fig. 4.4, the magnetization will adopt a configuration like $M_x(z) = \sin(k_z z)$ and $M_y(z) = \sin(k_z z + \frac{\pi}{2})$ at any instant of time. The kinetic energy of such a state goes as k_z^2, while the dipole energy turns out to decrease as k_z for small k_z.

In ^{87}Rb with experimentally accessibly densities the wavelength is approximately 80μm and should be observable. Note that the scales for the two textures are related by $d^\parallel \sim \lambda_z^\perp(L/\xi_S)$.

Since the modulations of $F_\parallel$ and $F_\perp$ decrease the total energy of those states, their regions of the phase diagram, Fig. 4.3, will be larger than predicted in the previous subsection. However, the dipole strength must be large to introduce domains into the $F_\parallel$ state; and the energy gain in a helical texture relative to a uniform $F_\perp$ is small; so the phase boundaries will not change significantly at weak or moderate dipole strengths when we take these textures into account.

4.5 Numerical Results

We investigate numerically the ground state phase diagram of a spin-1 condensate in external fields that give rise to a quadratic Zeeman shift and Larmor precession. The Metropolis algorithm [27], discussed in Ch. 3, allows us to efficiently locate minima of a given energy functional. We discretize the system on a lattice, and for the fundamental move we draw random deviations in the six real components of the field Ψ from a normal distribution at

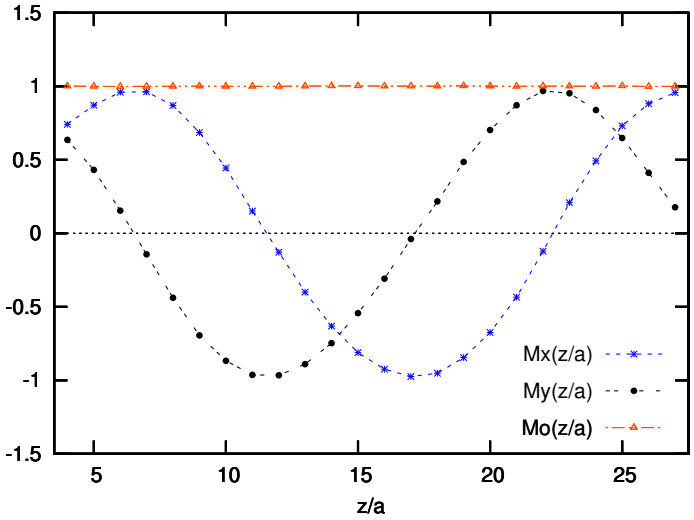

Figure 4.4: (Color online) Transverse magnetization as a function of z, from numerical simulation. Orange: magnitude of total magnetization M_0, blue: transverse magnetization in plane M_x and black: transverse magnetization out of plane M_y. A helical modulation with wavelength $\lambda \approx 85$ μm is clearly visible. Simulation values: $|\tilde{c}_2|\bar{n}_{3D} = 320$ Hz, $c_d\bar{n}_{3D} = 0.8$ Hz and $q = 100$ Hz (edges removed).

a lattice site. The initial state is similarly generated from random normally distributed variables.

A wide variety of simulation parameters (N, a, σ_y, T_{MC}, T^c_{MF}, μ, c_0, see below), for example $1 \times 1 < N < 50 \times 50$, have been used to investigate the phase diagram(c_2, q, c_d). Energies have been calculated in Hz and the lengths have been inserted in μm. Unless otherwise noted, numerical results presented here use lattice constant $a = 4\,\mu$m, thickness $\sigma_y = 2\,\mu$m, and a system size of $N = 30 \times 30$ plaquettes. We also add a chemical potential to the energy, $\mu = 1202\,\mathrm{Hz}\mu\mathrm{m}^{-2}$, in order to reproduce the experimental density for $c_0 = 1.9kHz$. Finally, we set $T_{MC} = 23\,\mathrm{nK}$ in the Metropolis weight $e^{-\langle H\rangle/kT_{MC}}$, which strikes a good balance between reducing fluctuations and achieving convergence in a reasonable computation time and use a critical mean field temperature $T^c_{MF} = 100T_{MC}$.

The phase diagram we have mapped out numerically agrees well with the results presented so far. In particular, we have confirmed that the ferromagnetic states develop modulations governed by the strength of the dipole interaction.

The algorithm described above tends to get trapped in local energy minima with varying densities of domain walls in the $F_\parallel$ region of the phase diagram. We can, however, locate the global minimum fairly confidently by starting the system in a variety of modulated states (striped or checkerboard) and comparing the final energies. The existence of metastable states as a consequence of dipolar interactions has been discussed before for spinor condensates in an optical lattice [51]. We have not observed any tendencies for the simulation in

the $F_\perp/P_\parallel$ region of the phase diagram to be trapped in a local energy minima, regardless of the initial configuration. This is as expected, since any possible local ground state configuration (Eq. (4.10)) can smoothly turn into another, unlike in the $F_\parallel$ case (Eq. (4.9)). This symmetry between the two transverse components of the magnetization is present in the Hamiltonian without the dipole interaction, removed by the dipole interaction, and finally restored by the rapid Larmor precession. However, even if the relaxational dynamics of the Metropolis algorithm used here does not apparently get trapped in a local minimum in this phase, the actual dynamics of the experimental system is primarily precessional rather than relaxational, which could lead to metastable states.

4.5.1 Numerical treatment of the dipole term

For the numerics, discretize the integrals in Eq. 4.18 as follows. Divide the 2-dimensional area into rectangular plaquettes and set the density n_{2D} and magnetization $\boldsymbol{M}$ constant on each plaquette,

$$\boldsymbol{M}(x,z) \to \boldsymbol{M}(a(r+\frac{1}{2}), a(s+\frac{1}{2})), \tag{4.42}$$

where a is the lattice constant and r, s are integers. Then do several variable substitutions. Going to variables $x_\pm$ and $z_\pm$ and scaling the coordinates by a allows us to replace

$$\int d^2x d^2x' \to \int_{p-1}^{p+1} dx_- \int_{q-1}^{q+1} dz_- (1-|x_- - p|)(1-|z_- - q|) \tag{4.43}$$

since the integrands depend only on x_-, z_-. Here $p = r' - r$ and $q = s' - s$.

The integrals can then be computed numerically for $0 \le p, q < \sqrt{N}$. The final step is to time-average the fields to take into account the rapid Larmor precession. This effectively means replacing

$$\begin{aligned} \sigma(p,q)\sigma(p',q') \to\ & \partial_z(n_{2D}M_z(p,q))\partial_{z'}(n_{2D}M_z(p',q')) \\ & + \frac{1}{2}\partial_x(n_{2D}M_x(p,q))\partial_{x'}(n_{2D}M_x(p',q')) \\ & + \frac{1}{2}\partial_x(n_{2D}M_y(p,q))\partial_{x'}(n_{2D}M_y(p',q')) \end{aligned} \tag{4.44}$$

and

$$M_y(p,q)M_y(p',q') \to \frac{1}{2}M_x(p,q)M_x(p',q') + \frac{1}{2}M_y(p,q)M_y(p',q') \tag{4.45}$$

in Eq. (4.18), since the transverse components rotate into each other but the longitudinal component is unaffected.

4.5.2 Domain walls in $F_\parallel$

Near the transition $q_{c2}(c_2, c_d)$, Eq. (4.31), magnetization vortices with unit spin winding develop all the way along all domain walls, see Fig. 4.5. The vortices are alternating elliptical and hyperbolic Mermin-Ho vortices, with ferromagnetic cores. [42, 52] The density of

vortices increases with increasing dipole interaction, i.e. more domain walls appear and the longitudinal length of each vortex decreases. The transverse length of the vortices increases with increasing quadratic Zeeman strength up to the transition line, which can be seen in the Fourier transform of the magnetization

$$M_z(k_x) = \sum_{r,s} e^{-irk_x} M_z(r,s), \tag{4.46}$$

as a rise in $M_y(k_z^{max})$; see Fig. 4.5 on the $F^{\parallel}$ side of the transition. The transition at q_{c2} itself remains sharp, and no vortices are observed for $q > q_{c2}$. At a given instant in time does the perpendicular magnetization in all vortices in a domain boundary point in a specific direction. The correlations between the direction of the transverse magnetization of vortices in different domain walls are however weaker.

4.5.3 Boundaries and trapping potential

Finite size effects and the details of the trapping potential seem to have little impact on our results. The only finite size effect observed with hard-wall boundaries is a decrease in magnetization at the $z = \pm L/2$ boundaries in the transition from $F_{\parallel}$ to $P_{\perp}$, as shown in Fig. 4.6. The approximative location of this transition line from the analytical calculation, Eq. (4.26), is $|\tilde{c}_{2c}|\bar{n}_{3D} = 3.4$Hz.

We have also carried out simulations with an elliptical trap potential of the form $U(\mathbf{x}) = U(v_z(\frac{z}{a})^2 + v_x(\frac{x}{a})^2)$, typically with $U = 625$ Hzμm^{-2} and $v_z, v_x = 1 - 10$ to more closely model experimental conditions. [35–37] These simulations have shown no effect other than a decrease in the density and thereby related effects, as in the original paper of Ho on spinor condensates in optical traps. [42] For example, the wavelength of the helical modulation in $F_{\perp}/P_{\parallel}$ is inversely proportional to the density, see Fig. 4.7 which shows a change in wavelength through the condensate as the density changes. In particular, we have not seen the effect reported by Vengalattore *et al.* [37] in which the modulation wave vector is not aligned with the applied magnetic field but is instead influenced by the orientation of the trap.

4.6 Discussion

We have mapped out the complete phase diagram for the model we have considered. Although the region occupied by the phase $F_{\perp}/P_{\parallel}$ moves and shrinks with the introduction of the dipole interaction, we find that it remains accessible at physical values of $|c_2|$ and c_d in ^{87}Rb, for some values of the quadratic Zeeman shift q. Hence, by tuning q for ^{87}Rb appropriately, the three phases $F_{\parallel}$, $F_{\perp}/P_{\parallel}$ and $P_{\parallel}$ should be observable in experiments. We also find that a spatial modulations should be seen in at least the second of those phases.

There are some disagreements between our result and other results obtained theoretically and more important experimentally. The length scale in the experiment is smaller than

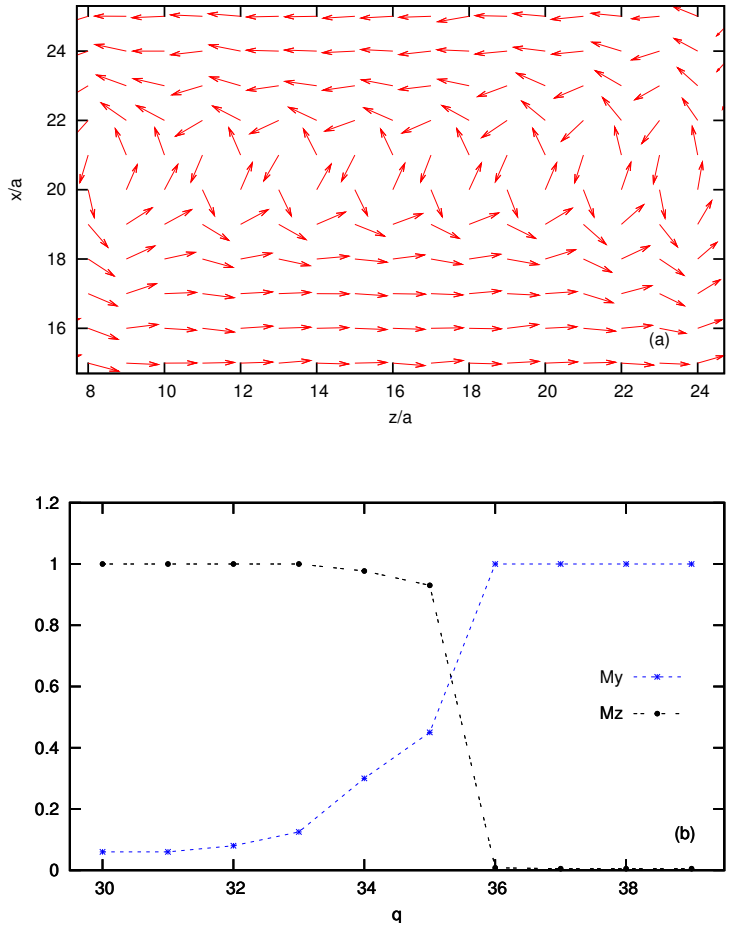

Figure 4.5: (Color online) Transition to $F_\perp/P_\parallel$ from $F_\parallel$. (a) For q slightly smaller than q_{c2}, large Mermin-Ho vortices appear between the stripes (plaquette size $a = 4$ μm). $M_z(x,z)$ is plotted on the horizontal axis, $M_x(x,z)$ on the vertical axis and $M_y(x,z) \approx 0$ for the whole region shown at this instant. (b) Consequently, the maximum value of the Fourier transform of the magnetization out of plane $M_x(k_z^{max})$, see Eq. (4.46), increase before the phase transition. Simulation variables: $|\tilde{c}_2|\bar{n}_{3D} = 450$ Hz, $c_d\bar{n}_{3D} = 7.2$ Hz and $q = 35$ Hz (a), $q = 30 - 39$ Hz (b).

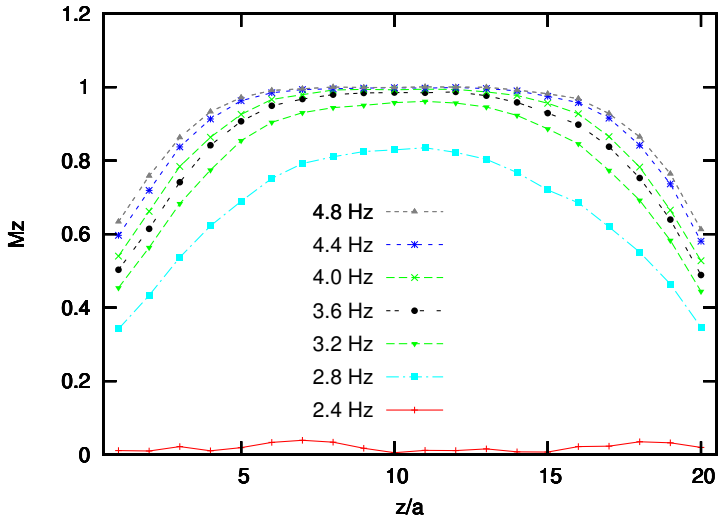

Figure 4.6: (Color online) Transition to $P_\perp$ from $F_\parallel$. The parallel magnetization $M_z(z/a)$ is plotted for different values of $|\tilde{c}_2|\bar{n}_{3D} = 2.4 - 4.8$ Hz as a function of z/a. The magnetization is lowered at the boundaries around the transition point for a finite system. Simulation values: $N = 20 \times 20$, $c_d\bar{n}_{3D} = 5.7$ Hz and $q = -4$ Hz.

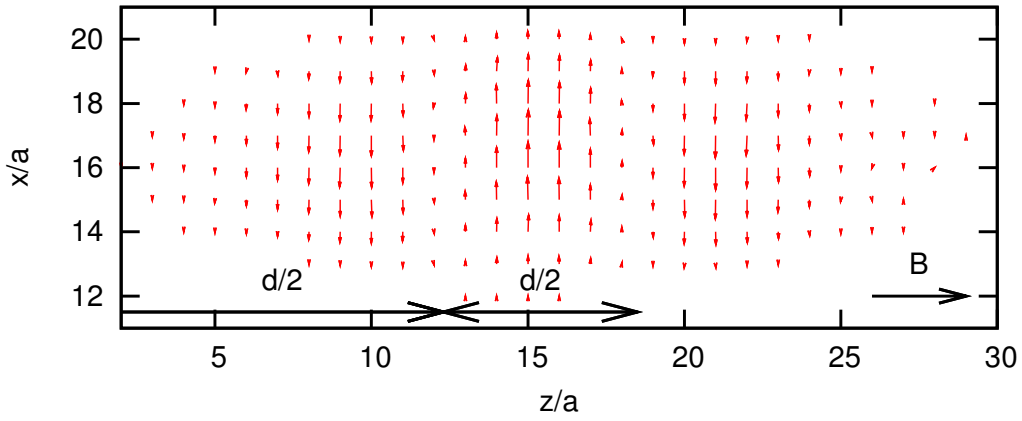

Figure 4.7: (Color online) Simulation of a helical modulated magnetized condensate in an elliptical trap. $\bar{n}_{3D}(x,z)M_z(x,z)$ is plotted on the horizontal axis, $\bar{n}_{3D}(x,z)M_x(x,z)$ on the vertical axis, and $M_y(x,z)$ is a quarter of a wavelength ahead of $M_x(x,z)$ as in Fig. 4.4, but is not shown. The wavelength $\lambda(z)$ of the helical modulation increases with decreasing density along the longitudinal axis. The distance between two neighbouring nodes is shown; the node to the left of them is outside the graph. Simulation parameters: $v_z = 1$, $v_x = 10$, $|c_2|\bar{n}_{3D} = 540$ Hz, $c_d\bar{n}_{3D} = 1.6$ Hz and $q = 120$ Hz.

the pitch of the helical modulation we describe above by a factor 10, roughly, for typical parameters. Cherng and Demler [39] find a dynamical instability at a scale nearer that seen in experiment. That picture would suggest that even if the phase diagram obtained here describes the system at long times, the experimental system might instead reach a long-lived metastable state. As explained in section V above, while we do see metastable states in some parts of the phase diagram, we do not see metastable checkerboard states in the region probed by current experiments, but this could be because the Metropolis dynamics of our simulation is not the actual dynamics of the condensate, even if their thermodynamics are the same.

One challenge for this dynamical scenario is that in experiments, an imposed helical configuration with pitch $\lambda = 50 - 150\mu$m [36] quickly evolves into a state modulated at a smaller scale, again roughly ten times smaller than the stable, or at least metastable, supersolid state we predict. [36, 37] This suggests that effects we have not taken into account prevent the current experimental system from finding this minimum. As an example, it is known that the dipole interaction makes the Larmor precession unstable, according to Lamacraft [40]; as a result, the Larmor-averaged energy that is the main focus of the present work might not be an accurate description for long times.

In order to observe the predicted supersolid clearly, our results suggest that the key is to suppress this Larmor instability while at the same time preserving the conservation of total magnetization in the field direction. The Larmor instability [40] grows exponentially from thermal excitation of an initial perturbation at the Larmor frequency ω_L. Hence the time scale to reach a fixed final size of the instability is proportional to $\hbar\omega_L/(k_B T)$ and can be increased either by increasing the magnetic field or decreasing the temperature. At the same time, an experiment should be designed to preserve the magnetization along the field direction for as long as possible, which requires a high degree of trap uniformity. One motivation for continued exploration of this system is that our results show that the Larmor-averaged system does have a supersolid ground state for a wide range of parameters.

Note added: As this work was being prepared for submission, two e-prints appeared investigating the same experiment by slightly different approaches. [52, 53] The first, by J. Zhang and T.-L. Ho, also investigates the static properties of ^{87}Rb using a deterministic numerical method and also gets the $F_\parallel$ state and a modulated $F_\perp$ state. The main difference between their results and ours appears to be that they find a stripe phase rather than a helix for the phase with spins perpendicular to the applied magnetic field. They find arrays of elliptical and hyperbolic Mermin-Ho vortices, as a meta-stable dynamical state, between the stripes for the $F_\parallel$ state for all q. However, they are smaller than the spin healing length and hence unobservable in our simulation, although we do see them close to the transition to the $F_\perp/P_\parallel$ state. The second, by Y. Kawaguchi *et al.*, finds a doubly periodic (checkerboard) spin pattern as a long-lived intermediate state through a combination of mean-field theory and numerical simulation of precession-averaged equations of motion. By adding energy dissipation to the dynamics, they reach a stationary state similar to ours.

Acknowledgments

The authors thank Subroto Mukerjee, Dan Stamper-Kurn, Mukund Vengalattore, Kater Murch, Jennie Guzman, Andre Wenz, Ari Turner, and Ashvin Vishwanath for useful comments and acknowledge support from ARO through the OLE program (J. K., J. E. M), Knut and Alice Wallenberg foundation (J. K.) and WIN (A. E.).

Chapter 5

Detecting fractional quantum Hall phases in optical lattices

5.1 Introduction

Fractional quantum Hall (FQH) phases [13, 54] contain a wide variety of interesting physics, including topologically degenerate ground states, fractional bulk excitations, and gapless chiral edge excitations. They arise at low temperatures when strong magnetic fields are applied to high-quality two-dimensional electron gases with low carrier concentration. Ultracold gases of neutral atoms are being used to investigate several properties of materials which can be hard to control precisely in the solid state. As these systems are charge-neutral, an ordinary magnetic field cannot be used to create the Lorentz force. A synthetic magnetic field can be created by rotation, but technical issues appear to limit this approach to lower field strengths than are necessary for FQH [55], with the exception of a recent experiment with few trapped particles [56]. Much theoretical work has been done for these systems, for a review see [22], including edge spectrum calculations [57].

Recently, several theoretical [14, 58, 59] and experimental [55, 60] proposals have been made for stronger synthetic magnetic fields for ultracold neutral atoms. All of them can be used with optical lattices which enhance interaction effects and give a larger energy gap above the FQH ground state. Theoretical work on lattice systems with an effective magnetic field goes back at least to Hofstader's work [10] on non-interacting particles; the FQH phases are strongly interacting, and Sørensen et al. [14] showed that in the low flux limit and strong interactions the system could be well described by Laughlin's wavefunction [61]. In subsequent work Hafezi et al. [62] concluded that this could be extended to larger fluxes per unit cell by investigating the topological structure of the ground state.

The goal of this work is to understand practical experimental conditions for observation of edge states in bosonic lattice FQH systems and compare numerical results for edge excitations in hierarchy states to the prediction of chiral Luttinger liquid theory [9]. Convincing observation of bosonic FQH states will depend on an experimentally viable probe

of the topological order; while many multi-particle quantities have been used to diagnose the topological state in past theoretical work, such as ground state degeneracy, bulk energy gap, wavefunction overlap, band flatness, band Chern number and entanglement spectra, these are not yet experimentally accessible. Our focus will be on edge excitations, whose "universal" aspects contain information about the topological order of the system, although a good understanding of the "non-universal" effects of the lattice and trap is crucial for these excitations to provide a clear signal that a FQH phase has been obtained.

5.2 The model

We investigate bosonic FQH phases in the simplest lattice system, hard-core bosons on a square lattice in a uniform magnetic field with equivalent Landau level filling $\nu = N/N_\phi$. N is the number of bosons and N_ϕ is the number of fluxes in the system, measured in units of the magnetic flux quantum $\Phi_0 = hc/q$, for particles of charge q. The modified Bose-Hubbard Hamiltonian is,

$$H = -J \sum_{\vec{r}} \hat{a}^\dagger_{\vec{r}+\hat{x}} \hat{a}_{\vec{r}} e^{-i\alpha_x y} + \hat{a}^\dagger_{\vec{r}+\hat{y}} \hat{a}_{\vec{r}} e^{i\alpha_y x} + h.c., \tag{5.1}$$

where J is the hopping amplitude, $\hat{a}^\dagger_{\vec{r}}$ creates a boson on site $\vec{r} = (x, y)$. We use two different gauges for the phases $\vec{\alpha} = (\alpha_x, \alpha_y)$, Landau gauge $\vec{\alpha} = (\alpha, 0)$ on cylinders to keep explicit translational symmetry around their circumferences, and symmetric gauge, $\vec{\alpha} = (\alpha/2, \alpha/2)$ on squares to keep explicit $\mathbb{Z}_4$ rotational symmetry. The flux through a plaquette $n_\phi = \alpha/2\pi$ is defined modulo 1 and can be expressed as an artificial magnetic field $\vec{B}^* = n_\phi \Phi_0/a^2 \hat{n}$, where a is the lattice spacing and $\hat{n}$ the vector normal to the lattice plane. At low flux $n_\phi \ll 1$, a continuum description can be used and the system is effectively in the flat band limit [63]. We focus on larger fluxes where the lattice is important. The magnetic length l_B is of the same order as the lattice spacing for the fluxes we are interested in, $l_B = \sqrt{\hbar c/(qB^*)} = a/\sqrt{2\pi n_\phi} \sim a$.

The spectrum of the Hamiltonian (5.1) is computed with exact diagonalization. A section of the system is shown schematically in Fig. 5.1(a). The edge excitations in an infinite system are gapless, but become gapped in a finite system. To clearly see them, it is desirable to have a large bulk gap $\Delta E^B_\nu/J \equiv (E^B_\nu - E^{GS}_\nu)/J$, where E^B_ν is the energy of the lowest bulk excitation and E^{GS}_ν the ground state energy in the ν phase. The bulk gap on cylinders at $\nu = 1/2$, in flat infinite wells where edge modes do not exist, are shown in Fig. 5.1(b). The ground state is non-degenerate and the gaps to all excited states are comparable to those reported for a torus [14]. To get edge excitations in the spectra, more sites outside the ground-state droplet need to be added where the edge waves can propagate. A trapping potential is then essential to confine the condensate.

The optical trapping potential $V_{\text{trap}}(x, y)$, provides the equivalent of the electric field confinement in semiconductors. In this chapter, we use harmonic traps $V_{trap}(x, y) = V_x x^2/a^2 + V_y y^2/a^2$ to get one edge on squares and two edges on cylinders, with $V_x = 0$ in the periodic direction of the cylinder. The velocity of a non-interacting particle near the edge is

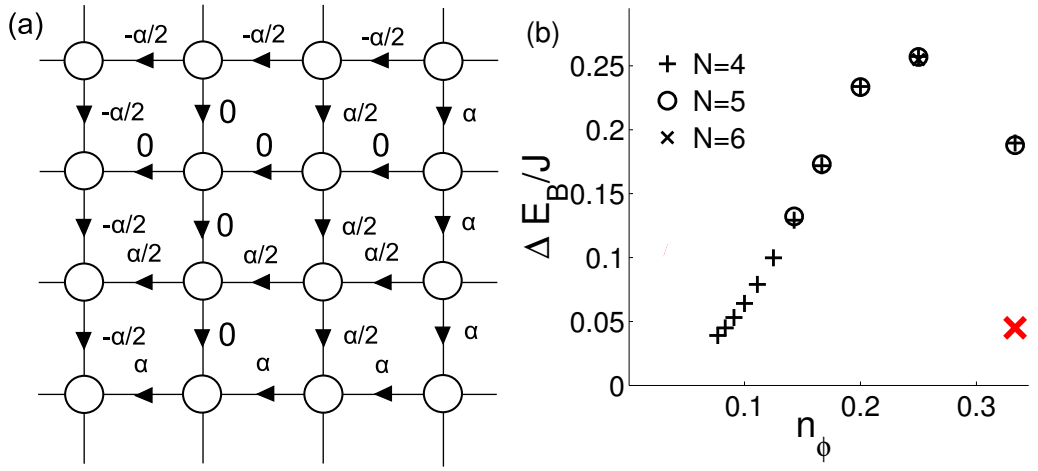

Figure 5.1: (Color online) (a) Part of the square lattice in the symmetric gauge with the phases gained when hopping in the direction of the arrows. When hopping in the opposite direction, the phases are the complex conjugate of those shown. (b) The bulk gap in the $\nu = 1/2$ phase on a cylinder as a function of flux per plaquette, for $N = 4 - 6$ particles. The large red cross is from a clearly different spectrum, indicating that it might not be in a FQH phase.

$v = |\nabla V_{\text{trap}}(r_c)|/(n_\phi hc/a^2)$, where r_c is the radius of the ground state droplet. The edge excitations of FQH phases form chiral Luttinger liquids. In the hydrodynamical approach [9], the Hamiltonian of the edge waves in the Laughlin phases $\nu = 1/m$, with $m = 2, 4, 6, ...$ for bosons, is

$$H_{1/m} = 2\pi \frac{v}{\nu} \sum_{k>0} \rho_{-k}\rho_k, \tag{5.2}$$

with $[\rho_k, \rho_{k'}] = \frac{\nu}{2\pi} k\delta_{k+k'}$ where $\rho_k = L_e^{-1/2} \int d\theta e^{ik\theta/\hbar}\rho(\theta)$, $k = ph/L_e$ with $\rho(\theta)$ the one-dimensional density along the edge, $p \in \mathbb{N}$ and L_e is the length of the edge. This is the $U(1)$ Kac-Moody algebra, describing a set of k uncoupled harmonic oscillators with energy $\sum_p l_p vk$ and momentum $\sum_p l_p k$, where $l_p \in \mathbb{N}$ counts the number of excitations in each mode. For a single edge, the degeneracies of the edge spectrum are $1, 1, 2, 3, 5, 7, 11, 15, 22, ...$, see Tab. 5.1 for a labeling of the different states. On a cylinder, there are two edges with momentum in different directions, right moving (R) and left moving (L). The degeneracies of this edge spectrum are $1, 2, 5, 10, 20, ...$ or $(1), (1, 1), (2, 1, 2), (3, 2, 2, 3), (5, 3, 4, 3, 5), ...$ if momentum is also resolved (Tab. 5.1). The wavefunctions in the microscopic theory of edge states for the

	One edge	Two edges				
E	p= $EL_e hv$	p= 0	p= 1	p= 2	p= 3	p= 4
0	GS	GS				
hv/L_e	1		1R			
$2hv/L_e$	2			2R		
	11	1R1L		11R		
$3hv/L_e$	3				3R	
	21		2R1L		21R	
	111		11R1L		111R	
$4hv/L_e$	4					4R
	31			3R1L		31R
	22	2R2L				22R
	211	2R11L+11R2L		21R1L		211R
	1111	11R11L		111R1L		1111R

Table 5.1: Labeling of the edge spectra for one and two edges: $2 \equiv \{l_2 = 1, l_i = 0 \text{ if } i \neq 2\}$, $111 \equiv \{l_1 = 3, l_i = 0 \text{ if } i \neq 1\}$ and so on. All edge levels with energy $E \leq 4hv/L_e$ and positive momentum $p \geq 0$ are shown. For two edges, the levels with $p < 0$ are equivalent to those with $p > 0$, with L and R exchanged.

Laughlin phases are

$$\Psi_{1/m}(z_i) = P(z_i) \prod_{i<j} (z_i - z_j)^m e^{-\sum_i |z_i|^2/4l_B^2}, \tag{5.3}$$

where $P(z_i) = \sum_p (\sum_i z_i^p)^{l_p}$. This is the form of all zero energy wavefunctions without a trap. For a small number of particles, the edge excitations consisting of a few single particle modes $n_p = \sum_p l_p$ extends a distance $\Delta r \lesssim n_p l_B$ outside the ground state droplet.

5.3 Circular trapping potential

First, we consider the circular harmonic trap on a square lattice. With an appropriate construction of the $\mathbb{Z}_4$ symmetric Hamiltonian, a Fourier transform will turn the Hamiltonian into block diagonal form with each block corresponding to a certain angular momentum $L/\hbar = 0, 1, 2, 3, ...$ mod 4. These momenta $k_c = \Delta L/r_c$, with $\Delta L \equiv L - L^{GS}$, are the same as in the Kac-Moody algebra $k = ph/(2\pi r_c)$. The analytic edge spectrum for the $\nu = 1/2$ phase is shown in Fig. 5.2(a). In a system with finite number of particles N, we only expect excitations consisting of $n_p \leq N$ single modes. The energy is proportional to the angular momentum for the trapped phase, indicated by the straight dotted line. With only $N = 4$

anal\num	GS	1	2	11
GS	0.978	$3 \cdot 10^{-24}$	$1 \cdot 10^{-26}$	$7 \cdot 10^{-28}$
1	$3 \cdot 10^{-24}$	0.974	$3 \cdot 10^{-27}$	$1 \cdot 10^{-26}$
2	$1 \cdot 10^{-26}$	$2 \cdot 10^{-27}$	0.971	$6 \cdot 10^{-4}$
11	$2 \cdot 10^{-27}$	$4 \cdot 10^{-25}$	0.041	0.934

Table 5.2: Overlap between the calculated wavefunctions corresponding to the four lowest energy levels in Fig. 5.2(b) and the first four zero-energy wavefunctions in Eq. 5.3, labeled as in Tab. 5.1.

particles on a 11×11 site lattice in a trap $c_a/J = 0.02$, we get remarkably good edge spectra. At $n_\phi = 1/5$, the filling fraction of the ground state is $\nu = 1/2$. The degeneracies $1, 1, 2, 3, 5, 6, 9, 11, 15, ...$ in the edge spectrum, agreeing with $n_p \leq N$ for $\nu = 1/2$, is clearly visible, see Fig. 5.2(b). A straight line is a good fit to the lowest excitation at each momenta. The small energy splitting is due to finite size effects, most noticable in the states that extends furthest in the trap. Note that all of these state appear to be edge states; there are no bulk excitations for $\Delta E_{1/2}/J \equiv (E_\nu - E^{GS}_{1/2}) \lesssim 0.35$, where E_ν is the energy of a state in the ν phase, much larger than the anticipated gap $\Delta E^B_{1/2}/J \approx 0.23$. The numerical wavefunctions $\Psi^{num}_{1/2}(\{l_p\})$ of these edge excitations have a highly non-trivial overlap $O(\{l_p\}, \{l'_{p'}\}) = |\langle \Psi^{num}_{1/2}(\{l_p\}) | \Psi^{anal}_{1/2}(\{l'_{p'}\})\rangle|^2$ with the normalized microscopic wavefunctions $\Psi^{anal}_{1/2}(\{l_p\})$ in Eq. 5.3, discretized on a lattice, see Tab. 5.2 for a few examples. The overlaps are also insensitive to the trap potential used V_r, confirming the incompressibility of the states.

Possibly the easiest way to experimentally measure the edge spectra is with stimulated two-photon Bragg scattering [64]. The probe light is scattered when the energy and momentum difference between the two beams is resonant with an excitation level in the FQH system. Inserting typical experimental values $J = \hbar/\tau_{tunnel}$, with a tunneling time $\tau_{tunnel} = 0.2$ ms and $a = 400$ nm gives an edge velocity $v = \Delta E_\nu/(\Delta L/r_c) \approx 0.2$ mm/s. Resolving the closest energy excitations at the same angular momenta might initially be challenging. However, the linear relation v should be well within experimental reach with a long pulse duration $\delta t \sim 10$ ms in the Bragg spectroscopy during which the condensate has to remain stable. Modulation of the trapping potential is another commonly used technique to produce small energy excitations [65]. Detecting edge excitations could potentially also be done by mapping out the in-situ density profile of the condensate and an excited state, to observe the propagating edge mode, or performing the analog to tunneling interferometry in condensed matter, either between the edges of two condensates trapped next to each other [66] or by outcoupling atoms from opposite points of the con- densate.

There are several states [Fig. 5.2(b)] that do not belong to the $\nu = 1/2$ edge spectrum. The lowest of those states has a $\nu = 2/3$ filling factor. The $\nu = 2/3$ FQH phase has a 3-fold degeneracy on a torus and Möller et al. [67] showed it has a good average overlap with

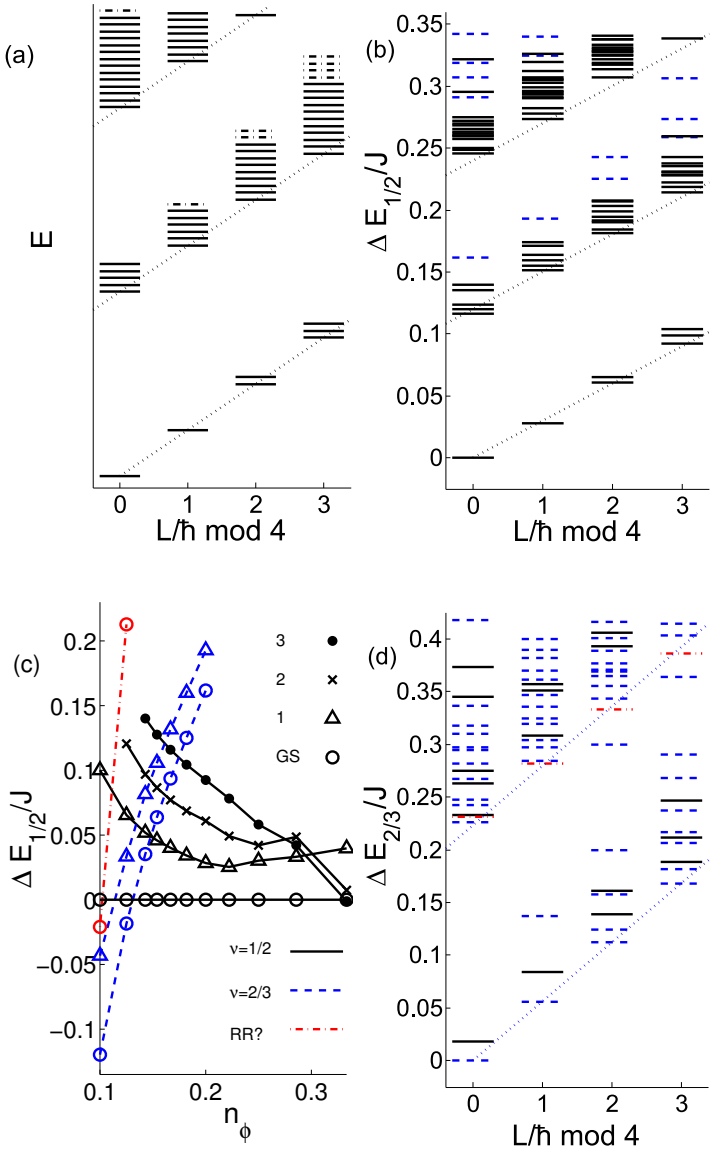

Figure 5.2: (Color online) (a) Analytic edge spectrum at $\nu = 1/2$ in a trap as a function of angular momenta. Degenerate lines are drawn slightly apart for clarity. The solid lines corresponds to excitations consisting of four single particle modes or less. The dashed dotted lines are the additional excitations appearing for additional modes. (b)-(d) Edge excitations for $N = 4$ particles on a 11×11 square lattice in a circular harmonic trap, $\nu = 1/2$ black solid lines, $\nu = 2/3$ blue dashed lines and the possible Read-Rezayi (RR?) phase, red dashed dotted lines. (b) Edge spectrum at $n_\phi = 1/5$ as a function of angular momentum. (c) Energy gap to the $\nu = 1/2$ ground state for: ground states ($\circ$), 1 states ($\triangle$), 2 states ($\times$) and 3 states ($\bullet$), labeled as in Tab. 5.1, as a function of flux per plaquette. (d) Edge spectrum at $n_\phi = 1/8$ as a function of angular momentum.

the composite-fermion wavefunction for $n_\phi \lesssim 0.3$ on a lattice. Varying the magnetic flux slightly, states in the same phase change their energy in a similar manner, see Fig. 5.2(c) for some examples. At small flux per plaquette, our system can become too small for some of the excited states of $\nu = 1/2$ to exist. Upon decreasing the flux further, other phases appear with larger ground state filling factors, consistent with some of the phases in the Read-Rezayi sequence for bosons $\nu = g/2$, where $g \in \mathbb{N}$ [68]. Whether these phases actually are FQH phases are left for future studies. Again, around $n_\phi \approx 0.3$, the edge spectrum break down and it is unclear what phases exist for $n_\phi \gtrsim 0.3$.

The $\nu = 2/3$ hierarchical state [69], consists of two condensates with comoving edge modes at different radii. This spectrum has the same degeneracies as two edges on a cylinder $1, (1,1), (2,1,2), (3,2,2,3), ...$, but states within each set () now have the same angular momentum, not energy. The edge spectra in Fig. 5.2(d) is at $n_\phi = 1/8$, where the ground state energy for $\nu = 2/3$ is slightly lower than for $\nu = 1/2$. The $\nu = 1/2$ edge excitations are spaced further apart, but the states with degeneracies $1, 1, 2, 3, 5$ can still be clearly distinguished. The two $U(1)$ branches of $\nu = 2/3$ have very different velocitiess, but the structure $1, 2, 5$ can easily be seen under the dotted line corresponding to the lowest energy for the higher angular momentum states.

5.4 Elliptical trapping potential

Next, we consider a square lattice on a finite cylinder with a harmonic trap in the non-periodic direction, which should be a good approximation to an elliptical elongated trap. The cylindrical system in Landau gauge has a $\mathbb{Z}_{L_x}$ symmetry along the circumference of the cylinder, when $\alpha_x = 2\pi/L_x$. With an appropriate construction of the Hamiltonian, a Fourier transform will turn the Hamiltonian into block diagonal form with each block corresponding to a certain momentum $k_x = p_x h/L_x = ..., -h/L_x, 0, h/L_x, ...$ mod h along the circumference of the cylinder. These are the same momenta as in the Kac-Moody algebra with $k_x = k$.

The edge spectrum on a cylinder in a 1-D harmonic trap $c_y/J = 0.004$, is shown in Fig. 5.3(a). Three additional rows are required outside the ground state droplet on both edges to get all edge excitations with $|p_x| \leq N$. No edge excitations with $|p_x| > N$ are found on any cylinder. The edge states 111R1L, 1R111L, 1111R and 1111L are higher up in the spectrum and not shown. The discrepancy from the analytical spectrum, shown in Fig. 5.3(b), can be explained by two types of finite size effects. The lower-than-expected energy of the high momentum single particle modes depends on their overlap with the opposite edge, the increase is again from finite size effects especially in the furthest extending states. Bulk excitations are shown with red lines. The bulk gap $\Delta E^B_{1/2}/J \approx 0.12$ is again larger than anticipated, $\Delta E^B_{1/2}/J \approx 0.08$ in Fig. 5.1(b).

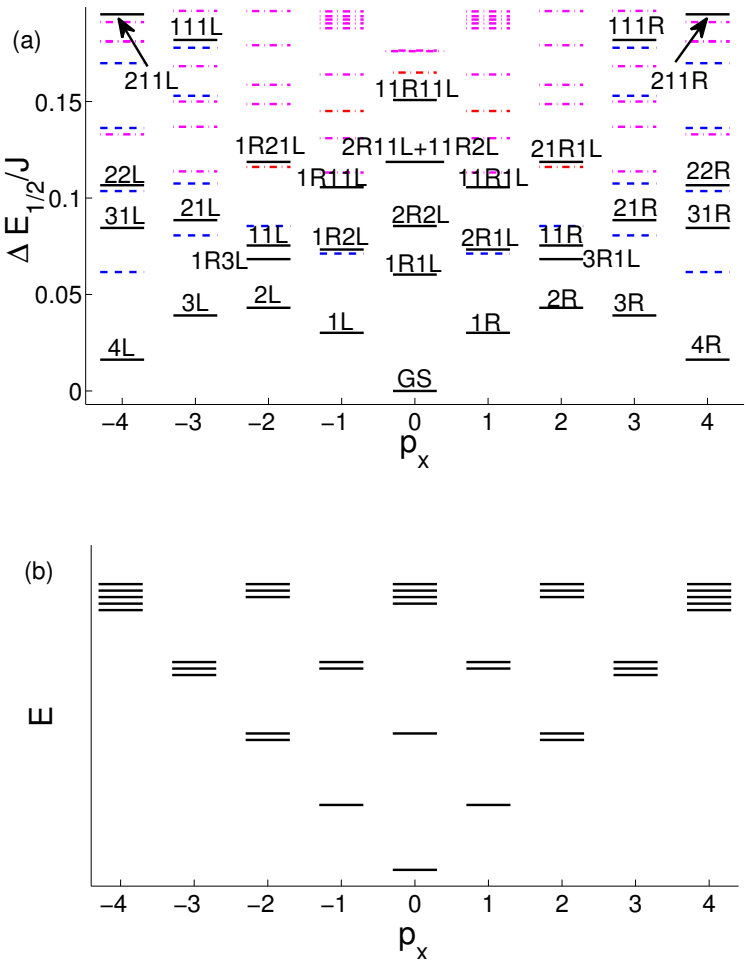

Figure 5.3: (Color online) (a) Edge spectrum for $N = 4$ particles at $\nu = 1/2$ on a 9×15 site cylinder in a harmonic trap as a function of momenta. Apart from the expected edge spectrum (black solid lines), bulk excitations (red dash-dotted lines) and edge excitations from translated $\nu = 1/2$ phases (blue dashed and magenta dashed-dotted lines, where the former are aliased to a lower momenta) are mixed in. Two-fold degenerate states are marked with longer lines. (b) Analytic edge spectrum at $\nu = 1/2$ for a large system. Degenerate lines are drawn slightly apart for clarity.

5.5 Discussion

We briefly discuss finite size effects, the influence of the trap and other possible FQH phases that could be observed. The number of particles we can use in our edge states calculations, is restricted by the large Hilbert space ($> 8 \cdot 10^6$ for the data presented here). It grows fast, mainly due to two reason; no projection to the lowest Landau level and the additional sites outside the GS droplet required for the higher edge excitations. Still, the diameter of the GS droplet d_{GS} is substantially larger than the magnetic length (which is comparable to the correlation length); $d_{GS}/l_B = \sqrt{8N/\nu}$. The good agreement with analytical edge excitation results and calculations with $N = 3$ and $N = 5$ (only for certain system sizes), make us believe that signs of the topological order can be seen already in these limited systems. Experimental systems will be larger, but trying to increase the system size further is likely not the the most important modification for observing a FQH phase. Apart from some finite size effects seen in our results, from N and the lattice which we have tried to comment about, the interesting experimental tuning parameters are the flux per plaquette and the trap. The GS droplet can cover any area, since n_ϕ can take on any value, not just fractional. Increasing the trapping potential V_r favors denser phases and the transitions to FQH phases with higher filling fractions ν will hence occur at larger fluxes n_ϕ. It also increases the spacing $\Delta E_\nu \propto V_r/J$, between edge excitations with different L, for reasonable trap strengths, making them easier to observe experimentally. Replacing the harmonic trap with another trap shape can change the spectra completely in circular traps $V_{\text{trap}} = V_r r^b$. The system shows a FQH edge for $1.5 \lesssim b \lesssim 2.5$ with the best spectra at $b = 2$. However, the edge spectra does not change much with b on a cylinder. Hence, this might be a finite size effect, larger systems can have FQH phases for a larger range in b. Still a harmonic trapping potential is likely the best for experiments, especially for smaller systems.

Lastly, we discuss which other FQH phases in optical lattices that potentially can be detected with our method. The other phases in the bosonic Laughlin sequence $\nu = 1/4, 1/6, ...$ cannot be the ground state without longer range repulsions in a trap [62]. In a trap, their ground state energies are higher than the energies presented here. With decreasing magnetic field, we do not observe the higher order hierarchical states at $\nu = 3/4, 4/5, ...$ But, we believe this is an artifact of the small systems studied. The non-abelian phases in the Read-Rezayi sequence $\nu = 1, 3/2, 2, 5/2, ...$ [68] are believed to be the ground state for bosons in a trap under certain conditions [70, 71]. The $\nu = 3/2$ phase is the simplest bosonic FQH phase that could be used for quantum computing [72]. In the other limit, at large flux per plaquette $n_\phi \approx 1/2$ (1/3), are the lattice specific FQH phases believed to appear [63, 67, 73]. We considered lattices with uniform flux; recent work has shown convincingly that non-uniform magnetic fields can create the same FQH phases without Landau levels [74–79]. The lessons in this work for trapping potentials and geometries apply also to these more complex situations. For completeness we mention a few recent proposals, see Refs. [80–83] , for detecting quantum Hall physics in ultracold gases in other ways than measuring the edge excitations.

5.6 Conclusions

The main result of this work is that hard-core repulsion in a small simple lattice system of approximately square or circular geometry is sufficient to generate clearly resolved edge excitations for the bosonic FQH states at filling $\nu = 1/2$ and $\nu = 2/3$, provided that the conditions described above on flux per site and harmonic trap strength can be achieved; engineering flat or nearly flat bands is unnecessary. In the cylindrical case, the edges are strongly interacting with each other and the edge excitations are much harder to distinguish, which suggests counterintuitively that increasing system size by going to an elongated trap may not be necessary or even desirable. Observation of the bosonic FQH states discussed here would be a logical first step toward even more exciting new states that can be studied by similar methods.

Acknowlegdments

The authors acknowledge helpful conversations with J. Guzman, G.-B. Jo, R. S. K. Mong and S. Parameswaran and support from the ARO Optical Lattice Emulator program.

Part IV

Quantum Spin Chains

Chapter 6

E_8 symmetry effects in perturbed quantum Ising chains

6.1 Perturbed quantum Ising chains

The one-dimensional (1D) quantum Ising model in transverse and longitudinal fields is one of the most studied theoretical models in condensed matter physics. It is a relatively simple model that contains very rich physics; for example, it contains a quantum critical point (QCP) at zero longitudinal field related to the 2D classical Ising model. A remarkable fact is that the integrability present at the critical point remains under addition of a longitudinal field as a mass-generating perturbation. Zamolodchikov conjectured in 1989 an S-matrix describing eight emergent particles whose mass ratios are connected to the roots of the Lie algebra E_8 [84, 85]. Recently, Coldea et al. performed neutron scattering experiments on $CoNb_2O_6$ (cobalt niobate), a material that to a good approximation can be described by a quantum Ising chain. At low temperatures and in the presence of a strong external transverse magnetic field which tunes the system to near criticality, the observed spectrum shows characteristic excitations of the E_8 symmetry [1].

However, a serious problem in comparing theory and experiment is that the real material has additional couplings that strictly speaking invalidate the exact solution, and until recently it was impractical to extend the theory non-perturbatively to include these couplings. In this Letter, we study a theoretical model for $CoNb_2O_6$ which includes in addition to the Ising interaction other interactions arising from the lattice structure and the weak coupling between the chains. Using this model, we calculate the dynamical spectral function and compare the results to the observed spectra. Close to the QCP, the model retains features expected from the quantum Ising model, in particular the characteristic particles of the E_8 symmetry.

6.2 Theoretichal model of $CoNb_2O_6$

We begin by deriving the theoretical model used to describe the low-energy physics of $CoNb_2O_6$. The spin lattice structure consists of chains of easy axis spins, realizing a two level system, on the Co^{2+} ions coupled by a ferromagnetic Ising interaction along the chain direction, see Fig. 6.1A. We thus start from the quantum Ising chain, described by the Hamiltonian

$$H = -J\sum_n S_n^z S_{n+1}^z - h^x \sum_n S_n^x \tag{6.1}$$

where $J > 0$ favors a ferromagnetic state ($|\uparrow\uparrow ... \uparrow\rangle$ or $|\downarrow\downarrow ... \downarrow\rangle$). When the transverse field is increased past the QCP $|h_c^x| = J/2$, the system undergoes a phase transition into a paramagnetic state $|\rightarrow\rightarrow ... \rightarrow\rangle$. This model is exactly solvable using a Jordan-Wigner transformation which transforms the spins into non-interacting fermions [7].

The lowest lying excitation energy is similar on both sides of the QCP due to the self-duality of the model and goes to zero, that is, the gap closes, at the QCP. However, the double degeneracy of the ferromagnetic ground state leads to a fractionalization of the experimental excitation, a spin flip, into two freely moving domain walls or kinks. We now take into account terms which result from the three-dimensional (3D) lattice structure of $CoNb_2O_6$. A recent theoretical study by Lee *et al.* investigates a three-dimensional model of $CoNb_2O_6$ [86]. They show that the plane perpendicular to the chain, a weakly coupled triangular lattice, see Fig. 6.1A, has ferrimagnetic order to transverse field strengths well passed h_c^x. The interchain couplings in a 3D magnetic ordered material at low temperature can be well approximated by a chain in a local effective longitudinal field $h^z = \sum_\delta J_\delta \langle S^z\rangle$ with the sum over all nearest interchain bonds [87]. This field favors the ferromagnetic phase, breaks its two-fold symmetry and moves the system away from the QCP. It also splits up the continuum into bound states by confining the kinks. At low transverse field and small bound state momentum, this can be described by a one-dimensional Schrödinger equation with a linear confining potential with the energy levels given by the negative zeros of the Airy function, see Fig. 6.1B [88]. This solution has later been extended to all possible bound state momenta [89]. Close to the QCP ($h^x = h_c^x, |h^z| \ll |h_c^x|$), the eight massive particles described by the E_8 symmetry can be seen either as asymptotic states or as bound states of a pair of particles of this theory [84, 85].

Although $CoNb_2O_6$ to a good approximation can be described by a quantum Ising chain, a realistic model must contain more interactions [90]. It has a strong easy axis character, but a weak XX part is still present. The chains have a zig-zag structure, making the next-nearest neighbor (nnn) interaction important as well, see Fig. 6.1A. The measured Ising exchange energy J is unusually low, likely due to a competition from an antiferromagnetic nnn interaction. Taking into account all terms, the resulting Hamiltonian reads

$$\begin{aligned} H &= -J'\sum_n S_n^z S_{n+1}^z - h^x \sum_n S_n^x - h^z \sum_n S_n^z \\ &- J_p \sum_n \left(S_n^x S_{n+1}^x + S_n^y S_{n+1}^y\right) + J_B \sum_n S_n^z S_{n+2}^z. \end{aligned} \tag{6.2}$$

The numerical values for the coupling constants to describe $CoNb_2O_6$ are obtained by matching the experimental neutron scattering intensity at zero applied transverse field with our numerical calculations. We compare the dynamical structure function $S^y(k,\omega)$, the Fourier transform of the dynamic two-point correlations

$$C^y(n,t) = \langle\psi_0|S^y_n(t)S^y_0(0)|\psi_0\rangle. \tag{6.3}$$

6.3 Time evolution

For the numerical calculations, we use the time evolving block decimation (TEBD) [29, 30] method which provides an efficient method to perform a time evolution of quantum states in one-dimensional systems. The evolution of a random state of an infinite chain in imaginary time is used to calculate the ground state $|\psi_0\rangle$ and an evolution in real time allows us to calculate the dynamic two-point correlations directly. The TEBD algorithm can be seen as a descendant of the *density matrix renormalization group* [91] method and is based on a matrix product state (MPS) representation [92**?**] of the wavefunctions. Algorithms of this type are efficient because they exploit the fact that the ground-state wave functions are only slightly entangled, especially away from criticality [93]. As the entanglement grows linearly as a function of time, the simulations of long time evolutions is numerically very difficult. To be able to simulate long enough times and thus to get sufficiently good energy resolution in the calculated spectral functions, we use a number of methods to accelerate the time evolution. We use linear predictions to extrapolate the dynamical correlation functions to very long times [94, 95] and take advantage of the "light-cone" like spread of the entanglement by adding more sites to the chain as time increases. As the calculation of the correlation functions $C^y(n,t)$ is numerically very expensive, we calculate it only for certain time steps and then interpolate its values. In order to estimate the errors of our simulations, we calculate the truncation error, i.e., the truncated weight of the wave function at a time step, which gives an upper bound for the truncation effects on local expectation values ($\lesssim 10^{-6}$ for all simulations presented in this chapter). In addition we also checked the dependence of the measured observables on the matrix dimension χ per site and the time steps Δt, settling for $\chi = 45$ and $\Delta t = 0.04$ meV^{-1} for the simulations presented in this chapter.

The numbers we use are $J' = J + J_B = 2.43$ meV, $h^x = 0.354$ meV, $h^z = 0.035$ meV, $J_p = 0.52$ meV and $J_B = 0.60$ meV, see Fig. 6.1C and compare it to Fig. 3 in Ref. [1]. A cross-section with the bound state "masses" (i.e., the energies of the bound states at zero momentum) is presented in Fig. 6.1D with the experimentally measured masses and Rutkevich's exact solution of Coldea *et al.* first order model for reference in Fig. 6.1D [1, 96]. Note that our full Hamiltonian agrees to first order in perturbation theory with the phenomenological model used there, although the coupling constant for that model is slightly larger than ours [90].

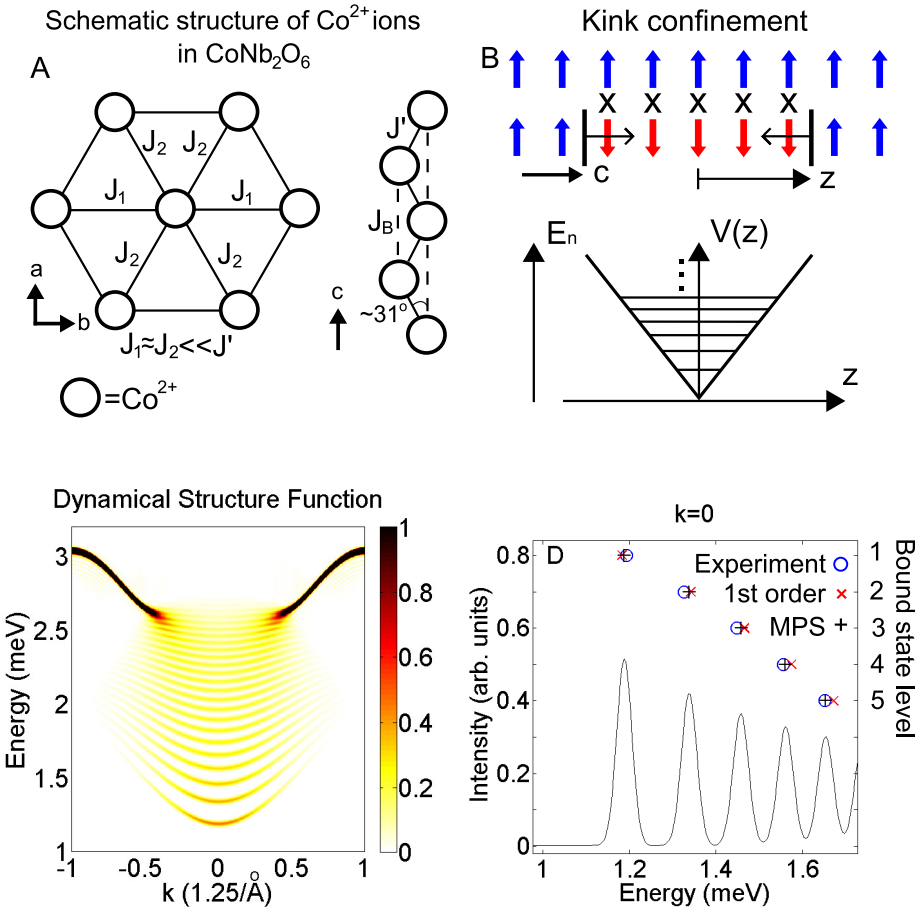

Figure 6.1: (Color online) (A) Ising spins on the Co^{2+} ions are strongly coupled in 1D along zig-zag chains. The Co^{2+} ions are ordered in a weakly coupled triangular lattice in the plane perpendicular to the chain direction, with **a**, **b** and **c** orthogonal unit vectors. (B) Confinement of kinks: the potential energy between kinks increase linearly, along the z coordinate in the **c** direction, as more interchain bonds turn energetically unfavorable. The energy levels are given by the negative zeros of the Airy function. (C-D) The full Hamiltonian describing $CoNb_2O_6$ at no external magnetic field. (C) The dynamical structure function. (D) The cross section of (C) at zero momentum showing the masses of the first five bound states. A comparison of these masses from our MPS calculations (pluses) with the experimental results (circles) and the exact solution of the proposed first order phenomenological model (crosses).

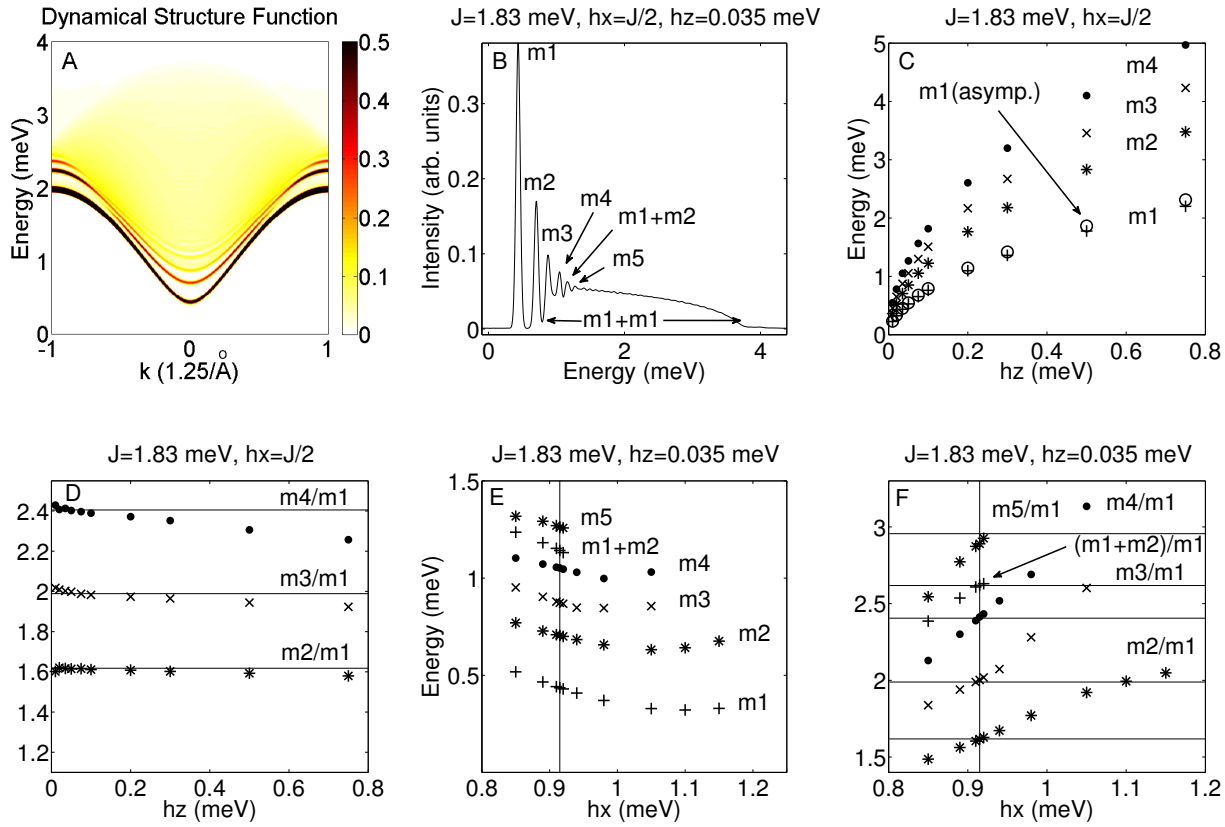

Figure 6.2: (Color online) Ising chain in a transverse and a longitudinal field. (A) The dynamical structure function at $h^x = h_c^x$ and $h^z = 0.035$ meV. (B) The cross section of (A) at zero momentum. The five lowest bound states and two bound state pairs can be distunguished. (C) ($h^x = h_c^x$) The mass of the four lowest bound states and an asymptotic expansion for m_1 from $h^z \to 0$ as a function of the longitudinal field. (D) ($h^x = h_c^x$) Relative mass of the lowest bound states compared to the analytical predicted values at $h^z \to 0$. (E) ($h^z = 0.035$ meV) The bound state masses as a function of the transverse field (h^x). The energy gap is smallest around $h^x = 1.10$ meV, however the minimum in the higher bound states occurs for lower fields. (F) ($h^z = 0.035$ meV) The relative masses for the bound states increases roughly linear as a function of the field (h^x) and passes the analytical calculated values at h_c^x.

6.4 Excitation spectra for a quantum Ising chain

Before investigating this model near the QCP, we start with a pure quantum Ising chain where the E_8 symmetry is expected to be present [84]. The dynamical structure function is calculated over the whole Brillouin zone (for various parameters $J = 1.83$ meV, h^x, h^z), see Fig. 6.2A for an example and we focus on the cross section at zero momentum where some comparison with earlier work can be done. Fig. 6.2B is an example of these cross sections at $h^x = h^x_c$ with $h^z = 0.035$ meV. The lowest four bound states can be easily detected and one or two more can be distinguished. Bound state pairs $m_1 + m_1$ (overlapping with m_3) and m_1+m_2 have similar intensity to the nearby bound states, making both types simultaneously observable. They are created in a "spinon jet", where the two kinks (also known as spinons) in a bound state have been stretched far enough apart to make it energetically favorable to flip a spin between them to form two more kinks that each form an independent low energy bound state with one of the original kinks. The independent motion of these two bound pairs appears as a continuum in the dynamical structure function. This process is reminiscent of quark dynamics, where the quarks are confined and cannot be isolated singularly. Finding condensed matter analogues of confinement effects known from high energy physics might help us to improve our understanding of underlying mechanisms; see e.g. Lake *et al.* [97].

The weight of the continuum decreases with increasing longitudinal field; this is also the case for the weight of the higher bound states but to a lesser extent. The gap and the spacing between the bound states increase with increasing longitudinal field; see Fig. 6.2C where data from more simulations are presented, together with an asymptotic expansion from the exact analytical limit ($h^x = h^x_c$, $h^z \to 0$) of the lowest bound state. The analytical expression for the gap is $m_1 \approx CJ/4(2h^z/J)^{8/15}$, with $C = 4.40490858/0.7833$, showing good agreement with our results to high longitudinal field strengths [84, 98]. (The spin is rescaled $S^z_{lat}(x) = 0.783(3)S^z_{cont}(x)$ from the continuum to the lattice model [99, 100].) The relative mass of these bound states related by the E_8 symmetry at h^x_c, are presented in Fig. 6.2D, again with good agreement in the analytically exact limit, see Tab. 6.1 [84].

m_2/m_1	m_3/m_1	m_4/m_1	m_5/m_1	m_6/m_1	m_7/m_1	m_8/m_1
1.618	1.989	2.405	2.956	3.218	3.891	4.783

Table 6.1: Analytically predicted mass ratios from Ref. [84]. These numbers result from evaluation of simple trigonometric expressions (e.g., $m_2/m_1 = 2\cos\pi/5$) that arise as eigenvalues of a matrix constructed from roots of the Lie algebra E_8.

The deviation of the asymptotic expansion is slightly larger for higher bound states. However, the deviation for large longitudinal fields ($h^z \lesssim h^x_c$) is fairly small, indicating influence of criticality up to very strong longitudinal fields. Note also that the uncertainty of our results increase with decreasing longitudinal field strength when the bound state masses move closer, due to our fixed energy resolution. For future reference we also present results as a function of the transverse field at longitudinal field $h^z = 0.035$ meV present in $CoNb_2O_6$

around $h^x = h_c^x$, see Fig. 6.2E. Good agreement for the energies of the bound states are obtained with earlier numerical work using the *Truncated Free Fermion Space Approach*, cf. Fig. 5 of Ref. [101]. Stronger longitudinal field will increase the minimum gap and move it to stronger transverse fields, but the gap increases slower away from its minimum value. Also note that the minimum for higher bound state masses occurs for a lower transverse field. The relative masses increase linearly around h_c^x, see Fig. 6.2F, with a steeper slope for higher bound state masses and lower longitudinal fields.

6.5 Excitation spectra for $CoNb_2O_6$

Finally we turn to the more accurate microscopic model of $CoNb_2O_6$ Eq. (6.2) with values of the coupling constants presented above. The QCP at zero longitudinal field for this model is moved to a slightly weaker field $h_c^x \approx 0.814$ meV, see Fig. 6.3A from ground state simulations with TEBD, due to the addition of the ferromagnetic XX-term. The longitudinal field strength from weakly coupled chains $h^z(\langle S^z \rangle)$ is to a good approximation constant past h_c^x, see Fig. 6.3A. At vanishing magnetization this is not true, but here the 1D approximation of the 3D material is breaking down anyway. The dynamical structure function at h_c^x, not presented here, shows a flattening of the kinetic bound state and a more prominent lowest bound state dispersion. The cross section at zero momentum, see Fig. 6.3B, has the same characteristics as the one for the quantum Ising chain, with fairly unaltered spectral weights. The relative weight of the bound state continuum is still largest around h_c^x, making this region even more interesting for experiments. A more careful analysis of the bound state masses, see Fig. 6.3C, reveals a small rescaling of both axes to around 90% of their previous values. This overall scaling does not affect the mass ratios, see Fig. 6.3D. Again they follow straight lines, see Fig. 6.3D, and pass the analytical values at h_c^x, exactly as they do for the quantum Ising chain, rather than approaching it by bending as suggested by the extrapolation of the experimental data in Ref. [1]. Additional interactions irrelevant at low field and not treated here might explain the bending if it is confirmed by higher resolution data, but our results suggest higher resolution data will show that the mass ratios indeed go through the analytical values at the critical field if the model used here (and previously [1, 86]) is a good one for $CoNb_2O_6$ past h_c^x.

6.6 Conclusions

To conclude, we have investigated the effects of integrability near the Ising QCP and evaluated how far away the features extend and how robust they are to additional interactions. We have shown that the bound state continuum should carry comparable spectral weight to the higher bound states. The microscopic 1D model of $CoNb_2O_6$ treated here is able to reproduce the experimental data far away from criticality well. When moved close to the QCP, the model still has the characteristics of the E_8 symmetry, with the mass ratios

following straight lines through the analytical values, even better than the extrapolated experimental data suggests. Future experiments with improved resolution on $CoNb_2O_6$ should detect higher bound state signatures to confirm the effects of integrability and the bound state continuum modeling confinement dynamics around the 1D QCP.

Acknowlegdments

The authors thank R. Coldea for very useful correspondence. This work was supported by a grant from the Army Research Office with funding from the DARPA OLE program and by the Knut and Alice Wallenberg foundation (J. K.).

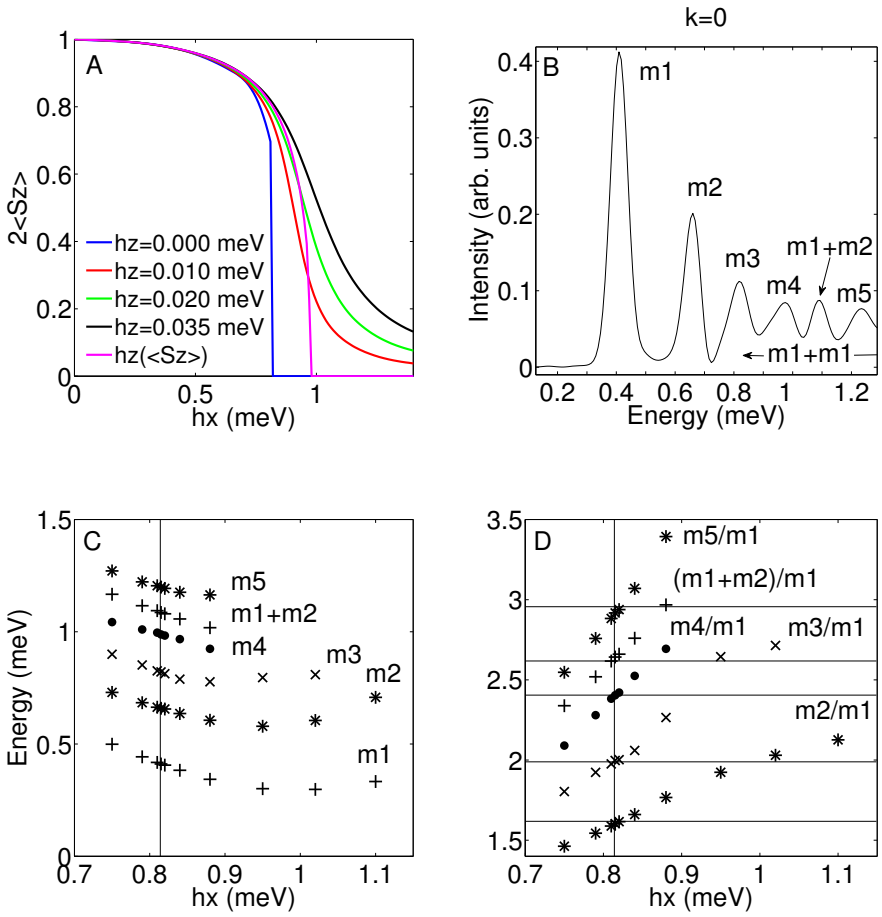

Figure 6.3: (Color online) The full Hamiltonian describing $CoNb_2O_6$. (A) Magnetization comparison between weakly coupled chains and chains in different constant longitudinal field. (B) The cross section of the dynamical structure function for h_c^x at zero momentum showing the masses of the first five bound states and two bound state pairs. (C) The bound state masses as a function of h^x. The minimum gap is above h_c^x and the bound state mass minimum decreases with increasing mass. (D) The ratio of the bound state masses varies linearly around h_c^x and goes through the analytically calculated values at h_c^x.

Chapter 7

Quantum phases for anisotropic XXZ-chains

7.1 Introduction

Quantum spin chains are a very exciting playground to study strongly correlated quantum systems. Many different types of phases and phase transition can be understood by studying relatively simple spin-chain model Hamiltonians. A prime example is the Heisenberg chain which has a gap above the ground state in the case of integer spins while the half-integer spin chains are gapless.[102, 103] Gapped integer spin chains do not break any symmetry and can thus not be characterized by any local order parameter. It has recently been shown that the spin-1 Heisenberg chain is a symmetry protected topological phase. This type of phase can be understood in terms of fractionalization of symmetry operations at the edges. In other words, the phases are characterized by projective representations of the symmetries present. Using this insight, it becomes clear that there is a fundamental difference between odd and even integer spin chains. In the case of of odd integer spin chains, the spin fractionalizes into two *half-integer* edge spins which are protected by the symmetry of the Hamiltonian. In the case of even integer, the fractionalized *integer* spins are not-protected.

Given the above reasoning, it is now interesting to discuss the phase diagram around the antiferromagnetic (AFM) Heisenberg point for increasing integer spins. Interestingly, bozonization predicts a similar phase diagram for all integer spin chains.[104] Another early proposal, contained a succession of intermediate phases corresponding to all the Haldane phases for lower spin chains.[105] On the other hand, early DMRG studies showed more or less a classical phase diagram for $S \geq 2$.[106]. A recent level spectroscopy (LS) study [107–110] show a phase diagram for $S = 2$ somewhere between the two previous proposals.

Apart from the large Hilbert space, the presence of the critical XY phase makes this a hard problem to understand. This phase has infinite correlation lengths, making it difficult to compute properties inside it and more importantly close to it. The transition into this phase is a Berzinski-Kosterlitz-Thouless (BKT) transition, which gets harder to locate the

slower the gap in the adjacent phase opens up.

In this chapter we present results of infinite system density-matrix-renormalization-group (iDMRG) calculations which allows us to capture the long correlation lengths. We study the phase diagram in detail and discuss the different phases we find in context of the previous results. Although the used iDMRG algorithm has been discussed in the literature before, we find it useful to give a pedagogical explanation of the algorithm and show how to implement $U(1)$ symmetries into the code.

This chapter is organized as follows: We first briefly present the model we are investigating and the challenges it contains in Sec. 7.2. In Sec. 7.3 we discuss the various phases and phase transitions present and how they can be detected with our data. In Sec. 7.4 we present our main result, the phase diagrams with focus on the two Haldane phases. In Sec. 7.5 we present some results for the $S = 3$ XXZ-chain to confirm the belief on the ceveelopment of the classical phase diagram. We conclude with a discussion in Sec. 7.6.

7.2 The model

The XXZ quantum spin chain was introduced in Ch. 1 in Eq. 1.33. We write down the Hamiltonian again here for convenience

$$H_{\mathrm{XXZ}} = \sum_n (S_n^x S_{n+1}^x + S_n^y S_{n+1}^y + \Delta S_n^z S_{n+1}^z), \tag{7.1}$$

where S_n^α ($\alpha = x, y, z$) is the α-component of the spin-S operator at the n^{th} site and Δ is the XXZ anisotropy parameter. As Δ is tuned from $-\infty$ to ∞, the following phases appear; Ferromagnetic (FM), XY, (Haldane) and AFM.[102, 103] The Haldane phase does not appear for half-integer spins including $S = \infty$. The transition from the FM to the XY phase occurs at the FM Heisenberg point $\Delta = -1$ for all S. The transition from XY to Haldane occurs at $\Delta = 0$ for $S = 1$ [111] and approaches rapidly the AFM Heisenberg point for larger integer spins. The same is true for the transition between the Haldane phase and the AFM phase that also approaches $\Delta = 1$ rapidly for increasing integer S, but from the opposite direction (transition at $\Delta = 1.19$ for $S = 1$). This makes it hard to resolve the Haldane phase already for $S = 2$, where the phase extends about $\delta\Delta \sim 0.04$. For all half-integer spins the XY to AFM transition is at the AFM Heisenberg point $\Delta = 1$ [102, 103].

With the addition of an on-site interaction, various local quantum states can be favored or disfavored. We will study the $S = 2$ Hamiltonian $H = H_{\mathrm{xxz}} + H_{\mathrm{D}}$, where the on-site interaction has the form

$$H_{\mathrm{D}} = \sum_n D_2 (S_n^z)^2 + D_4 (S_n^z)^4. \tag{7.2}$$

A general form for the on-site anisotropy in a spin-S chain is $\sum_{p=1}^{2S} D_p (S_n^z)^p$, where D_p are constants. The odd terms in p favors a FM phase and are hence not very interesting. The even p terms can give rise to interesting phases. The phase diagram (Δ,D_2) for $S = 1$ is very

well understood. Also the phase diagram for $S = 2$ with the $p = 2$ term has been extensively studied [106–108, 112]. However, these studies have presented some contradictory results. No previous work has taken the $p = 4$ term into account for a $S = 2$ chain.

The Haldane phases contain the AKLT point, which appear when the spins are projected into a valence bond solid ground state [113]. This state can be described in terms of $2S$ spin-1/2 at each site, forming S valence bonds with each of the two neighboring sites. Increasing D_2 from the AFM Heisenberg point in integer spin chains, a supposedly new phase appears, previously named the Large-D (LD) phase. This phase is unmagnetized and has $m_n = 0$ in the limit $D_2 \to \infty$. In $S \geq 2$ integer spin chains this phase is separated from the AFM Heisenberg point by the XY phase along the D_2 line, and hence initially believed to be a different phase. However, some recent work proposed that only two distinct Haldane phases exist using symmetry arguments [114]. All the even S Haldane (EH) phases are argued to be the same phase and all the odd S Haldane (OH) phases as well. They also pointed out the similarities between the EH phase and the LD phase [114]. In fact, the LD phase can be thought of as the spin-0 Haldane phase. The main results in this chapter is; with the D_4 term, the OH is easily accessible, extending to $D_4 \gtrsim 0$ for some (Δ,D_2) and the spin-2 Haldane phase is indeed adiabatically connected to LD phase, strengthening the claim of only two distinct Haldane phases; OH and EH.

7.3 Quantum phase transitions

Quantum phase transitions are transitions between various quantum phases. They occur at zero temperature when some physical parameter is varied. Spin chains are great systems to analyze various quantum phase transitions in. They can be analyzed with a wide variety of methods, ranging from analytical, like bosonization and conformal field theory (CFT), that can give exact solutions under certain conditions, to numerical like exact diagonlization, that also is exact but limited to small system sizes and iDMRG. Since iDMRG, does not give an exact solution, especially close to critically, care most be taken in interpreting the data. Various observables can be used. In this section, we will begin with a brief discussion of the phases present in our Hamiltonian $H_{\text{xxz}} + H_{\text{D}}$ and how they are classified. Then we consider the three different quantum phase transitions, first order, second order and BKT, that occur.

7.3.1 Quantum phases

Before we investigate the phase diagram, we summarize the characteristics of the different phases. The two magnetically ordered phases are easiest to distinguish. They have a non-zero magnetization site expectation value $|\langle S_n^z \rangle| \neq 0$, with the FM phase having a non-zero total magnetization $\langle S_n^z \rangle = \langle S_{n+1}^z \rangle$, while the AFM phase has zero total magnetization $\langle S_n^z \rangle = -\langle S_{n+1}^z \rangle$. All the other phases are unmagnetized $\langle S_n^z \rangle = 0$. The XY-phase is the only gapless phase, it has exponentially decaying $\langle S_m^z S_n^z \rangle$ correlations and power law decaying $\langle S_m^+ S_n^- \rangle$ correlations [106]. The hidden non-local order of the OH phase can be described

with a string order (SO) parameter,

$$SO(m,n) = \langle S^z_m e^{i\pi \sum_{p=m+1}^{n} S^z_p} S^z_n \rangle, \tag{7.3}$$

that approaches a finite value in the thermodynamic limit $n - m \to \infty$.

7.3.2 First order transition

The transition between the AFM and EH phases is a first order transition for large Δ, as expected in the limit $\Delta \to \infty$. In the $D_4 = 0$ plane it turns into a first order transition at $\Delta \approx 3.8$. This type of transition is easiest located by observing the change in the ground state energy slope as a function of the physical parameter across the transition, see Fig. 7.1(a). This comes from the crossing of two different energy levels that are continued with red dashed lined where it is not the ground state energy anymore. The energy is well converged as a function of χ. Both the entanglement entropy S and the correlation length ξ has a smooth behavior across this transition.

7.3.3 Second order transition

Closer to the AFM Heisenberg point ($\Delta \lesssim 3.8$) does the transition between the AFM and the EH phase turn into a second order phase transition. It is easy to locate the magnetized phase everywhere with its local order parameter, the local magnetization $|\langle S^z_n \rangle|$. It vanishes at the phase transition, see Fig. 7.1(b) for an example along the line $\Delta = 1$, where the transition is at $D_2^{c1}(\Delta = 1) = -0.004$. Characteristics of a second order phase transition are diverging entanglement entropy S and $S^z_m S^z_n$-correlation length ξ_0 from both side, see Fig. 7.1(c)-(d). The entanglement entropy in Fig. 7.1(c) has a distinguishable peak at $D_2^{c1}(\Delta = 1)$ for large enough χ. The peak in the ξ_0 correlation length in Fig. 7.1(d) is clearer, again at $D_2^{c1}(\Delta = 1)$ for large enough χ. Due to the narrowness of the EH phase $\delta D_2 \approx 0.05$, these observables of the transition can be hard to distinguish for small χ's.

7.3.4 BKT transition

The other transition in Fig. 7.1(b)-(d) is a BKT transition, to the critical phase. This is the hardest transition to locate and the one we have focused our efforts on. The entanglement entropy in this phase is infinite. However, finite matrices can only contain a finite amount of entanglement entropy $S \leq log(\chi)$. Moreover, even at criticality with DMRG the entanglement eigenvalue distribution does not maximize the entanglement. This makes it hard to see exactly where the transition is, see Fig. 7.1(c), where the entanglement entropy increases continuously across the phase transition to the critical phase. The correlation lengths, ξ_0 in Fig. 7.1(d) and ξ_2, the $S^+_m S^-_n$-correlation length, have similar behaviors and they are not very useful either for pin-pointing the transitIon.

A scaling from finite χ up to $\chi = \infty$ tend to overestimate the critical region, since the correlation lengths do not behave monotonically with χ. As long as χ is small enough, the

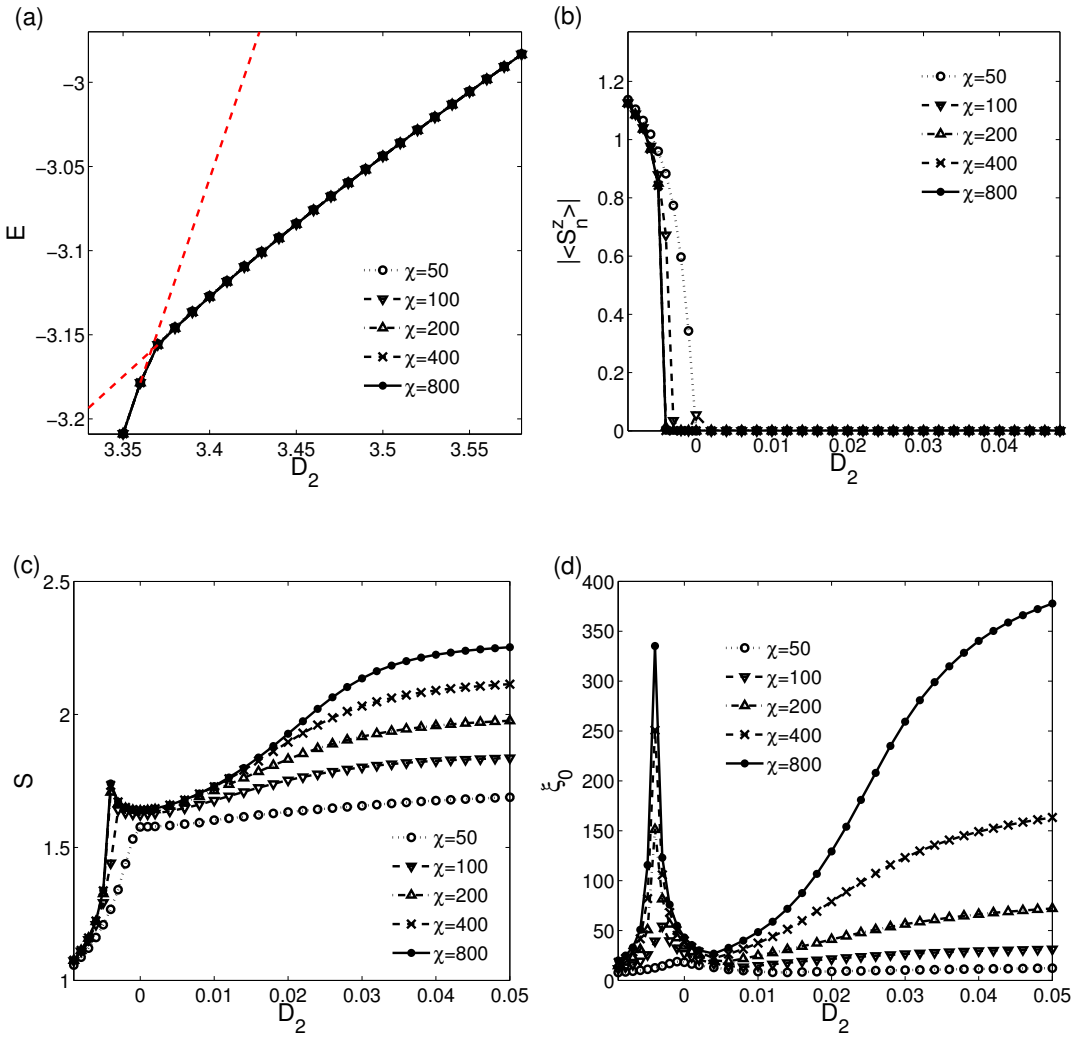

Figure 7.1: Examples of how to locate phase transitions with iDMRG data. (a) First order transition; Energy level crossing in the ground state. Red dashed line indicates the continuation of the energy level where it is not the ground state anymore. Note also that the energy is well converged in χ in iDMRG. (b)-(d) Second order transition. (b) Transition from a magnetized to a non-magnetized phase. (c)-(d) The entanglement entropy and correlation length go to infinity $S \to \infty$ and $\xi_0 \to \infty$ as $\chi \to \infty$ at the transition point. (c)-(d) BKT transition; Hard to locate in these diagrams. The critical phase is the region where the entanglement entropy and correlation length go to infinity $S \to \infty$ and $\xi_0 \to \infty$ as $\chi \to \infty$.

ground state is influenced by the critical region and scales similar as within it. However, once χ is large enough to describe the gapped phase, the physical properties converge fast. The same problem appeared when we tried scaling of other observables that have been used to locate a BKT transition, like closing of energy gap [106, 112] and fidelity susceptibility [115, 116]. The first one of these is similar to correlation scaling, since $\Delta E \propto 1/\xi$. The second has proven to be more accurate for some models, but we did not find any improvement for our model.

However, there is another method that can localize the BKT transition much better in this model. As was shown by Calabrese and Cardy [117], close to criticality in 1-D there is a relation between the entanglement entropy and the correlation length,

$$S = S_0 + \frac{c}{6} log(\xi), \tag{7.4}$$

where S_0 is a constant that varies over the phase diagram and c is the central charge. The value of the central charge is one in the XY-phase and zero outside. In our model, at finite χ, we find that $c = 1$ inside the critical phase and $c < 1$ outside the critical phase, already for small χ. For more details on the central charge calculation, see Sec. 7.3.5.

7.3.5 Central charge

The entanglement eigenvalue distribution at finite χ at criticality is similar to at infinite χ slightly away from criticality [118, 119]. Hence, at criticality, the relation Eq. 7.4 can be obtained by variation of χ and c is then obtained from the slope by a linear fit, see Fig 7.2.

Simulating to very high precession (truncation error $\leq 10^{-13}$), the data converges well outside the critical phase, making it possible to determine the slope to very high accuracy and hence where in the phase diagram it starts to deviate from 1/6. Outside the critical phase it deviates from 1/6 already for small χ and the deviation increase with increasing χ. Inside the critical phase, the data slightly fluctuates more. Hence, averaging over many data points is desirable. However, the error does not appear to be completely independent of χ, so we also want to use χ's far apart. We simulate for $\chi = 25, 35, 50, 70, 100, 140, 200, 280, 400, 560, 800, 1120$ and average for various subsections of these, see Fig. 7.2(b). Note, that the transition to the critical phase with this method does not appear to scale much with χ. The noise in the data is almost as big as the difference in transition between the lowest and highest χ's. This makes it hard to do scaling, but on the other hand it is not really necessary when the data is almost converged. Also the noise decrease with increasing χ and we mainly use the largest χ's to determine the transition point. However, we plot some lower χ data as well mainly to show how well the data is converged and how noisy it is.

The transition to the XY phase close to the AFM Heisenberg point, shown in Fig. 7.2(b)-(d) is with this method $D_2^{c2}(\Delta = 1) \approx 0.044$, see Fig. 7.2(b), where these averages almost converge and reaches $c = 1$ for the largest χ. This in very good agreement with LS+ED study which has the transition at $D_2^{c2}(\Delta = 1) = 0.043$, scaled from finite chains up to 12

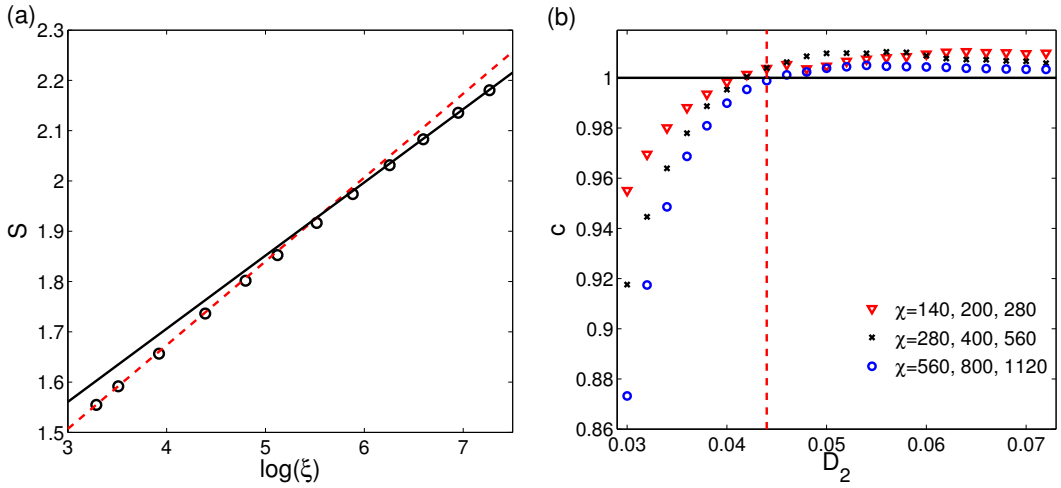

Figure 7.2: (a) S as a function of $log(\xi)$ for $\chi = 25, 35, 50, 70, 100, 140, 200, 280, 400, 560, 800, 1120$, black circles. Close to a QCP there is a linear relation between them, red dashed line. The system moves away from criticality with increasing χ. A linear fit to the data from the three largest χ gives a different slope, black line. (b) Linear fit of the data at three different χ to the Eq. 7.4. The red dashed line shows the transition to the critical phase with $c = 1$.

sites [107]. The data inside the critical phase appears surprisingly to initially overshoot $c = 1$ slightly. On the other side of the critical phase, the transition is not as ditinct. As an example, we find the transition at $(\Delta = 0, D_4 = 0)$ to be at $D_2^{c3}(\Delta = 0) \approx 2.82$(not shown). This is in good agreement with the best LS+DMRG data $D_2^{c3}(\Delta = 0) = 2.796$ [108].

With the data presented in this way in Fig. 7.2(b) it is hard to see what c is outside the critical phase as $\chi \to \infty$, but that is not very interesting anyway. Well outside the critical phase it is clear that this data has very little noise as c gets smaller the larger $log\ \chi$ is. Closer to the transition it starts to get more noisy and surprisingly appears to initially go slightly past 1. Further inside the critical phase does it approach 1. The reason for this initial overshoot is unclear, but we believe it occurs in the less understood critical phase and we take the initial crossing of 1 as our phase transition point.

The LS method scales much better at this transition then any of the other methods that use scaling, that is the transition point does not change very much with system size. Tzeng uses DMRG to calculate the energy spectrum and goes to very high χ so he can neglect the scaling in χ and only have to scale in system size. At this transition point he calculate systems up to 60 sites.

7.4 Phase diagrams

The $S = 2$ phase diagram as a function of J_z and D_2 (at $D_4 = 0$) has previously been studied, however as we already have mentioned there have been disagreements [106, 107]. The two most debated issues are whether there exist an OH phase for the spin-2 system and whether the Hesienberg point and the phase at large D_2 belong to the same phase, the EH phase.

7.4.1 Phase Diagram (Δ,D_2)

In this section we investigate the upper right corner ($\Delta \geq 0$,$D_2 \geq 0$) of the $D_4 = 0$ phase diagram focusing on these two issues. The three large color coded phases in Fig. 7.3 shows our result for the (Δ,D_2) phase diagram. The transition to the AFM phase is easy to locate from the local magnetic order parameter $|\langle S_n^z \rangle|$, for an example see Fig. 7.1(a). The hardest phase transition to locate is the BKT transition. We located it by calculating the central charge c up to at least $\chi = 1120$ states per site in infinite chains, see Sec. 7.3 for details. At some interesting points we also used $\chi = 1600$ and $\chi = 2240$. No sign of the OH was seen in any of the points analyzed in this phase diagram. Previous DMRG results for the transition to the XY phase is shown with a red dashed line [106]. Recent LS+ED result for the BKT transition is shown with the red line and for the OH phase with the tiny blue region [107]. The new LS+DMRG results, that appeared when this chapter was being finalized, conclude that the OH phase is even smaller, but still existing [108].

Our results are a big improvement from the old DMRG results [106] in the upper right corner. However, as can be seen in Fig. 7.4, where c has been calculated along the lines $\Delta = 2.3, 2.6, 3.3, 4.0$ (other lines not shown) in Fig. 7.3, it is really hard to determine exactly where the phase transition is in this part of the phase diagram. The simulation time for a given χ is longest here and the data noisier than anywhere else. The correlation length is huge, likely tens of thousands of sites, although it gets even larger for smaller Δ along the upper part of the critical phase. Again, the critical phase is where $c = 1$ for an extended region.

It is clear that the critical region is much smaller here than concluded in the earlier DMRG study by Aschauer et. al. [106]. Simulating to larger χ, a smaller XY-phase can not be excluded, but lit is likely larger than concluded in the recent LS studies [107, 108]. Regardless, it is definitely small enough that no direct transition from the XY to the AFM phase occur in this part of the phase diagram. In Sec. 7.4.4 we will argue in more detail that the AFM Heisenberg point and the a point at large D_2 belongs to the same phase and in Sec. 7.4.3 we will show that the OH phase does not appear in this phase diagram.

7.4.2 Phase digram (D_2,D_4)

Even if we can not determine, whether the OH phase exist in the $D_4 = 0$ phase diagram, it should be much easier to determine whether it exists with other anisotropic on-site inter-

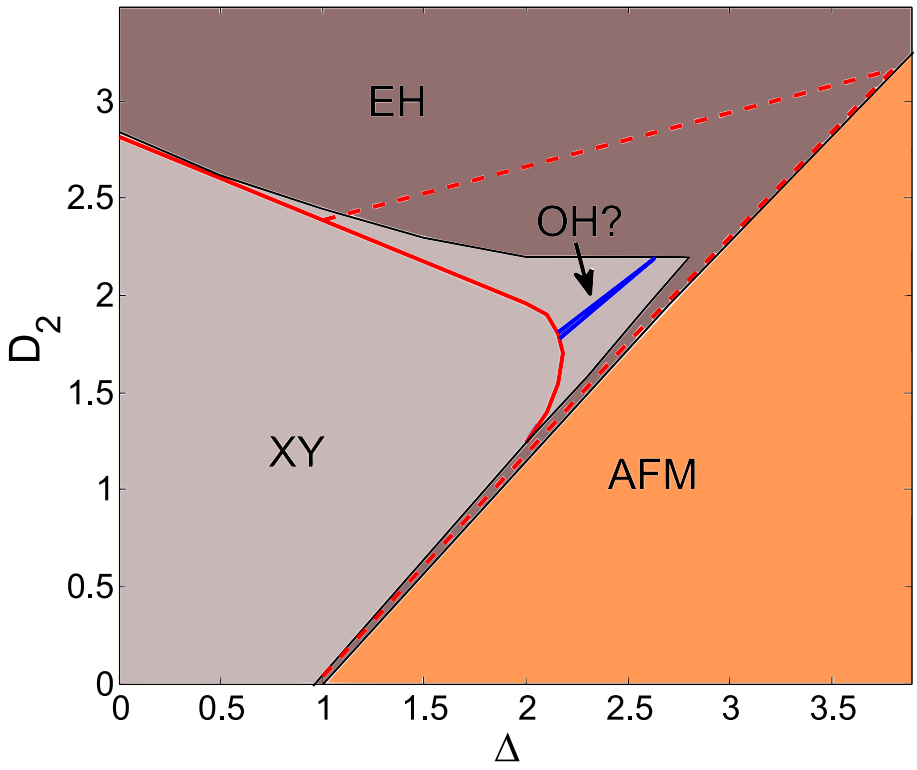

Figure 7.3: Phase diagram for $S = 2$ as a function of Δ and on-site anisotropy D_2. The phases detected with iDMRG are the large colored regions; AFM, XY and EH phases. Red dashed line show the previous calculated XY phase boundary with DMRG [106]. Solid red line, the calculated XY phase boundary with ED+LS [107]. Solid blue line, the calculated Oh phase boundary with ED+LS [107].

actions. The AFM Heisenberg point in the spin-1 chain belongs to the OH phase. In this case the possible onsite states are $m_z = 0, \pm 1$, so starting from the spin-2 AFM Heisenberg point and projecting out the $m_z = \pm 2$ onsite states should give an OH phase. This is done by taking $D_2 = -D_4$, as $D_4 \to \infty$. This does not favor any of the $m_z = 0, \pm 1$ states over the other. The phase diagram around the AFM Heisenberg point for various on-site anisotropies D_2 and D_4 are shown in Fig. 7.5. This phase diagram is simulated with $\chi \leq 400$ and the phase transitions are slightly less accurate than for the (Δ,D_2)-phase diagram. The OH phase is the ground state for a wide range of on-site anisotropies and it appears roughly where it was expected, along lines $D_2 = -D_4 + D_2^{S=1}$, where $D_2^{S=1}$ is the values where the OH phase appears at $\Delta = 1$ in the $S = 1$ phase diagram. As $D_4 \to \infty$ the $S = 1$ phase diagram for $\Delta = 1$ translated by $-D_4$ indeed appears (not shown).

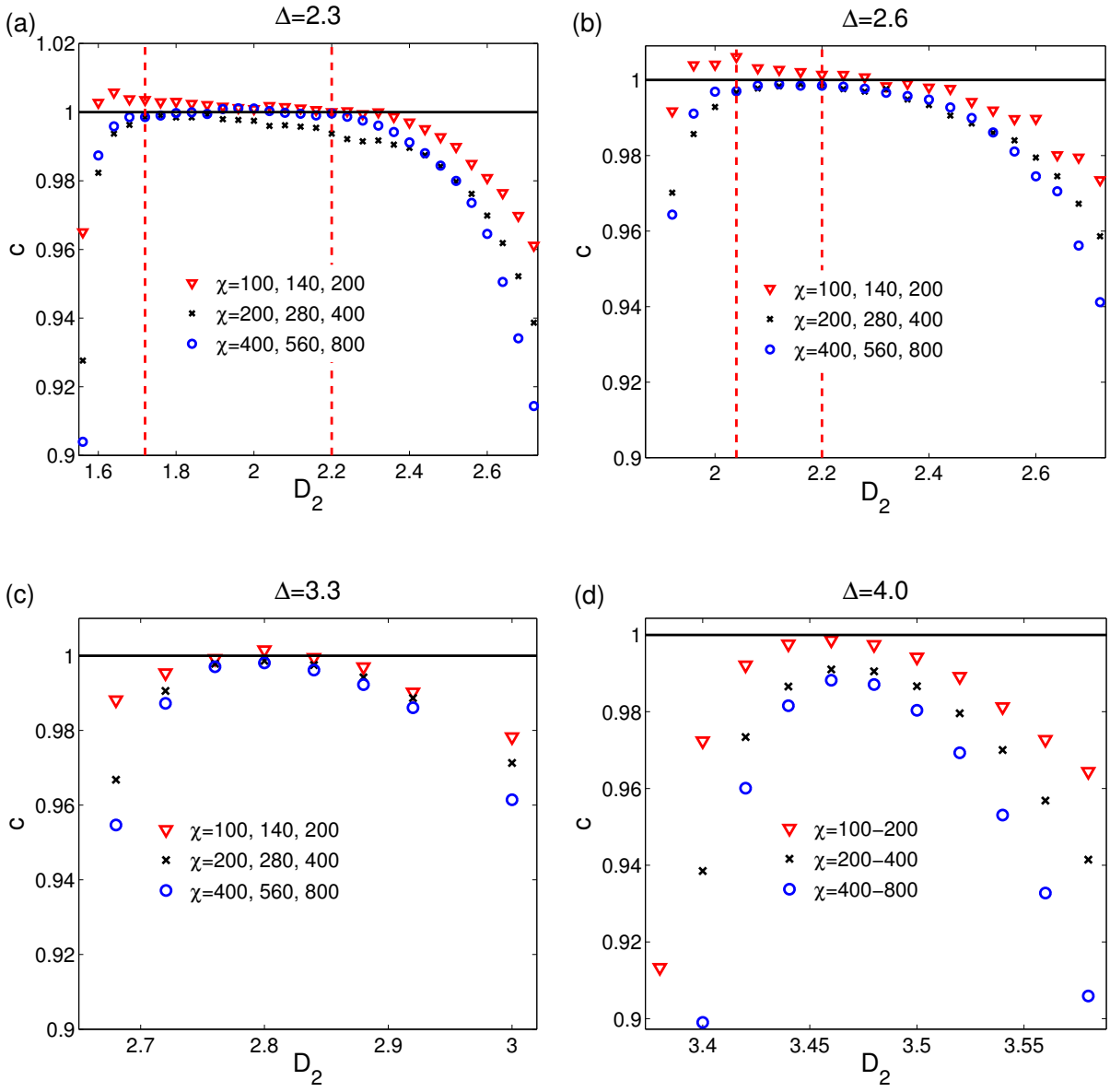

Figure 7.4: Central charge calculations to find the critical phase as in Fig. 7.2, along different vertical lines in the phase diagram Fig. 7.3. The critical phase is where $c = 1$ extends over a finite range, like in (a) and likely (b), marked with vertical red dashed lines.

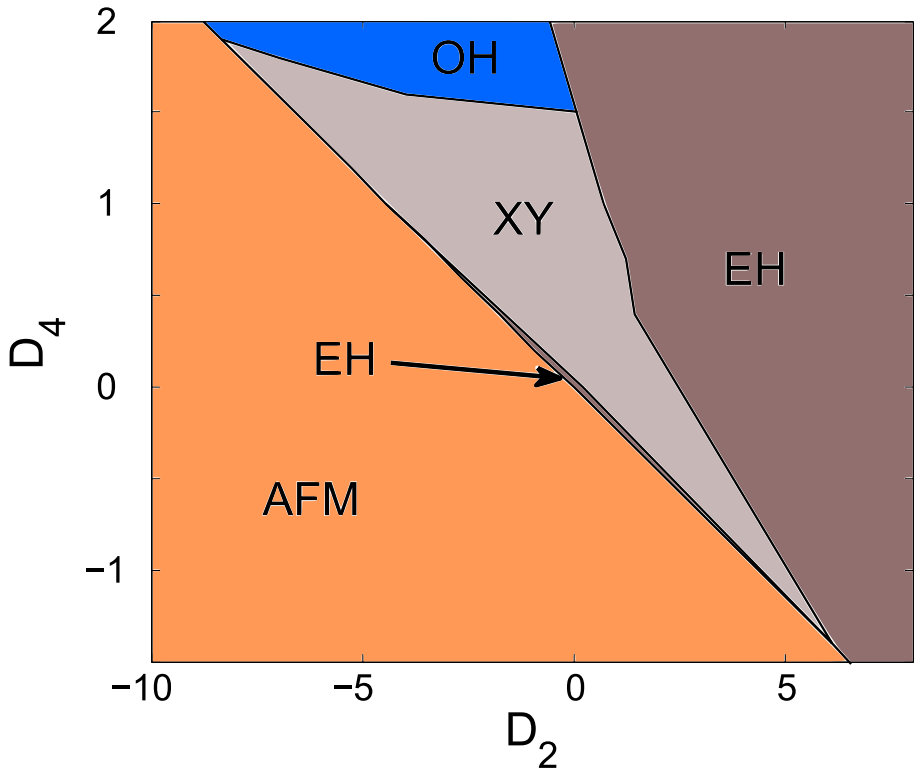

Figure 7.5: Phase diagram for $S = 2$ as a function of the on-site anisotropies D_2 and D_4 at $\Delta = 1$. The phases detected with iDMRG are the colored regions; AFM, XY, EH and OH phases.

7.4.3 Odd Haldane phase

It was already established in Sec. 7.4.2 that an OH phase exist in the $S = 2$ XXZ-chain with on-site anisotropic interactions. However, no sign of the OH phase was seen in the $D_4 = 0$ phase diagram. In this subsection we will investigate how close to this phase diagram it exist. Tonegawa et. al. [107] found a very small and narrow OH phase in this phase diagram, for example the point ($\Delta = 2.6$,$D_2 = 2.155$) is proposed to be inside this phase and about as far away from the critical phase as possible. Starting from this point and going along the line

$$D_2 = -D_4 + 2.155 \tag{7.5}$$

for increasing D_4, it is obvious that the phase is a OH phase. Well inside the phase, the entanglement entropy and the correlation lengths are well converged as a function of χ and the SO is non-zero and the entanglement spectra is two-fold degenerate. As long as χ is smaller than the correlation length ξ_2, the string order decrease roughly linearly with $1/\chi$. Once χ is large enough to describe the phase accurately, the correct SO can be obtained. For

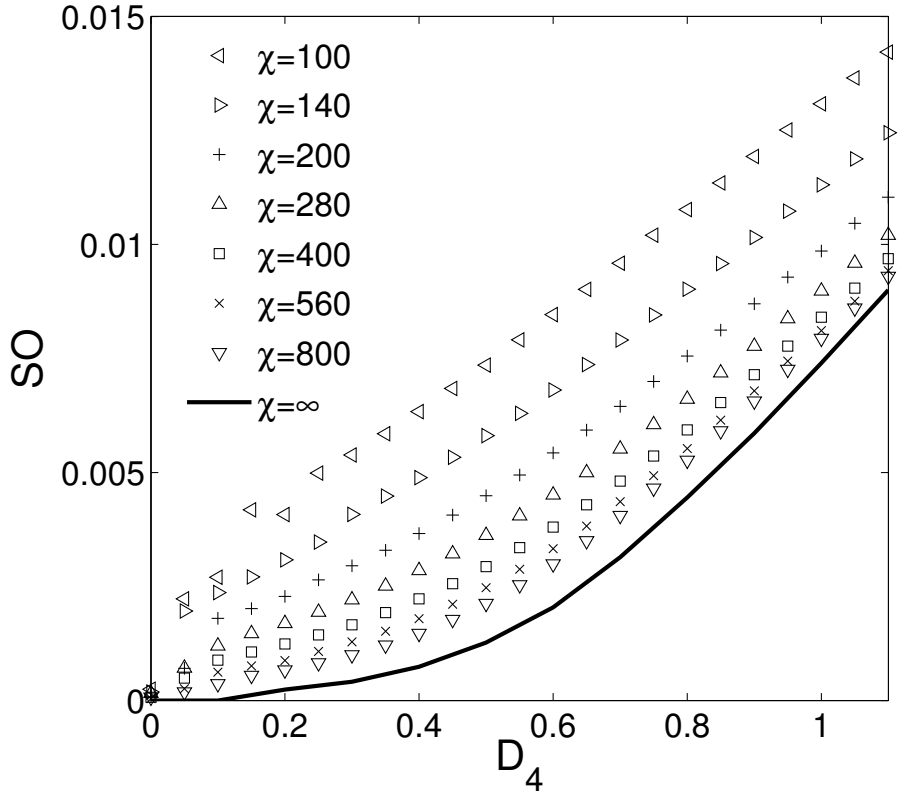

Figure 7.6: String order calculations for different χ's and scaled to $\chi \to \infty$ (solid line) along the line (Eq. 7.5). Smaller χ gives a larger SO. The SO vanish at $D_4 \approx= 0.1$. At $D_4 = 0$ it has vanished for all χ's.

the lower D_4 this happens for larger and larger χ as criticality is approached, but a scaling in χ is still expected to give a reasonable result.

Fig. 7.6 shows the SO for various χs and scaled to $\chi = \infty$ as a function of D_4 along this line. Central charge calculations give a similar transition point into a critical phase, just outside the $D_4 = 0$ plane. The SO approaches zero exponentially as the BKT transition is approached in a similar fashion as in the $S = 1$ phase diagram. The scaling appears to overestimate the value of the SO slightly close to the transition. Also based from experience with the OH phase in a $S = 1$ system, we know that a finite χ overestimate the size of the OH phase. In Fig. 7.6 the SO$= 0$ for all χ simulated at $D_4 = 0$ and this point should hence be clearly outside the OH phase.

We did simulations for many lines out from the $D_4 = 0$ plane around the line $D_2 = -D_4 + 2.155$ at $\Delta = 2.6$, but none are significantly closer to the OH phase. The region the

OH phase was proposed to occupy by Tonegawa et. al. is close to the OH phase, as are points for higher Δ along an extension of that region, close to the AFM phase. These points coincide with the points with largest c in Fig. 7.4(c)-(d) and the proximity to the transition into the OH phase, which also has a central charge $c = 1$, is likely the reason why $c \approx 1$ there.

7.4.4 Even Haldane phase

The (Δ,D_2) phase diagram at $D_4 = 0$ in Fig. 7.3 has the AFM Heisenberg point and a point at large D_2 in the same EH phase. In this subsection we will discuss our data in more detail and explain why it is possible to move adiabatically between these two points without going through a phase transition. We made similar simulations as in Fig. 7.1(b)-(d) along lines out from the AFM phase as a function of D_2 for fixed $\Delta = 1.0 : 0.1 : 4.0$, all having the same characteristics up to the change in phase transition from second to first order at $\Delta \approx 3.8$. The bottom of the ξ_0 valley, see Fig. 7.1(d) for an example, is well converged in χ and roughly constant for all these lines up to the change in phase transition type, showing no sign of a transition into the critical phase.

However, the correlation length remains much larger than what is possible to reach with numerics outside the valley on the opposite side from the AFM phase well passed the change in phase transition type. The influence of the critical phase and more importantly the proximity to the transition to the OH phase at small D_4 s what has previously made it so hard to locate how far the XY phase extends. A phase transition with $c = 1$ between a phase around the AFM Heisenberg point and a trivial phase extending to large D_2 is hard to completely exclude from our data. For really large $\Delta \gtrsim 3.8$ it is obvious that there is no transition with $c = 1$ along D_2 lines. The simulations converge faster and the data is also less noisy than for lower values of Δ in Fig. 7.4(a). Also c is clearly below 1 and decrease faster with χ, about as fast as for comparable points (same c value for a given χ) just outside the XY phase in Fig. 7.4(a)-(b) and Fig. 7.2(b). A phase transition that ends where the transition out of the AFM phase change from 2^{nd} to 1^{st} order could also be a possible. However, on closer examination, although the valley discussed above where the correlation length is converged in numerical reachable *chi*s is gone, $c << 1$ in a small region close to the AFM phase all the way past the change in transition type. From these results and symmetry argument between the phases at the AFM Heisenberg point and a point at large D_2 we conclude that they are in the same phase, the EH phase.

From the (D_2,D_4) phase diagram at $\Delta = 1$ in Fig. 7.5 it also looks possible to move adiabatically from the AFM Heisenberg point to a large D_2 point in this phase diagram without closing the gap. At $D_2 \to \infty$, the EH phase has $m_n^z = 0$. Projecting out the $m_z = \pm 1, \pm 2$ states from the AFM Heisenberg point could give a EH phase. These are projected out equally for $D_4 = -1/4D_2$ as $D_2 \to \infty$. Consequently, it appears likely that the line $D_4 = -1/4D_2$ from the AFM Heisenberg point for increasing D_2 will stay in the EH phase. This line follow close to the AFM transition. Again there is a narrow EH phase that has a second order transition to the AFM phase. The valley in ξ_0 extends to

about $D_4 \approx -1.0$. However, the critical phase extends further to $D_4 \approx -1.4$. Without a narrow phase with a comparable short correlation length between the two phase transitions, a solid conclusion is hard to make. Central charge calculations in this area indicate a direct transition between the AFM and the XY phase here.

7.5 $S = 3$ XXZ-chain

We conclude this chapter with investigating a related problem, the $S = 3$ XXZ-chain. We compare the results to the $S = 1, 2$ cases and discuss the implications in the development of the classical limit $S \to \infty$. In 1983 Haldane conjunctured that the AFM Hesienberg point for all even S belonged to a gapped phase between the XY and the AFM phase and showed that the gap at this point had the asymptotic expansion $\delta E_S \approx S^2 e^{-\pi S}$ as $S \to \infty$ [102, 103].

The $S = 1, 2$ chains have been extensively studied and agree with Haldanes conjuncture, although the actual values needs to be calculated numerically. The value of the spin wave velocity $c = \delta E_s \xi = 2S$ as $S \to \infty$ relates the correlation length and the gap. The correlation length increases rapidly from $\xi_0^{S=1} = 5.828(1)$ to $\xi_0^{S=2} = 47.2(1)$, however it is a bit slower than the asymptotic expansion suggests. Moreover, with the differences between the EH and OH phases, a different approach of the $S \to \infty$ limit for odd and even integer spin chains can not be excluded. The expected long correlation length will make the simulations challenging, but the possible shrinking of the OH will likely make it even more so.

Indeed simulating at the AFM Heisenberg point for $S = 3$, the OH phase appears first for $\chi \gtrsim 800$. That the AFM phase extends further into the Haldane phase the smaller the χ used is, have also been observed for $S = 1, 2$, see Fig. 7.1(b) for a related $S = 2$ example. Locating this transition for various $\chi \leq 1120$, we can do a finite χ scaling, see Fig. 7.7(a), where we see a transition at $\Delta^{S=3} = 1.000045(5)$. Consequently, this transition approaches $\Delta_{c2-3}^{S=\infty} = 1$ exponentially, but faster than the gap closes at $S \to \infty$, since $\Delta_{c3}^{S=1} = 1.19(1)$ and $\Delta_{c3}^{S=2} = 1.005(1)$.

The transition from the XY phase to the Haldane is from the $S = 1, 2$ cases expected to be slightly further away from the AFM Heisenberg point and not to change as much with χ. Still, $\chi \gtrsim 400$ is required to see the OH phase clearly. Fig. 7.7(b) shows the correlation for $\chi = 400, 560, 800, 1120$ across these two transitions. The peak from the 2$^{\text{nd}}$-order transition between the OH and the AFM phase is where the local magnetization $| < S_n^z > |$ disappears. The transition between the AFM and the OH phase is harder to see, in fact it is not even clear there is a gapped OH phase from this graph. However, calculating the central charge, see Fig. 7.7(c), we see a clear transition at $\Delta_{c2}^{S=3} = 0.99970(5)$. Exactly as for $S = 2$ we see an initial overshoot of $c = 1$, although it is larger for $S = 3$, just inside the critical phase and approaching $c = 1$ (not shown) further into the phase. This transition also approaches $\Delta_{c2-3}^{S=\infty} = 1$ exponentially, but faster than the gap closing would suggest, since $\Delta_{c2}^{S=1} = 0.0$ and $\Delta_{c2}^{S=2} = 0.962(1)$. To calculate the SO in the thermodynamic limit at the AFM Heisenberg point we need to scale from the data inside the OH phase ($\chi \gtrsim 800$), see Fig. 7.7(d), where $\chi = 800, 1120, 1340, 1600$ are used in the finite-χ scaling to get $\text{SO}_{\Delta=1}^{S=3} = 0.161(1)$. The SO

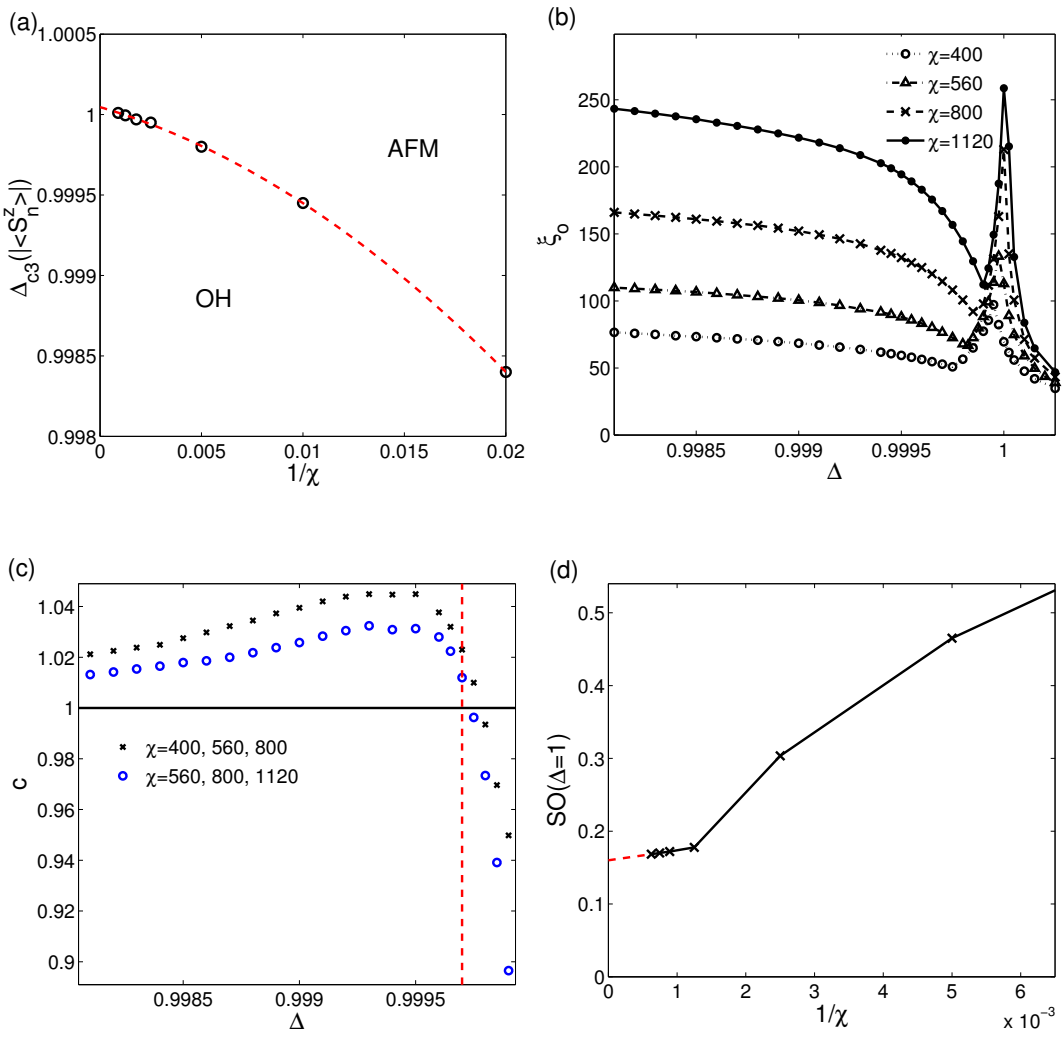

Figure 7.7: Phase transitions in the $S = 3$ XXZ-chain. (a) The vanishing of the magnetization order parameter $|\langle S_n^z \rangle|$ as a function of $1/\chi$, black circles and scaled to the limit $\chi \to \infty$, red dashed line. (b) The peak in the correlation length ξ_0 indicated the transition between the FM and the OH phase. (c) Central charge calculations gives the transition to the critical phase, red dashed line. (d) String order calculations at the AFM Heisenberg point. For small χ it is in the AFM phase, for $\chi \gtrsim 800$ it is in the OH phase and it scales linear with χ, red dashed line.

inside the AFM phase falls off in similar fashion as $|<S_n^z>|$ as can be seen for $\chi \lesssim 800$. Inside the OH phase does the SO fall off exponentially with Δ as the XY transition is approached, in a similar fashion as for $S = 1, 2$ and vanishes at $\Delta^{S=3} = 0.99965(5)$. Again it appears like the SO slightly overestimate the size of the OH phase when $\chi \to \infty$.

We also calculate the correlation length $\xi_0^{S=3} = 520(5)$ at the AFM Heisenberg point with a finite-χ scaling (not shown). Also the correlation length increases exponentially, but slower than what it will in the semi-classical limit. We conclude that there is no difference in how the EH and OH phases at the AFM Heisenberg point approaches the classical limit $\to \infty$.

7.6 Discussion

Of the many different methods used to locate the BKT transition, like vanishing energy gap, fidelity susceptibility, central charge calculation and level spectroscopy, the last two converge much faster in χ respectively system size than the others. Along most of the transition line they also agree well on the location of the transition. However, in the upper right corner of $D_4 = 0$ phase diagram, where the OH is proposed to be close to the XY phase, there are some disagreements. The central charge calculations are noisiest inside the XY phase close to a BKT transition and this region is largest in this corner. We argued in Sec. 7.3.5 that this region belongs to the critical phase.

Also scaling with the LS method can have some problems as pointed out by Tzeng [108], since the location of the transition can behave non-monotonically with system size. Even when the location of the transition appears well converged, like in Fig. 5(a) in Tzeng's [108] paper, $\max(\Delta E)$ appear not to be. In fact $\max(\Delta E)$ might even reach negative values for large systems, that is no OH phase along this line either, opening up for an even smaller (or maybe vanishing) OH phase than proposed by Tzeng.

The value of the SO increase with decreasing χ and the calculations of the SO from well inside the OH phase suggest that it does not extend all the way to the $D_4 = 0$ plane. From the $S = 1$ chain, we know that signs of the OH phase appear to extend into the XY phase for finite χ, but for $S = 2$ at $D_4 = 0$, non of these signs can be seen for finite χ, indicating that the $D_4 = 0$ plane is well outside the OH phase. The final conclusion whether the OH phase exist at $D_4 = 0$ will be left for future studies that can simulate larger systems. The correlation length is likely tens of thousands of site in this region so it might take some years before a definite conclusion can be made. Regardless, it will be a tiny area of the phase diagram and will likely of little use. However, with a D_4 interaction the OH phase is easily reachable.

We finish, by mention a recent study [120] on a related model, which showed that the OH phase also appear in a spin-2 chain if one starts from the SO(5) symmetric point, obtained by tuning J_D when $H = \sum_n \sum_{p=2}^4 J_p(\vec{S_n}\vec{S_{n+1}})^p$ is added to the Hamiltonian at $J_z = 1$ and $D_4 = 0$.

Acknowlegdments

The authors acknowledge helpful conversations with Masaki Oshikawa.

Bibliography

[1] R. Coldea, D. A. Tennant, E. M. Wheeler, E. Wawrzynska, D. Prabhakaran, M. Telling, K. Habicht, P. Smeibidl, and K. Kiefer, "Quantum Criticality in an Ising Chain: Experimental Evidence for Emergent E_8 Symmetry," Science **327**, 177–180 (2010).

[2] John D. Jackson, *Classical Electrodynamics Third Edition*, 3rd ed. (Wiley, 1998).

[3] Charles Kittel, *Introduction to Solid State Physics*, 8th ed. (Wiley, NY, 2005).

[4] Michael P. Marder, *Condensed Matter Physics* (Wiley-Interscience, 2000).

[5] J. J. Sakurai, *Modern Quantum Mechanics (Revised Edition)*, 1st ed. (Addison Wesley, 1993).

[6] Assa Auerbach, *Interacting Electrons and Quantum Magnetism (Graduate Texts in Contemporary Physics)* (Springer-Verlag New York Inc., 1998).

[7] Subir Sachdev, *Quantum Phase Transitions*, new edition ed. (Cambridge University Press, 2001).

[8] P. M. Chaikin and T. C. Lubensky, *Principles of Condensed Matter Physics*, reprint ed. (Cambridge University Press, 2000).

[9] Xiao-Gang Wen, *Quantum Field Theory of Many-body Systems: From the Origin of Sound to an Origin of Light and Electrons (Oxford Graduate Texts)*, reissue ed. (Oxford University Press, USA, 2007).

[10] Douglas R. Hofstadter, "Energy levels and wave functions of Bloch electrons in rational and irrational magnetic fields," Phys. Rev. B **14**, 2239–2249 (1976).

[11] K. von Klitzing, G. Dorda, and M. Pepper, "New Method for High-Accuracy Determination of the Fine-Structure Constant Based on Quantized Hall Resistance," Phys. Rev. Lett. **45**, 494–497 (1980).

[12] Klaus von Klitzing, "The quantized Hall effect," Reviews of Modern Physics **58**, 519–531 (1986).

[13] D. C. Tsui, H. L. Stormer, and A. C. Gossard, "Two-Dimensional Magnetotransport in the Extreme Quantum Limit," Phys. Rev. Lett. **48**, 1559–1562 (1982).

[14] Anders S. Sørensen, Eugene Demler, and Mikhail D. Lukin, "Fractional Quantum Hall States of Atoms in Optical Lattices," Phys. Rev. Lett. **94**, 086803 (2005).

[15] M. H. Anderson, J. R. Ensher, M. R. Matthews, C. E. Wieman, and E. A. Cornell, "Observation of Bose-Einstein Condensation in a Dilute Atomic Vapor," Science **269**, 198–201 (1995).

[16] K. B. Davis, M. O. Mewes, M. R. Andrews, N. J. van Druten, D. S. Durfee, D. M. Kurn, and W. Ketterle, "Bose-Einstein Condensation in a Gas of Sodium Atoms," Phys. Rev. Lett. **75**, 3969–3973 (1995).

[17] James M. Higbie, *First Steps toward Precision Measurements using Multicomponent Bose-Einstein Condensates of 87 Rb (Ph. D. dissertation)* (University of California, Berkeley, 2005).

[18] Lorraine E. Sadler, *Dynamics of a Spin 1 Ferromagnetic Condensate (Ph. D. dissertation)* (University of California, Berkeley, 2006).

[19] Sabrina R. A. Leslie, *Spinor Condensates as Amplifiers, Sensors and Tunable Quantum Playgrounds for Studies of Spin (Ph. D. dissertation)* (University of California, Berkeley, 2005).

[20] Immanuel Bloch, Jean Dalibard, and Wilhelm Zwerger, "Many-body physics with ultracold gases," Rev. Mod. Phys. **80**, 885–964 (2008).

[21] D. M. Stamper-Kurn and M. Ueda, "Spinor Bose gases: Explorations of symmetries, magnetism and quantum dynamics," arXiv:1205.1888v1 .

[22] N.R. Cooper, "Rapidly rotating atomic gases," Advances in Physics **57**, 539–616 (2008).

[23] Tapan Chatterji (Editor), *Neutron scattering from magnetic materials* (Elsevier B. V., 2006).

[24] Jonas A. Kjäll, Andrew M. Essin, and Joel E. Moore, "Magnetic phase diagram of a spin-1 condensate in two dimensions with dipole interaction," Phys. Rev. B **80**, 224502 (2009).

[25] Jonas A. Kjäll and Joel E. Moore, "Edge excitations of bosonic fractional quantum Hall phases in optical lattices," Phys. Rev. B **85**, 235137 (2012).

[26] Jonas A. Kjäll, Frank Pollmann, and Joel E. Moore, "Bound states and E_8 symmetry effects in perturbed quantum Ising chains," Phys. Rev. B **83**, 020407 (2011).

[27] Nicholas Metropolis, Arianna W. Rosenbluth, Marshall N. Rosenbluth, Augusta H. Teller, and Edward Teller, "Equation of State Calculations by Fast Computing Machines," J. Chem. Phys. **21**, 1087 (1953).

[28] Steven R. White, "Density-matrix algorithms for quantum renormalization groups," Phys. Rev. B **48**, 10345–10356 (1993).

[29] Guifré Vidal, "Efficient Classical Simulation of Slightly Entangled Quantum Computations," Phys. Rev. Lett. **91**, 147902 (2003).

[30] G. Vidal, "Classical Simulation of Infinite-Size Quantum Lattice Systems in One Spatial Dimension," Phys. Rev. Lett. **98**, 070201 (2007).

[31] Stellan Östlund and Stefan Rommer, "Thermodynamic Limit of Density Matrix Renormalization," Phys. Rev. Lett. **75**, 3537–3540 (1995).

[32] J. Dukelsky, M. A. Martn-Delgado, T. Nishino, and G. Sierra, "Equivalence of the variational matrix product method and the density matrix renormalization group applied to spin chains," EPL (Europhysics Letters) **43**, 457 (1998).

[33] Ulrich Schollwöck, "The density-matrix renormalization group in the age of matrix product states," Annals of Physics **326**, 96 – 192 (2011).

[34] D. Perez-Garcia, F. Verstraete, M. M. Wolf, and J. I. Cirac, "Matrix Product State Representations," Quantum Inf. Comput. **7**, 401 (2007), arXiv:quant-ph/0608197v2 .

[35] L.E. Sadler, J.M. Higbie, S. R. Leslie, M. Vengalattore, and D. M. Stamper-Kurn, "Spontaneous symmetry breaking in a quenched ferromagnetic spinor Bose-Einstein condensate," Nature **443**, 312–315 (2006).

[36] M. Vengalattore, S. R. Leslie, J. Guzman, and D. M. Stamper-Kurn, "Spontaneously Modulated Spin Textures in a Dipolar Spinor Bose-Einstein Condensate," Phys. Rev. Lett. **100**, 170403 (2008).

[37] M. Vengalattore, J. Guzman, S. Leslie, F. Serwane, and D. M. Stamper-Kurn, "Crystalline Magnetic Order in a Dipolar Quantum Fluid," arXiv:0901.3800 .

[38] E. Kim and M. H. V. Chan, "Probable observation of a supersolid helium phase," Nature **427**, 225 (2004).

[39] R. W. Cherng and E. Demler, "Magnetoroton Softening in Rb Spinor Condensates with Dipolar Interactions," Phys. Rev. Lett. **103**, 185301 (2009).

[40] Austen Lamacraft, "Long-wavelength spin dynamics of ferromagnetic condensates," Phys. Rev. A **77**, 063622 (2008).

[41] Jay D. Sau, S. R. Leslie, D. M. Stamper-Kurn, and Marvin L. Cohen, "Theory of domain formation in inhomogeneous ferromagnetic dipolar condensates within the truncated Wigner approximation," Phys. Rev. A **80**, 023622 (2009).

[42] Tin-Lun Ho, "Spinor Bose Condensates in Optical Traps," Phys. Rev. Lett. **81**, 742–745 (1998).

[43] Tetsuo Ohmi and Kazushige Machida, "Bose-Einstein Condensation with Internal Degrees of Freedom in Alkali Atom Gases," Journal of the Physical Society of Japan **67**, 1822–1825 (1998).

[44] Subroto Mukerjee, Cenke Xu, and J. E. Moore, "Dynamical models and the phase ordering kinetics of the $s = 1$ spinor condensate," Phys. Rev. B **76**, 104519 (2007).

[45] Daniel Podolsky, Shailesh Chandrasekharan, and Ashvin Vishwanath, "Phase transitions of $S = 1$ spinor condensates in an optical lattice," Phys. Rev. B **80**, 214513 (2009).

[46] E. G. M. van Kempen, S. J. J. M. F. Kokkelmans, D. J. Heinzen, and B. J. Verhaar, "Interisotope Determination of Ultracold Rubidium Interactions from Three High-Precision Experiments," Phys. Rev. Lett. **88**, 093201 (2002).

[47] Discussion with D. M. Stamper-Kurns experimental group at Berkeley.

[48] Axel Griesmaier, Jörg Werner, Sven Hensler, Jürgen Stuhler, and Tilman Pfau, "Bose-Einstein Condensation of Chromium," Phys. Rev. Lett. **94**, 160401 (2005).

[49] Subroto Mukerjee, Cenke Xu, and J. E. Moore, "Topological Defects and the Superfluid Transition of the $s = 1$ Spinor Condensate in Two Dimensions," Phys. Rev. Lett. **97**, 120406 (2006).

[50] Fei Zhou, "Spin Correlation and Discrete Symmetry in Spinor Bose-Einstein Condensates," Phys. Rev. Lett. **87**, 080401 (2001).

[51] C. Trefzger, C. Menotti, and M. Lewenstein, "Ultracold dipolar gas in an optical lattice: The fate of metastable states," Phys. Rev. A **78**, 043604 (2008).

[52] Jian Zhang and Tin-Lun Ho, "Spontaneous Vortex Lattices in Quasi 2D Dipolar Spinor Condensates," arXiv:0908.1593v1 .

[53] Y. Kawaguchi, H. Saito, K. Kudo, and M. Ueda, "Magnetic Crystallization of a Ferromagnetic Bose-Einstein Condensate," arXiv:0909.0565 .

[54] S. Das Sarma and A. Pinczuk, *Perspectives in Quantum Hall Effects* (John Wiley & Sons, Inc., New York, 1997).

[55] Y.-J. Lin, R. L. Compton, K. Jiménez-García, J. V. Porto, and I. B. Spielman, "Synthetic magnetic fields for ultracold neutral atoms," Nature **462**, 628 (2009).

[56] N. Gemelke, E. Sarajlic, and S. Chu, "Rotating Few-body Atomic Systems in the Fractional Quantum Hall Regime," arXiv:1007.2677v1 .

[57] M. A. Cazalilla, N. Barberán, and N. R. Cooper, "Edge excitations and topological order in a rotating Bose gas," Phys. Rev. B **71**, 121303 (2005).

[58] Jean Dalibard, Fabrice Gerbier, Gediminas Juzeliūnas, and Patrik Öhberg, "*Colloquium* : Artificial gauge potentials for neutral atoms," Rev. Mod. Phys. **83**, 1523–1543 (2011).

[59] N. R. Cooper, "Optical Flux Lattices for Ultracold Atomic Gases," Phys. Rev. Lett. **106**, 175301 (2011).

[60] M. Aidelsburger, M. Atala, S. Nascimbène, S. Trotzky, Y.-A. Chen, and I. Bloch, "Experimental Realization of Strong Effective Magnetic Fields in an Optical Lattice," Phys. Rev. Lett. **107**, 255301 (2011).

[61] R. B. Laughlin, "Anomalous Quantum Hall Effect: An Incompressible Quantum Fluid with Fractionally Charged Excitations," Phys. Rev. Lett. **50**, 1395–1398 (1983).

[62] M. Hafezi, A. S. Sørensen, E. Demler, and M. D. Lukin, "Fractional quantum Hall effect in optical lattices," Phys. Rev. A **76**, 023613 (2007).

[63] L. Hormozi, G. Möller, and S. H. Simon, "Fractional quantum hall effect of lattice bosons near commensurate flux," arXiv:1109.3434v1 .

[64] J. Stenger, S. Inouye, A. P. Chikkatur, D. M. Stamper-Kurn, D. E. Pritchard, and W. Ketterle, "Bragg Spectroscopy of a Bose-Einstein Condensate," Phys. Rev. Lett. **82**, 4569–4573 (1999).

[65] M.-O. Mewes, M. R. Andrews, N. J. van Druten, D. M. Kurn, D. S. Durfee, C. G. Townsend, and W. Ketterle, "Collective Excitations of a Bose-Einstein Condensate in a Magnetic Trap," Phys. Rev. Lett. **77**, 988–991 (1996).

[66] T. Schumm, S. Hofferberth, L. M. Andersson, S. Wildermuth, S. Groth, I. Bar-Joseph, J. Schmiedmayer, and P. Krüger, "Matter-wave interferometry in a double well on an atom chip ," Nature Physics **1**, 57 (2005).

[67] G. Möller and N. R. Cooper, "Composite Fermion Theory for Bosonic Quantum Hall States on Lattices," Phys. Rev. Lett. **103**, 105303 (2009).

[68] N. Read and E. Rezayi, "Beyond paired quantum Hall states: Parafermions and incompressible states in the first excited Landau level," Phys. Rev. B **59**, 8084–8092 (1999).

[69] F. D. M. Haldane, "Fractional Quantization of the Hall Effect: A Hierarchy of Incompressible Quantum Fluid States," Phys. Rev. Lett. **51**, 605–608 (1983).

[70] N. R. Cooper, N. K. Wilkin, and J. M. F. Gunn, "Quantum Phases of Vortices in Rotating Bose-Einstein Condensates," Phys. Rev. Lett. **87**, 120405 (2001).

[71] E. H. Rezayi, N. Read, and N. R. Cooper, "Incompressible Liquid State of Rapidly Rotating Bosons at Filling Factor 3/2," Phys. Rev. Lett. **95**, 160404 (2005).

[72] M. H. Freedman, A. Kitaev, M. J. Larsen, and Z. Wang, "Topological quantum computation," Bull. Amer. Math. Soc. **40**, 31 (2003).

[73] R. N. Palmer and D. Jaksch, "High-Field Fractional Quantum Hall Effect in Optical Lattices," Phys. Rev. Lett. **96**, 180407 (2006).

[74] Evelyn Tang, Jia-Wei Mei, and Xiao-Gang Wen, "High-Temperature Fractional Quantum Hall States," Phys. Rev. Lett. **106**, 236802 (2011).

[75] Titus Neupert, Luiz Santos, Claudio Chamon, and Christopher Mudry, "Fractional Quantum Hall States at Zero Magnetic Field," Phys. Rev. Lett. **106**, 236804 (2011).

[76] Kai Sun, Zhengcheng Gu, Hosho Katsura, and S. Das Sarma, "Nearly Flatbands with Nontrivial Topology," Phys. Rev. Lett. **106**, 236803 (2011).

[77] D. N. Sheng, Z.-C. Gu, K. Sun, and L. Sheng, "Fractional quantum Hall effect in the absence of Landau levels," Nature Communications **2**, 389 (2011).

[78] Yi-Fei Wang, Zheng-Cheng Gu, Chang-De Gong, and D. N. Sheng, "Fractional Quantum Hall Effect of Hard-Core Bosons in Topological Flat Bands," Phys. Rev. Lett. **107**, 146803 (2011).

[79] N. Regnault and B. Andrei Bernevig, "Fractional Chern Insulator," Phys. Rev. X **1**, 021014 (2011).

[80] James S. Douglas and Keith Burnett, "Imaging of quantum Hall states in ultracold atomic gases," Phys. Rev. A **84**, 053608 (2011).

[81] Erhai Zhao, Noah Bray-Ali, Carl J. Williams, I. B. Spielman, and Indubala I. Satija, "Chern numbers hiding in time-of-flight images," Phys. Rev. A **84**, 063629 (2011).

[82] E. Alba, X. Fernandez-Gonzalvo, J. Mur-Petit, J. K. Pachos, and J. J. Garcia-Ripoll, "Seeing Topological Order in Time-of-Flight Measurements," Phys. Rev. Lett. **107**, 235301 (2011).

[83] Christopher N. Varney, Kai Sun, Marcos Rigol, and Victor Galitski, "Topological phase transitions for interacting finite systems," Phys. Rev. B **84**, 241105 (2011).

[84] A. B. Zamolodchikov, "Integrals of motion and the S-matrix of the (scaled) $T = T_c$ Ising model with magnetic field," Int. J. Mod. Phys. A **04**, 4235–4248 (1989).

[85] Giuseppe Mussardo, *Statistical Field Theory: An Introduction to Exactly Solved Models in Statistical Physics* (Oxford University Press, 2009).

[86] S. Lee, R. K. Kaul, and Leon Balents, "Interplay of quantum criticality and geometric frustration in columbite," Nat. Phys. **6**, 702 (2010).

[87] Sam T. Carr and Alexei M. Tsvelik, "Spectrum and Correlation Functions of a Quasi-One-Dimensional Quantum Ising Model," Phys. Rev. Lett. **90**, 177206 (2003).

[88] Barry M. McCoy and Tai Tsun Wu, "Two-dimensional Ising field theory in a magnetic field: Breakup of the cut in the two-point function," Phys. Rev. D **18**, 1259–1267 (1978).

[89] S. B. Rutkevich, "Energy spectrum of bound-spinons in the quantum Ising spin-chain ferromagnet," J. Stat. Phys. **131**, 917–939 (2008).

[90] R. Coldea, D. A. Tennant, E. M. Wheeler, E. Wawrzynska, D. Prabhakaran, M. Telling, K. Habicht, P. Smeibidl, and K. Kiefer, (2010), supporting online material for ref. 1 .

[91] Steven R. White, "Density matrix formulation for quantum renormalization groups," Phys. Rev. Lett. **69**, 2863–2866 (1992).

[92] M. Fannes, B. Nachtergaele, and R. Werner, "Finitely correlated states on quantum spin chains," Commun. Math. Phys. **144**, 443–490 (1992), 10.1007/BF02099178.

[93] D. Gottesman and M. B. Hastings, "Entanlement versus gap for one-dimensional spin systems," New J. Phys. **12**, 025002 (2010).

[94] Thomas Barthel, Ulrich Schollwöck, and Steven R. White, "Spectral functions in one-dimensional quantum systems at finite temperature using the density matrix renormalization group," Phys. Rev. B **79**, 245101 (2009).

[95] Steven R. White and Ian Affleck, "Spectral function for the $S = 1$ Heisenberg antiferromagetic chain," Phys. Rev. B **77**, 134437 (2008).

[96] S. B. Rutkevich, "On the weak confinement of kinks in the one-dimensional quantum ferromagnet $CoNb_2O_6$," J. Stat. Mech. **7**, 07015 (2010).

[97] Bella Lake, Alexei M. Tsvelik, Susanne Notbohm, Alan D. Tennant, Toby G. Perring, Manfred Reehuis, Chinnathambi Sekar, Gernot Krabbes, and Bernd Büchner, "Confinement of fractional quantum number particles in a condensed-matter system," Nat. Phys. **6**, 50–55 (2010).

[98] V. A. Fateev, "The exact relations between the coupling constants and the masses of particles for the integrable perturbed conformal field theories," Phys. Lett. B **324**, 45 (1994).

[99] C. Destri, F. Di Renzo, E. Onofri, P. Rossi, and G. P. Tecchiolli, "Swendsen-Wang Monte Carlo study of the Ising model with external field," Phys. Lett. B **278**, 311 (1991).

[100] G. Delfino and G. Mussardo, "The spin-spin correlation function in the two-dimensional Ising model in a magnetic field at $T = T_c$," Nucl. Phys. B **455**, 724 (1995).

[101] P. Fonseca and A. Zamolodchikov, "Ising Field Theory in a Magnetic Field: Analytic Properties of the Free Energy," J. Stat. Phys. **110**, 527–590 (2003), 10.1023/A:1022147532606.

[102] F. D. M. Haldane, "Continuum dynamics of the 1-D Heisenberg antiferromagnet: Identification with the O(3) nonlinear sigma model," Phys. Lett. **93A**, 464 (1983).

[103] F. D. M. Haldane, "Nonlinear Field Theory of Large-Spin Heisenberg Antiferromagnets: Semiclassically Quantized Solitons of the One-Dimensional Easy-Axis Néel State," Phys. Rev. Lett. **50**, 1153–1156 (1983).

[104] H. J. Schulz, "Phase diagrams and correlation exponents for quantum spin chains of arbitrary spin quantum number," Phys. Rev. B **34**, 6372–6385 (1986).

[105] M Oshikawa, "Hidden $Z_2 * Z_2$ symmetry in quantum spin chains with arbitrary integer spin," J. Phys. Condens. Matter **4**, 7469 (1992).

[106] H. Aschauer and U. Schollwöck, "Absence of string order in the anisotropic $S = 2$ Heisenberg antiferromagnet," Phys. Rev. B **58**, 359–365 (1998).

[107] T. Tonegawa, K. Okamoto, H. Nakano, T. Sakai, K. Nomura, and M. Kaburagi, "Haldane, Large-D, and Intermediate-D States in an $S = 2$ Quantum Spin Chain with On-Site and XXZ Anisotropies," J. Phys. Soc. Jpn. **80**, 043001 (2011).

[108] Y.-C. Tzeng, "Parity quantum numbers in Density Matrix Renormalization Group," arXiv:1204.4933v1 .

[109] A Kitazawa, "Twisted boundary conditions of quantum spin chains near the Gaussian fixed points," J. Phys. A **30**, L285 (1997).

[110] K. Nomura and A. Kitazawa, "$SU(2)/Z_2$ symmetry of the BKT transition and twisted boundary condition," J. Phys. A **31**, 7341 (1998).

[111] Marcel den Nijs and Koos Rommelse, "Preroughening transitions in crystal surfaces and valence-bond phases in quantum spin chains," Phys. Rev. B **40**, 4709–4734 (1989).

[112] U. Schollwöck, O. Golinelli, and Th. Jolicoeur, "$S = 2$ antiferromagnetic quantum spin chain," Phys. Rev. B **54**, 4038 (1996).

[113] Ian Affleck, Tom Kennedy, Elliott H. Lieb, and Hal Tasaki, "Rigorous results on valence-bond ground states in antiferromagnets," Phys. Rev. Lett. **59**, 799–802 (1987).

[114] Frank Pollmann, Erez Berg, Ari M. Turner, and Masaki Oshikawa, "Symmetry protection of topological phases in one-dimensional quantum spin systems," Phys. Rev. B **85**, 075125 (2012).

[115] Bo Wang, Mang Feng, and Ze-Qian Chen, "Berezinskii-kosterlitz-thouless transition uncovered by the fidelity susceptibility in the XXZ model," Phys. Rev. A **81**, 064301 (2010).

[116] S.-J. Gu, "Fidelity approach to quantum phase transitions," Int. J. Mod. Phys. B **24**, 4371 (2010).

[117] P. Calabrese and J. Cardy, "Entanglement entropy and quantum field theory," J. Stat. Mech. **06**, P06002 (2004).

[118] L. Tagliacozzo, Thiago. R. de Oliveira, S. Iblisdir, and J. I. Latorre, "Scaling of entanglement support for matrix product states," Phys. Rev. B **78**, 024410 (2008).

[119] Frank Pollmann, Subroto Mukerjee, Ari A. M. Turner, and Joel E. Moore, "Theory of finite-entanglement scaling at one-dimensional quantum critical points," Phys. Rev. Lett. **102**, 255701 (2009).

[120] Hong-Hao Tu and Román Orús, "Intermediate Haldane phase in spin-2 quantum chains with uniaxial anisotropy," Phys. Rev. B **84**, 140407 (2011).